



저작자표시-비영리-변경금지 2.0 대한민국

이용자는 아래의 조건을 따르는 경우에 한하여 자유롭게

- 이 저작물을 복제, 배포, 전송, 전시, 공연 및 방송할 수 있습니다.

다음과 같은 조건을 따라야 합니다:



저작자표시. 귀하는 원저작자를 표시하여야 합니다.



비영리. 귀하는 이 저작물을 영리 목적으로 이용할 수 없습니다.



변경금지. 귀하는 이 저작물을 개작, 변형 또는 가공할 수 없습니다.

- 귀하는, 이 저작물의 재이용이나 배포의 경우, 이 저작물에 적용된 이용허락조건을 명확하게 나타내어야 합니다.
- 저작권자로부터 별도의 허가를 받으면 이러한 조건들은 적용되지 않습니다.

저작권법에 따른 이용자의 권리는 위의 내용에 의하여 영향을 받지 않습니다.

이것은 [이용허락규약\(Legal Code\)](#)을 이해하기 쉽게 요약한 것입니다.

[Disclaimer](#)

공학박사학위논문

**Fabrication of Polymer Nanostructures by
Conventional/Unconventional Anodization
Techniques and Their Applications in
Liquid Crystal Displays (LCDs)**

전통적인/비전통적인 양극산화법을 통한
고분자 나노 구조 제조 및
액정 디스플레이로의 응용

2013년 2월

서울대학교 대학원
화학생물공학부
이 경 희

Abstract

Fabrication of Polymer Nanostructures by Conventional/Unconventional Anodization Techniques and Their Applications in Liquid Crystal Displays (LCDs)

Kyunghee Lee

School of Chemical and Biological Engineering

The Graduate School

Seoul National University

Anodization techniques based on self-organized behavior have been of great interest, especially for the preparation of large-area, nanometer-sized structures with high aspect ratios, which are difficult to form by a conventional lithographic process based on expensive vacuum equipment. Anodic aluminum oxide (AAO) has a nanoscopically cylindrical pore arrays with a hexagonally ordered arrangement, so AAO has become a popular nanotemplate for the fabrication of various functional nanostructures such as nanorods, nanowires, and nanotubes. As nanofabrication technologies have been developed toward more complex nanostructure with low-dimension, complicated or hierarchical nanostructures become a highly noticeable architecture. In this study, we suggest a simple and novel anodization technique (unconventional anodization) for fabricating

hierarchical nanostructures with various shapes, maintaining advantages of conventional anodization method. Hierarchical polymer nanostructures were replicated from AAO nanotemplate obtained by unconventional anodization, and we analyzed their surface properties. In addition, we tried to apply nanopatterned surface to alignment layer and organic thin film transistors of liquid crystal displays (LCDs).

In Chapter 1, we introduce conventional anodization technique as one of nanotechnologies for the preparation of nanostructures. Additionally, we add their versatile applications in practical fields such as electronics or optoelectronics, magnetic, and biosensors.

In Chapter 2, we suggest unconventional anodization technique, which makes possible to fabricate more complex nanostructures with various shapes. Hierarchical AAO was obtained through the thinning process of oxide layer and the sequential anodization process at lower voltage. According to sequential anodization conditions such as the type of electrolyte and the applied voltage, the hierarchy was varied. Moreover, we fabricated the very tiny hierarchical nanopore arrays with pore diameter less than 100nm via unconventional anodization, which are limited to manufacture by conventional lithography techniques.

In Chapter 3, hierarchical structures consisting of micro- or nano-meter scale structures have been discovered in many plant leaves and insect wings or legs, and exhibited outstanding properties on their surfaces. Thus, we investigate to mimic unique hierarchical structures by unconventional anodization in order to realize their superior properties. Firstly, the artificial lotus-leaf-inspired polymer nanostructures were fabricated by the replication AAO templates that have

hierarchical nanopores via subsequent anodization on concave Al surface with the variation of the applied voltages. Then, we analyzed surface wettability of these hierarchical nanostructures. Secondly, for mimicking gecko's foot surface, asymmetrically bent polymer nanopillars were prepared by metal deposition onto one lateral side of polymer nanopillars after the fabrication of polymer nanopillars replicated from AAO template, because the natural gecko setae show frictional anisotropy. Anisotropic adhesion behavior was observed due to structural peculiarity.

In Chapter 4, we apprehend the structure of liquid crystal displays (TFT-LCDs) in order to apply micro/nanopatterned surfaces to TFT-LCDs. The patterned surface would be suitable as an alignment layer in TFT-LCDs because the orientation of LC molecules on the alignment layer is influenced by surface topography. We study LC alignment method and alignment mechanism. Furthermore, we introduce basic theory of organic thin film transistors to utilize the patterned surface in organic semiconductor layer.

In Chapter 5, we investigate the alignment behavior of LC molecules with the variation of nanostructure size. As alignment layer, one-dimensional polymer nanostructure arrays replicated from AAO template was firstly prepared. When small LC molecules are confined by nanoscopic environment, they would suffer strong packing frustration because of the size similarity between LC molecules and nanoscopic space. We observed the transition of LC alignment from random to vertical orientation with the increase of nanorod diameter and length.

In Chapter 6, we demonstrate the surface chemical compositions and nanoscopic topography effect on LC alignment. Several photocurable polymers with different

surface free energies were used to examine the interaction at the LC/alignment layer interface. Diameter-controlled polymer nanorods were obtained from AAO templates. The alignment transition of LC molecules was only observed in polymer nanorod structure with moderate surface energy according to the increase of nanorod diameter. It can be interpreted that the LC alignment on nanorod arrays is determined by two competition interactions; the LC-LC interaction by spatial confinement and the LC-alignment layer interaction by surface chemical nature.

In Chapter 7, we investigate a simple and novel method to make micropatterned organic semiconductors. The organic semiconductor was crystallized along the patterned surfaces of PDMS pad. Similar to a commercial rubber stamp, the crystalline organic semiconductor layer onto PDMS pad was transferred to the substrate after conformal contact. The molecular ordering and crystalline structures of transferred micropatterns was confirmed by 2D-grazing incidence x-ray diffraction (GIXRD). Electrical properties of the OTFTs with micropatterned semiconductors showed considerably enhanced device performance.

Keywords: Anodic Aluminum Oxide (AAO), nanostructures, hierarchical structures, liquid crystals, alignment layer, organic thin film transistors (OTFTs)

Student Number: 2007-21204

TABLE OF CONTENTS

Abstract	i
List of Figures	ix
List of Tables	xx

PART I Fabrication and Characterization of Nanostructures

Chapter 1. Introduction: Nanostructures

1.1. Fabrication Technique for Nanostructures :Conventional Anodization	2
1.2. Applications of Anodized Aluminum Oxide (AAO).....	11
1.3. References	21

Chapter 2. Fabrication of Nanostructures by Unconventional Anodization

2.1. Introduction: Unconventional Anodization	24
2.2. Experimental Section.....	28

2.3. Results and Discussion.....	30
2.4. Conclusion.....	43
2.5. References	44

Chapter 3. Nature-Inspired Nanostructures and Their Properties

3.1. Introduction: Biomimetics	46
3.2. Mimicking Lotus Leaf Surface.....	50
3.2.1. Experimental Section	50
3.2.2. Results and Discussion	55
3.3. Mimicking Gecko’s Foot Surface.....	67
3.2.1. Experimental Section	67
3.2.2. Results and Discussion	69
3.4. Conclusion.....	83
3.5. References	85

PART II Applications of Patterned Surfaces in Display

Devices

Chapter 4. Introduction: Practical Applications of Patterned Surface

4.1. TFT-LCD Displays	89
4.2. Liquid Crystal Alignment.....	91

4.2.1. Liquid Crystal Alignment Methods.....	91
4.2.2. The Mechanism of Liquid Crystal Alignment...	100
4.3. Organic Thin Film Transistors	103
4.3.1. Organic Thin-Film Transistors (OTFTs)	103
4.3.2. Thin-Film Transistor Architecture	104
4.3.3. Operating Mode.....	106
4.3.4. OTFTs Parameters.....	107
4.4. References	110

Chapter 5. Nanoconfinement Effect on LC alignment

5.1. Introduction	112
5.2. Experimental Section.....	114
5.3. Results and Discussion.....	117
5.3.1. The Effect of Surface Pattern Size on LC Alignment : Microstructure vs. Nanostructure.....	117
5.3.2. The Influence of Nanoconfinement on LC Alignment	120
5.4. Conclusion.....	127
5.5. References	128

Chapter 6. Surface Wettability and Topography Effect on LC Alignment

6.1. Introduction	131
6.2. Experimental Section.....	133
6.3. Results and Discussion.....	137
6.4. Conclusion.....	154
6.5. References	155

Chapter 7. Patterning of Solution-Processed Organic Semiconductors

7.1. Introduction	158
7.1.1. Solution-Processed Organic Semiconductors ...	158
7.1.2. Patterning of Organic Semiconductors.....	161
7.1.3. Motivation.....	166
7.2. Experimental Section.....	168
7.3. Results and Discussion.....	172
7.4. Conclusion.....	191
7.5. References	192

국문초록.....	195
------------------	------------

List of Figures

- Figure 1.1.** Schematic illustration of experimental setup of conventional anodization (a) and the porous oxide formation from aluminum to alumina (b).
- Figure 1.2.** Schematic drawing of the idealized configuration of AAO with top-view (a) and cross-sectional view (b), and structural properties of self-ordered nanoporous AAO (c).
- Figure 1.3.** Anodization instrument for the synthesis of AAO (a) and the experimental process of conventional anodization (b).
- Figure 1.4.** The etched (concave) surface (a) and nanoporous AAO with various diameters obtained in sulfuric acid (b), oxalic acid (c), and phosphoric acid (d).
- Figure 1.5.** Various applications using nanoporous AAO template.
- Figure 1.6.** Schematic route to fabricate ordered Tin oxide nanopore films. AAO template (a); the top view of the ordered tin nanopores array on the top of AAO (b); annealing at different temperature (c); the ordered SnO₂ nanopore-film-based UV photodetector (d).
- Figure 1.7.** Schematic illustration of electrode arrangement for deposition of nanowires (a), the current-time curve for electrodeposition of Ni into porous membrane (b), an array of 60 nm diameter Ni nanowires embedded in porous template (c), and the magnetization hysteresis loops with the magnetic field applied parallel and perpendicular to the film plane (d).

- Figure 1.8.** Schematic procedure of preparation of NiO/Ni nanorod ReRam device (a), current-voltage (I-V) characteristics of the nanorod sample (b), and cycle number of switching voltage dependence (c).
- Figure 1.9.** SEM images of porous TiO₂/Al₂O₃ before/after sol-gel coating (a) and the photocatalytic performance (b).
- Figure 1.10.** AAO membranes with the variation of nanopore diameter along a longitudinal direction and peak wavelength shift of the reflectance as a function of the porosity.
- Figure 1.11.** Schematic of flow-through-type DNA array based on the ordered AAO (a), and fluorescence images after hybridization with complementary pairs of the probe DNA: DNA1-DNA3 (left), DNA2-DNA4 (right).
- Figure 2.1.** SEM images of nanofunnels and inverted nanofunnels (a), and modulated pore structures (b).
- Figure 2.2.** Schematic illustration to synthesize the Y-branched pores (a) and the resulting branched nanowire structures (b).
- Figure 2.3.** Schematic route to fabricate hierarchical structures via unconventional anodization.
- Figure 2.4.** The change of barrier layer thickness with thinning process time.
- Figure 2.5.** SEM images of hierarchical structures fabricated via the unconventional anodization. Scale bars are 500 nm (the first and third rows) and 100 nm (the second row and the inset in the third row).
- Figure 2.6.** SEM images of hierarchical polymer nanostructures replicated from

AAO templates. Scale bars are 100 nm (left) and 500 nm (right).

Figure 2.7. SEM images of hierarchical polymer nanostructures with $D_p < 100$ nm. Scale bars are 100 nm.

Figure 2.8. The change of barrier layer thickness with thinning process time. Scale bars are 100 nm.

Figure 2.9. Schematic showing the fabrication of nanochannel membrane.

Figure 2.10. The change of water contact angle with the increase of dissolving time of barrier layer. Scale bars are 100 nm.

Figure 2.11. Multiscale nanomenbrane obtained by the unconventional anodization.

Figure 3.1. Various examples of biomimetic surface discovered in nature.

Figure 3.2. Schematic illustration of hierarchical polymeric nanostructures using AAO template.

Figure 3.3. The morphology of various water-repellent plants and artificial biomimetic polymer surfaces manufactured in this study: (a) *Colocasia esculenta*, (b) *Lupines polyphyllus*, (c) *Gladiolus watsonioides*, (d) *Hhygoryza aristata*, and (e) *Alchenilla duplophylla*. Scale bars= 20 μm for (a), (c)-(e) and 50 μm for (b) in the first row, and scale bars= 500 nm in the second row.

Figure 3.4. The SEM images of nanoscopic hierarchical structured AAO templates and PFPE rods. The top-view SEM images of etched (concave) Al surface and hierarchical AAO templates with the low magnitude (the first row, scale bars=500 nm) and the high magnitude (the second row, scale bars=100 nm), and the cross-sectional SEM

images of hierarchical nanopores (the third row, scale bars=100 nm). The SEM images of convex PFPE surface and hierarchical nanostructures replicated from AAO templates are also given (The fourth row, scale bars=500 nm). The top row indicates the anodization voltage (40-195V) with the chemically etched Al that is given at the first left column.

Figure 3.5. Water contact angles of flat, convex, and hierarchical PFPE surfaces. The “Etched” surface was obtained from etched Al.

Figure 3.6. Water contact angles of flat, convex, and hierarchical PUA surfaces with SEM images of each nanostructures. Scale bar= 500 nm.

Figure 3.7. Water contact angles of flat, convex, and hierarchical TPT surfaces with SEM images of each nanostructures. Scale bar= 500 nm.

Figure 3.8. Comparison of water contact angles on PFPE, PDMS-coated PUA, and PDMS-coated TPT surfaces.

Figure 3.9. The hierarchical nanopillar surface: (a) schematic route to nanoscopic branches in a nanopore, (b) top and cross-sectional SEM images of hierarchical structures of AAO template (the first and second row, scale bars= 500 nm (left) and 100 nm (right)) and PFPE (the third row, scale bars= 1 μ m (left) and 500 nm (right)), and (c) the water contact angle of hierarchical nanopillar surface.

Figure 3.10. Schematic route to hierarchical polymeric nanostructures obtained from etched Al films or AAO template.

Figure 3.11. Force-distance curve depicting the interaction of the AFM tip with the sample surface.

- Figure 3.12.** Adhesive forces on bulk PS, thin film, and one-dimensional PS nanorod arrays.
- Figure 3.13.** Adhesive properties and SEM images of convex surface replicated from the etched Al surface with wavelength variation.
- Figure 3.14.** Structural complexity effect on adhesive force. Adhesive force on convex and double -embossed structures with 110 nm and 500 nm in wavelength (a), and convex, double-embossed, and triple-embossed nanostructures with 500 nm in wavelength (b). SEM images of each nanostructures are displayed under the graph.
- Figure 3.15.** Adhesive properties and SEM images of branched structures based on one-dimensional nanostructures.
- Figure 3.16.** Schematic illustration of real contact area between the tip with Au-particle and nanostructured surfaces.
- Figure 3.17.** The relation between the adhesive force and the real contact area.
- Figure 3.18.** Schematic illustration of the experimental procedure to fabricate asymmetrically bent Janus nanopillar arrays prepared from reusable AAO templates.
- Figure 3.19.** Asymmetrically bent Janus nanopillars and the shear adhesive properties of bent Janus nanopillars: A schematic illustration of the fabrication of bent Janus nanopillars by Au evaporation (a), SEM image of bent nanopillars prepared by 20 nm thick Au evaporation. Scale bar= 500 nm (b). The shear adhesion force of PUA nanopillar arrays (c).
- Figure 4.1.** Basic structure of TFT-LCD devices.

- Figure 4.2.** Typical orientations of nematic LCs.
- Figure 4.3.** Common LC alignment methods: contact and non-contact method.
- Figure 4.4.** Contact alignment method: mechanical rubbing.
- Figure 4.5.** Non-contact alignment method (1): photoalignment.
- Figure 4.6.** Non-contact alignment method (2): Micrograting.
- Figure 4.7.** Architecture of OTFTs based on bottom-gate structure. Bottom contact (BC) device (a) and top contact (TC) device (b).
- Figure 4.8.** The typical output curves (a) and transfer curves (b) of OTFTs.
- Figure 5.1.** Schematic diagrams of LC Cells with nanostructured PS alignment layer.
- Figure 5.2.** Order parameter of LC alignment with the variation of pattern size.
- Figure 5.3.** SEM (top) and POM (bottom) images of line patterns with the variation of pattern widths ranging from 300 nm to 5.1 μm .
- Figure 5.4.** SEM images of diameter-controlled AAO templates and PS nanorod arrays ranging from 38 nm to 86 nm and POM images of LC cell. SEM images: (a) top view and (b) side view of diameter-controlled AAO templates, (c) top view of PS nanorod arrays. (d) POM images of LC cells. Insets: conoscopic images.
- Figure 5.5.** SEM images of length-controlled AAO templates and PS nanorod arrays ranging from 80 nm to 187 nm and POM images of LC cell. SEM images: (a) side view of length-controlled AAO templates, (b) tilt view and (c) top view of PS nanorod arrays. (d) POM images of LC cells. Insets: conoscopic images.
- Figure 6.1.** Schematic route to the LC cells with the polymer nanorod arrays via

UV-assisted nanomolding with AAO templates.

Figure 6.2. Top and cross-sectional SEM images of the diameter-controlled AAO templates. $D1$: 37 nm, $D2$: 47 nm, $D3$: 60 nm, $D4$: 70nm, and $D5$: 83 nm with the fixed L ($\sim 138 \pm 6$ nm) for all templates. Scale bars are 100 nm.

Figure 6.3. Top view SEM images of the photocurable polymer nanorod arrays replicated from the diameter-controlled AAO templates and the conoscopic images.

Figure 6.4. The surface energy of nanostructured PFPE, PUA, and TPT surfaces with the diameter variations ($D1$ - $D5$).

Figure 6.5. The change of the LC contact angles on flat and $D4$ substrates with the elapsed time (< 13 s);PFPE (a), PUA (b), and TPT (c).

Figure 6.6. XRD analysis of LC cell with polyimide (a), 3M tape (b), PET (c), PFPE (d), PUA (e), and TPT (f).

Figure 6.7. SEM and POM images of PUA, APTES-coated PUA, and PDMS-coated PUA substrates. Scale bars are 100 nm.

Figure 6.8. Schematic illustration of LC alignment on PFPE, PUA, and TPT nanorod arrays on the basis of the degree of confinement.

Figure 7.1. Pentacene (a) and 6, 13-bis (triisopropylsilylethynyl) pentacene (TIPS-PEN) (b).

Figure 7.2. Schematic illustration of experimental procedure for the SAM-induced growth of organic semiconductor crystals (a), and the OM images of patterned arrays of anthracene crystals grown on micropatterned SAMs. Scale bars =300 μ m.

- Figure 7.3.** Schematic of procedures for organic single crystal assembly (a), the OM images showing the evaporation process of the CuPc crystal suspension.
- Figure 7.4.** Schematic illustration of the selective contact evaporating printing process (a), and the OM images of micropatterned of single crystal TIPS-PEN prepared by the selective contact evaporating printing method with various sizes and shapes (b).
- Figure 7.5.** Schematic route to the micropatterned TIPS-PEN semiconductors via direct pattern transfer.
- Figure 7.6.** The optical images of surface morphologies of TIPS-PEN films obtained by various deposition methods. Each films are prepared by spin coating with 2 wt% TIPS-PEN solution (a), drop casting with 1 wt% TIPS-PEN solution on SiO₂ surface (b) and on chemically patterned SiO₂ surface (c), and direct pattern transfer process with 1 wt% TIPS-PEN solution (d). Scale bars are 100 μm.
- Figure 7.7.** 2D GIXRD patterns for TIPS-PEN films obtained by conventional deposition techniques. The films prepared by spin coating with 2 wt% TIPS-PEN in toluene (a) and chlorobenzene (b), and drop casting with 1 wt% TIPS-PEN in toluene (c) and chlorobenzene (d).
- Figure 7.8.** The optical images of the transferred TIPS-PEN films by the direct pattern transfer process with PDMS pad without glass substrate (a) and the PDMS pad attached to a glass substrate (b).
- Figure 7.9.** The degree of TIPS-PEN crystallization with the elapsed time upon solvent evaporation in rectangular patterns (~length x width

dimensions of $20 \times 70 \mu\text{m}^2$) (a) and in line patterns ($20 \mu\text{m}$) (b). The nucleation and growth of organic crystalline materials prefers to occur at the edge region of patterns. Below the effective evaporation time, the TIPS-PEN crystals are mostly discovered at the pattern edge. Then, the crystal growth is dominant from the edge to center direction until the films are homogeneous. After the effective evaporation time, the nucleation and growth at the edge region are governed again, so the color of TIPS-PEN films changes to purple, and it means that the films become thicker.

Figure 7.10. The optical microscopy images of the transferred TIPS-PEN patterns. When the TIPS-PEN/PDMS stamp was in conformal contact with the SiO_2 surface, the transferred TIPS-PEN micropattern was discontinuous (a). After spin coating of pure solvent (for the SiO_2 surface) (b) or PMMA solution (for the Si surface) (c), the micropatterned TIPS-PEN film became uniform and continuous. As the TIPS-PEN film was transferred on the PMMA surface after the removal of residual solvent, the line patterns were irregular and non-uniform (d).

Figure 7.11. AFM images (a) and OM images (b~j) of the transferred TIPS-PEN micropatterns with various sizes and shapes on the dielectric surfaces. The sizes of line pattern are 10 (b), 20 (c), 25 (d), 30 (e), 35 (f), and $40 \mu\text{m}$ (g). The rectangular patterns are transferred on Si/PMMA (h), Si/ SiO_2 (i), and ITO glass/PMMA (j) surfaces.

Figure 7.12. X-ray diffraction patterns ($\theta/2\theta$ mode) for the TIPS-PEN crystals on

the TIPS-PEN/PDMS stamp and transferred surfaces. The peaks around 5° could be attributed to the combination results of a (001) reflection peak ($\sim 5.3^\circ$) for the TIPS-PEN crystal structure and instrumental noise peaks.

Figure 7.13. 2D GIXRD patterns of the transferred TIPS-PEN micropatterns on SiO_2 (b) and PMMA (c) dielectric layer. A schematic diagram of the experimental set-up for the GIXRD measurements is shown in (a).

Figure 7.14. The output curve (top) and transfer curve (bottom) of the OTFTs with patterned TIPS-PEN semiconductors on SiO_2 surfaces ((a), (c)) and PMMA surfaces ((b), (d)), respectively. The inset of (c) shows the bottom gate and top contact OTFTs with ~ 25 lines of TIPS-PEN channels bridged between Au source and drain.

Figure 7.15. Three-dimensional and line-scan AFM images and of the transferred TIPS-PEN morphology on Si/ SiO_2 (a) and Si/PMMA surfaces (the center region: (b)/ the edge region: (c)). The yellow-dot arrow indicates the direction of the line-scan and the white arrow in (c) points the patterned PMMA surface during stamping process.

Figure 7.16. Output curve and transfer curve of the OTFTs with TIPS-PEN semiconductors prepared by different bottom electrode/ dielectric layer/soaking solution. Si wafer/ SiO_2 (after spin coating of toluene)/ 1 wt% TIPS-PEN in chlorobenzene (a), ITO glass/PMMA/1 wt% TIPS-PEN in chlorobenzene (b), and Si wafer/ SiO_2 (after spin coating of toluene)/ 1 wt% TIPS-PEN in toluene (c). The bottom

gate, top contact OTFTs shows in the inset of transfer curve in (c).

List of Tables

Table 6.1. Surface free energy of photocurable polymer. The dispersive, polar, and total surface free energy was calculated followed by Owens-Wendt model.

Table 7.1. The electrical properties of the OTFTs. For SiO₂ dielectric layer, the solvent in the bracket indicates the residual solvent on the surface after spin coating.

Chapter 1.

Introduction: Nanostructures

1.1. Fabrication Techniques for Nanostructure: Conventional Anodization

There has been of great interest in the fabrication of nanoscopically fine structures because of their potential applications in electronics, optoelectronics and micromechanical devices. One approach to produce nanometer-scale structures has been to use a naturally assembled structure as a master mold [1]. Especially, nanoscopic porous oxide growth on aluminum (Al) plate under anodic bias in various electrolytes has been investigated for more than 40 years (Figure 1.1 (a)). Anodic aluminum oxide (AAO) has a hexagonally packed columnar structure with uniformly sized holes ranging from 4 to 200 nm in diameter. This method originated from the discovery of self-ordered alumina films by Masuda and Fukuda in 1995 [2]. This approach is also very promising, especially for the preparation of large-area, nanometer-sized structures with high aspect ratios, which are difficult to form by a conventional lithographic process. In recent years, nanoporous AAO with a highly ordered arrangement has become a popular template for the fabrication of various functional nanostructures.

Since Masuda and Fukuda's discovery of self-ordered nanoporous alumina films by a conventional anodization process, AAO films have become one of the most common nanotemplates for the fabrication of one-dimensional nanostructures such as nanorods, nanowires, nanotubes, and nanocornes [3-7]. The typical method for fabricating the AAO film is the two-step anodization of high purity Al plates at constant voltage in electrolyte, and the interpore (pore-pore) distance is dependent on the applied voltage and the type of electrolyte: 66 nm (0.3M H₂SO₄, 25V), 100

nm (0.3M $\text{H}_2\text{C}_2\text{O}_4$, 40V), and 500 nm (0.1M H_3PO_4). Here, the first anodization time mostly affects the structural arrangement of pores, and the second anodization time is only determined the pore length [8]. When aluminum is oxidized to aluminum oxide (alumina) in electrolyte solution at a given voltage, the volume expands by approximately a factor of 2 because the atomic density of aluminum in alumina is a factor 2 lower than that in metallic aluminum [9]. The oxidation occurs at the metal (Al)/oxide (Al_2O_3) interface, leading to compressive stresses in the film [9]. However, since the volume change by expansion can only take place in the vertical direction, the morphology of AAO consists of cylindrical nanopores oriented perpendicular to the metal/oxide interface, where each pore at the bottom is closed by a thin barrier (oxide) layer with hemispherical geometry [9]. As shown in Figure 1.1 (b), pores grow perpendicular to the surface with equilibrium of oxide dissolution at the oxide/electrolyte interface and oxide growth at the metal/oxide interface [9, 10]. While the oxide growth takes place due to the migration of oxygen containing ions (O^{2-} , OH^-) from the electrolyte through the oxide layer at the bottom of nanopore, Al^{3+} ions which drift through the oxide layer are ejected into the solution at the oxide/electrolyte interface [10].

Self-organization of a nanopore arrays with top-view and cross-sectional view are described in Figure 1.2 (a) and (b), respectively. The interpore (pore-pore) distance is determined by the applied voltage used for anodization, so it has a good linear relationship with the applied voltage, where the proportionality constant of the interpore distance per applied voltage is approximately 2.5 nm/V [11]. The structural properties of nanoporous AAO fabricated in a given electrolyte are summarized in Figure 1.2 (c). In addition, the porosity (P) of AAO can be calculated by:

$$P = \frac{2\pi}{\sqrt{3}} \left(\frac{r}{D_{\text{int}}} \right)$$

where r is the pore radius, and D_{int} is the interpore distance [12]. The porosity of AAO films increases as the anodizing potential increases. It can be explained by the high current density and strong chemical dissolution enhanced by the electric field [13]. In particular, it was reported that the porosity of the ordered AAO films at high fields is 10-13.5 % [13]. Nielsch et al. have suggested a 10% porosity theory, which was a requisite condition for the arrangement of nanopores based on the volume expansion from alumina to porous alumina [12].

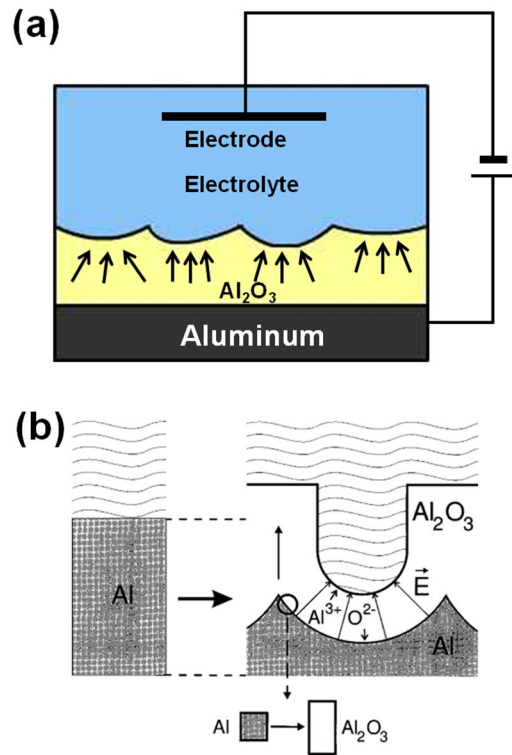
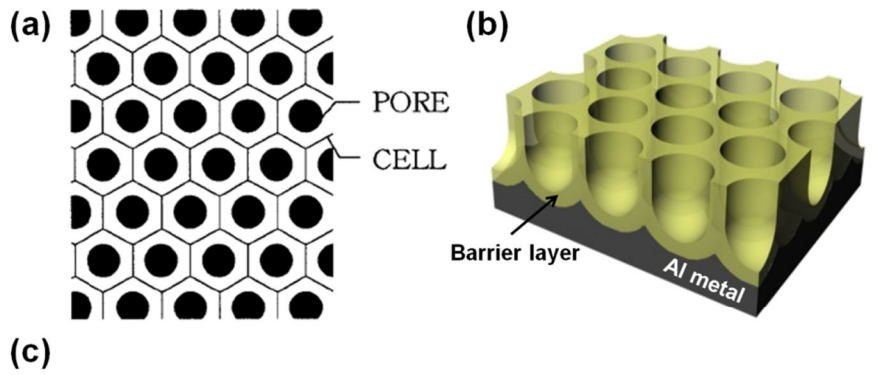


Figure 1.1. Schematic illustration of experimental setup of conventional anodization (a) and the porous oxide formation from aluminum to alumina [10] (b).



(c)

electrolyte	interpore distance D_{int}	inner wall thickness D_{inner}	pore diameter $D_p (= 2r)$
H ₂ SO ₄ 25 V, 0.3 M	66.3 nm	7.2 nm	24 nm
(COOH) ₂ 40 V, 0.3 M	105 nm	9.1 nm	31 nm
H ₃ PO ₄ 195 V, 0.1 M	501 nm	54 nm	158.4 nm

Figure 1.2. Schematic drawing of the idealized configuration of AAO with top-view [11] (a) and cross-sectional view (b), and structural properties of self-ordered nanoporous AAO [12] (c).

Based on previously reported researches, we designed anodization reactor for the synthesis of nanoporous alumina from aluminum plate, as shown in Figure 1.3 (a). The change of AAO morphology analyzed by scanning electron microscopy (SEM) is shown the left part of Figure 1.3 (b). The morphology of AAO is quite disordered after the first anodization. To clarify the cell configuration, alumina was dissolved in the mixture of chromic acid and phosphoric acid solution, and then the second anodization is performed at the same anodization condition as the first anodization. Here, we used three types of electrolyte with different anodization conditions: 0.3M sulfuric acid at 25V, 0.3M oxalic acid at 40V, and 0.1M phosphoric acid at 195V. The etched surface in Figure 1.4 (a) represents that the interpore distances (D_{int}) obtained from sulfuric acid, oxalic acid, and phosphoric acid are approximately 70 nm, 110 nm, and 500 nm, respectively. The diameter of nanopore is controlled in 0.1M phosphoric acid at 30 °C with the range of 15-45 nm (sulfuric acid), 25-80 nm (oxalic acid), and 150-400 nm (phosphoric acid) (Figure 1.4 (b), (c), and (d), respectively).

Outside the self-ordering regimes, the degree of structural ordering decreases dramatically during anodization process. At high voltages or high temperature, oxide dissolution rate at the bottom of nanopore may increase because the enhanced electric field and current density shows large fluctuation, so the local film is thickened [8]. It is called 'breakdown' or 'burning' of the oxide film caused by catastrophic flow of electric current [14]. As a result, the stresses and rates of heat dissipation become irregular at the bottom of nanopore due to the increase of local temperature [8]. Also, the pore arrangement might be disordered because the extent of volume expansion of alumina during anodization was larger [8]. On the other hand, under a low voltage or low temperature, though anodization is very stable,

the pore arrangement becomes very disordered because the expansion of volume during oxide formation at the Al/Al₂O₃ interface is smaller [9]. However, regular pore array can be obtained after sufficient anodization time [8]. Therefore, it indicates that the ordered nanopore arrays can be synthesized only in a stable voltage and current.

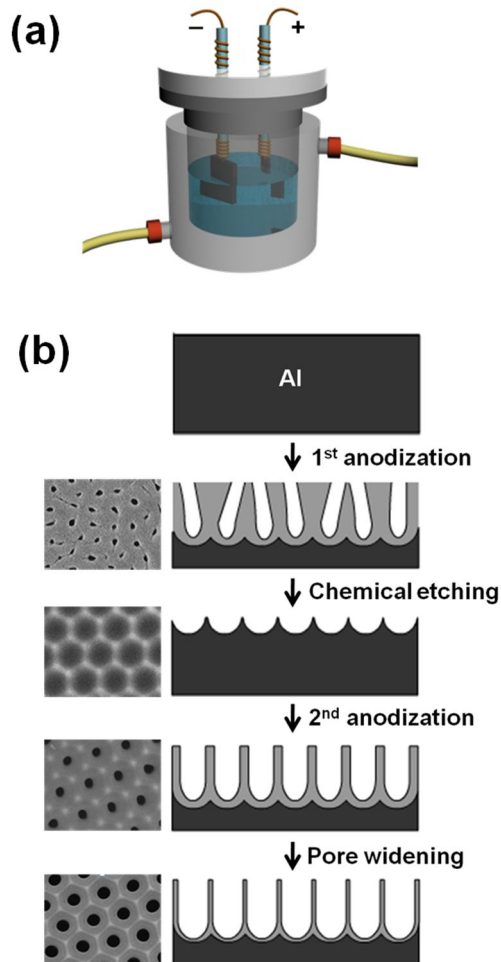


Figure 1.3. Anodization instrument for the synthesis of AAO (a) and the experimental process of conventional anodization (b).

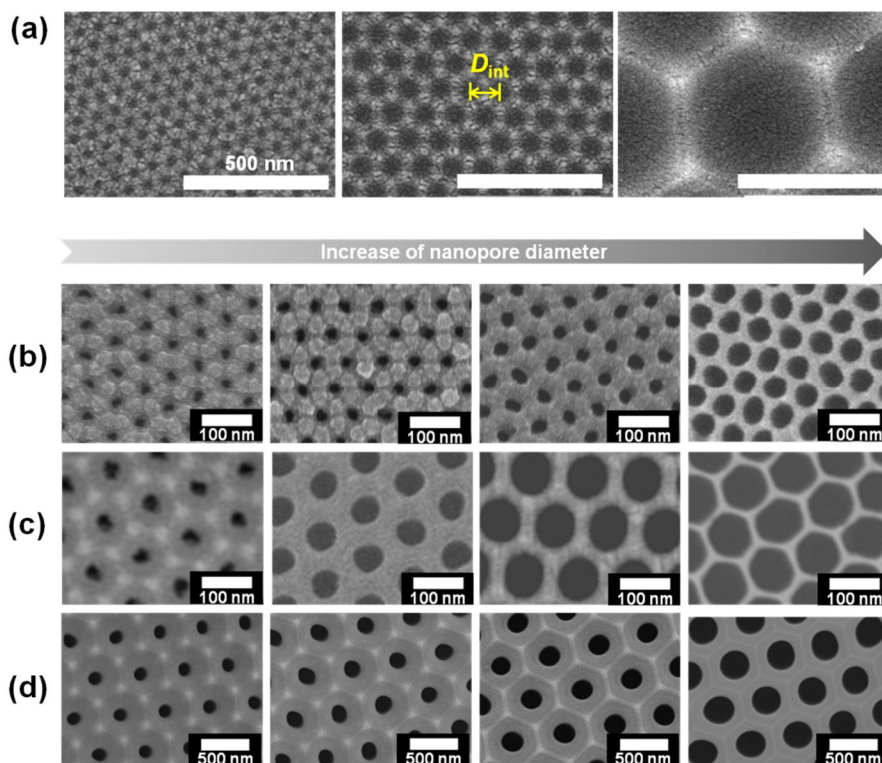


Figure 1.4. The etched (concave) surface (a) and nanoporous AAO with various diameters obtained in sulfuric acid (b), oxalic acid (c), and phosphoric acid (d).

1.2. Applications of Anodized Aluminum Oxide (AAO)

On the basis of recent research progress in developing long-range ordered porous structures, the AAO has been considerably attracted in both scientific and commercial fields as an essential part of nanotechnology (Figure 1.5). This has been employed by their versatile applications in fields of electronics or optoelectronics [15, 16], magnetic [17], energy storage [18, 19], photocatalysis [20], photonics [21], and biosensors [22]. Each example is introduced below.

Electronics and Optoelectronics [15]:

The ordered Tin oxide nanopore films (thickness~150 nm) based on the porous anodic aluminum oxide templates have been successfully fabricated by direct current magnetron sputtering and oxidizing annealing. The schematic illustration in Figure 1.6 exhibits the experimental procedure of Tin oxide nanopores. This ordered nanopore films show a shorter recovery time due to the high specific surface area, compared to thin films for ultraviolet (UV) detection. In particular, the ordered SnO_x nanopore films with lower x possess more excellent sensitivity to detect weak UV light, which was explained by the higher concentration of the oxygen vacancies in this SnO_x films. This work presents a new approach to fabricate the UV light detector based on Tin oxide films.

Magnetics [17]:

Arrays of ferromagnetic nickel and cobalt nanowires have been fabricated by electrochemical deposition of the metals into templates with nanometer-sized pores,

as shown in Figure 1.7. These systems display distinctive characteristics because of their one-dimensional microstructure. The preferred magnetization direction is perpendicular to the film plane (Figure 1.7 (d)). The “easy axis” is for the field applied perpendicular to the film, hence parallel to the nanowires. Ferromagnetic nanowires show considerably enhanced magnetic coercivity because of their single-domain nature.

Memory [19]:

Ni nanorod arrays were formed in the AAO template by pulsed electroplating technique (Figure 1.8 (a)). Figure 1.8 (b) shows that the sample clearly exhibits switching phenomena and I-V hysteresis loops with large “window” in the set and reset processes. In addition, the sample using NiO/Ni nanorod shows one hundred stable switching behaviors, whereas the Ni film sample broke after twenty-two times cycles (Figure 1.8 (c)).

Photocatalysis [20]:

The porous alumina films are employed as the template on which porous TiO₂ nanostructures are synthesized through sol-gel process (Figure 1.9 (a)). The porous TiO₂/Al₂O₃ composite nanostructures exhibited enhanced photocatalytic activities (Figure 1.9 (b)). The enhanced photocatalysis of the composite nanostructures can be mainly ascribed to their hollow nanostructures with large surface areas and appropriate transparency of the porous composite layers.

Photonics [21]:

The AAO membrane with its pore size gradually changing along a longitudinal

direction on the surface was fabricated (Figure 1.10). After Pt coating, the wavelength of peak reflectance gradually changes from red to green as the pore size increases. It can be used in photonic application. Moreover, this strong dependence of an effective refractive index on porosity is a possible candidate for anti-reflection coating.

Biosensors [22]:

A flow-through-type DNA array was fabricated by attaching a single-stranded probe DNA to the sidewall of nanopore in AAO films whose surface was coated with a platinum layer, as shown in Figure 1.11 (a). When probe DNAs were directly affixed to the sidewall of nanopores, the ordered fluorescence spots were observed after hybridization with complementary pair of the probe DNA (Figure 1.11 (b)).

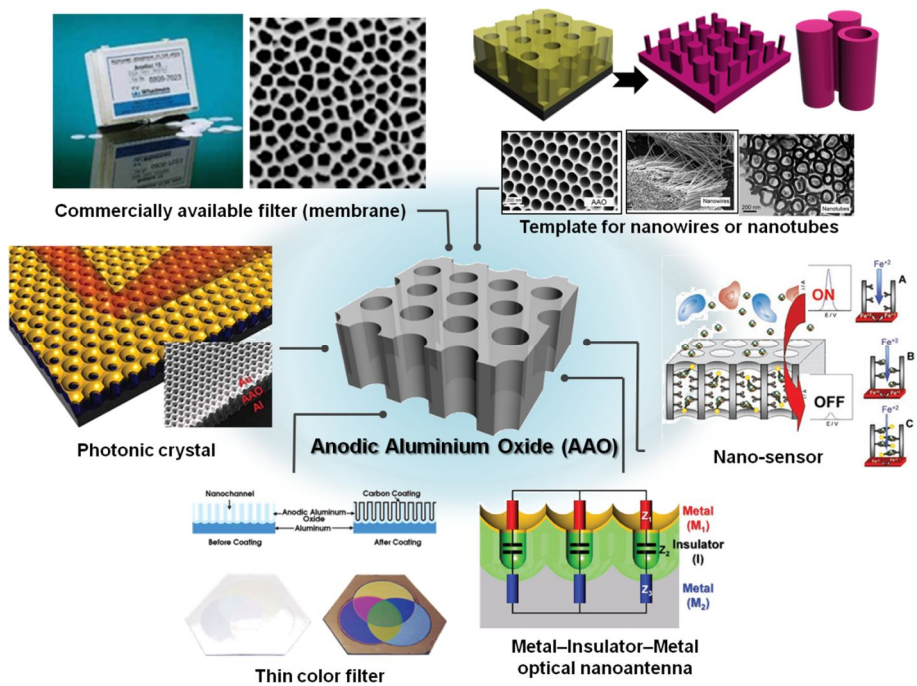


Figure 1.5. Various applications using nanoporous AAO template.

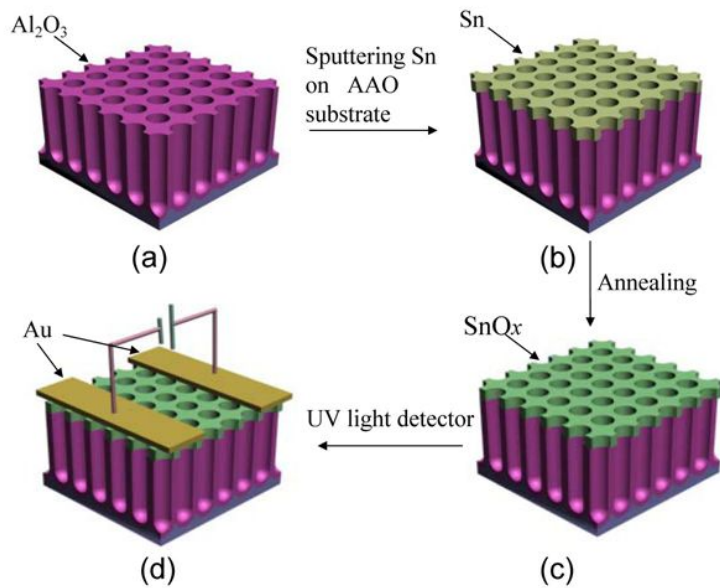


Figure 1.6. Schematic route to fabricate ordered Tin oxide nanopore films. AAO template (a); the top view of the ordered tin nanopores array on the top of AAO (b); annealing at different temperature (c); the ordered SnO_x nanopore-film-based UV photodetector (d) [15].

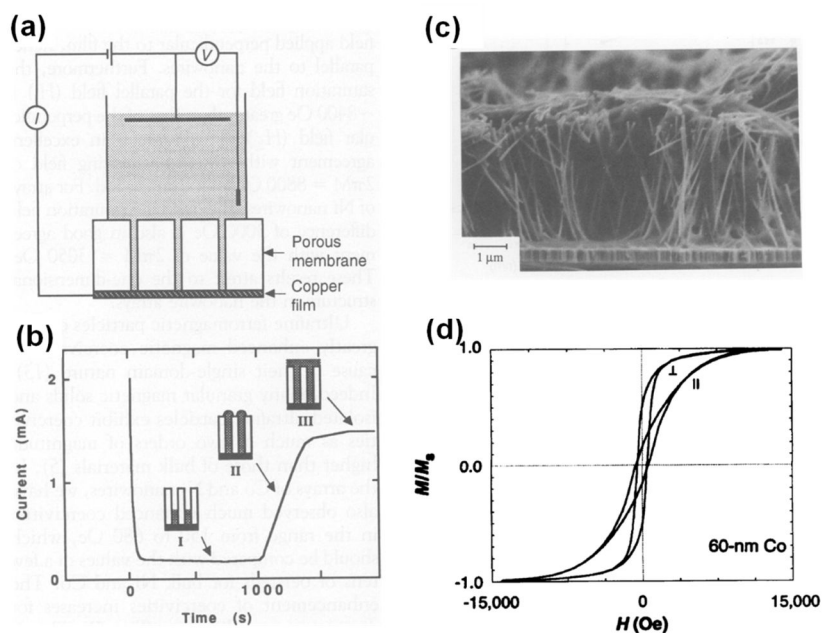


Figure 1.7. Schematic illustration of electrode arrangement for deposition of nanowires (a), the current-time curve for electrodeposition of Ni into porous membrane (b), an array of 60 nm diameter Ni nanowires embedded in porous template (c), and the magnetization hysteresis loops with the magnetic field applied parallel and perpendicular to the film plane (d) [17].

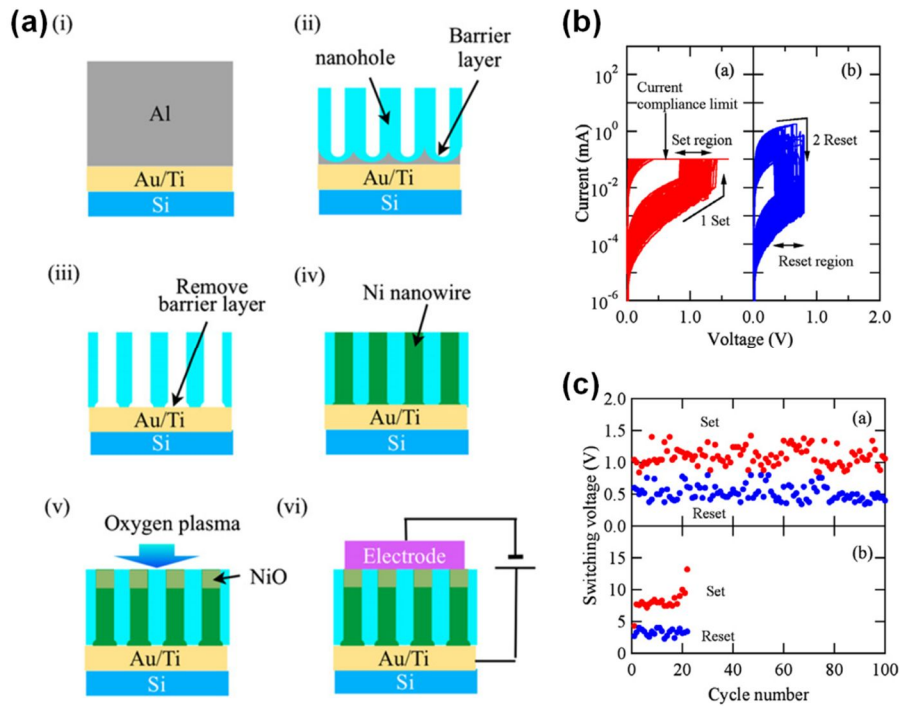


Figure 1.8. Schematic procedure of preparation of NiO/Ni nanorod ReRam device (a), current-voltage (I-V) characteristics of the nanorod sample (b), and cycle number of switching voltage dependence (c) [19].

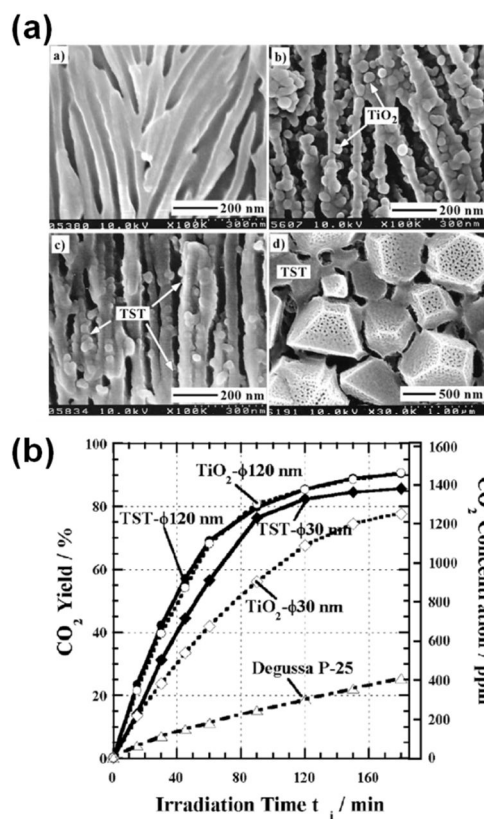


Figure 1.9. SEM images of porous TiO₂/Al₂O₃ before/after sol-gel coating (a) and the photocatalytic performance (b) [20].

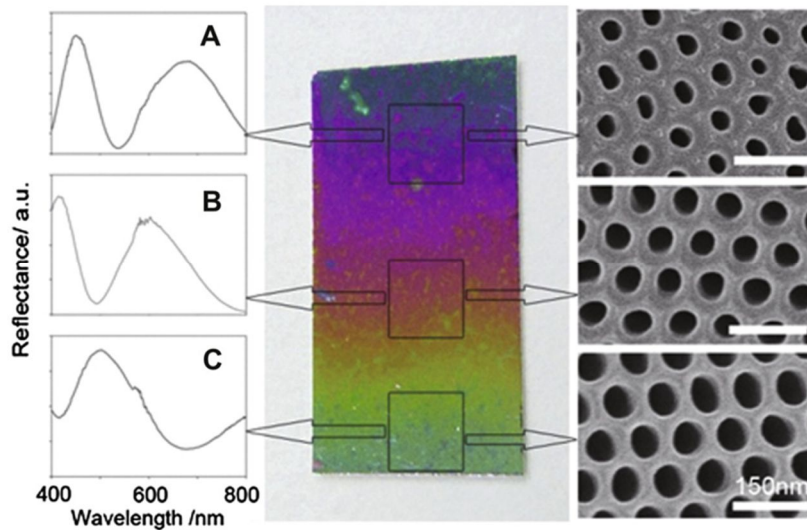


Figure 1.10. AAO membranes with the variation of nanopore diameter along a longitudinal direction and peak wavelength shift of the reflectance as a function of the porosity [21].

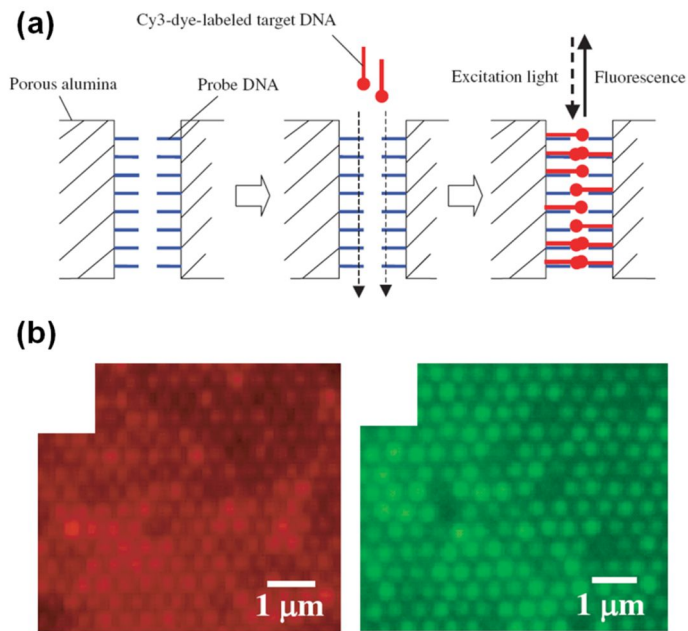


Figure 1.11. Schematic of flow-through-type DNA array based on the ordered AAO (a), and fluorescence images after hybridization with complementary pairs of the probe DNA: DNA1-DNA3 (left), DNA2-DNA4 (right) [22].

1.3. References

- [1] G. E. Thompson, R. C. Furneaux, G. C. Wood, J. A. Richardson, J. S. Goode, *Nature* **1978**, 272, 433.
- [2] H. Masuda, K. Fukuda, *Science* **1995**, 268, 1466.
- [3] S. J. Hurst, E. K. Payne, L. D. Qin, C. A. Mirkin, *Angew. Chem. Int. Ed.* **2006**, 45, 2672.
- [4] N. L. Kovtyukhova, T. E. Mallouk, *Adv. Mater.* **2005**, 17, 187.
- [5] S. B. Lee, D. T. Mitchell, L. Trofin, T. K. Nevanen, H. Soderlund, C. R. Martin, *Science* **2002**, 296, 2198.
- [6] W. Lee, R. Scholz, K. Niesch, U. Gosele, *Angew. Chem. Int. Ed.* **2005**, 44, 6050.
- [7] Z. B. Pi, T. Tian, X. K. Tian, C. Yang, S. X. Zhang, J. H. Zheng, *J. Nanosci. Nanotech.* **2007**, 7, 673.
- [8] S. K. Hwang, S. H. Jeong, H. Y. Hwang, O. J. Lee, K. H. Lee, *Korean J. Chem. Engin.* **2002**, 19, 467.
- [9] A. P. Li, F. Muller, A. Birner, K. Nielsch, U. Gosele, *J. Appl. Phys.* **1998**, 84, 6023.
- [10] O. Jessensky, F. Muller, U. Gosele, *Appl. Phys. Lett.* **1998**, 72, 1173.
- [11] H. Masuda, K. Yada, A. Osaka, *Jpn. J. Appl. Phys. Part 2-Letters* **1998**, 37, L1340.
- [12] K. Nielsch, J. Choi, K. Schwirn, R. B. Wehrspohn, U. Gosele, *Nano Lett.* **2002**, 2, 677.
- [13] S. Z. Chu, K. Wada, S. Inoue, M. Isogai, A. Yasumori, *Adv. Mater.* **2005**, 17, 2115.

- [14] W. Lee, K. Nielsch, U. Gosele, *Nanotechnology* **2007**, *18*, 475713.
- [15] C. L. Li, M. J. Zheng, X. H. Wang, L. J. Yao, L. Ma, W. Z. Shen, *Nano. Res. Lett.* **2011**, *6*, 1.
- [16] R. J. Tonucci, B. L. Justus, A. J. Campillo, C. E. Ford, *Science* **1992**, *258*, 783.
- [17] T. M. Whitney, J. S. Jiang, P. C. Searson, C. L. Chien, *Science* **1993**, *261*, 1316.
- [18] G. L. Che, B. B. Lakshmi, E. R. Fisher, C. R. Martin, *Nature* **1998**, *393*, 346.
- [19] S. Otsuka, S. Furuya, R. Takeda, T. Shimizu, S. Shingubara, T. Watanabe, Y. Takano, K. Takase, *Microelectron. Engin.* **2012**, *98*, 367.
- [20] S. Z. Chu, S. Inoue, K. Wada, D. Li, H. Haneda, *J. Mater. Chem.* **2003**, *13*, 866.
- [21] Y. Zhang, S. J. Son, H. Ju, *Current Appl. Phys.* **2012**, *12*, 1561.
- [22] F. Matsumoto, K. Nishio, H. Masuda, *Adv. Mater.* **2004**, *16*, 2105.

Chapter 2.
Fabrication of Nanostructures
by Unconventional Anodization

2.1. Introduction: Unconventional Anodization

Anodization processes have intensively been attracted in diverse fields of electronics, photonics, architecture, sensors, and transport in the last decade. Even though a typical two-step anodization process has a lot of advantages, explained in previous chapter, it can provide only well-ordered cylindrical nanopore arrays. However, as nanofabrication technologies have been developed toward more complex nanostructure with low-dimension, three-dimensional (3D) nanostructures become a highly noticeable architecture [1-6]. Various techniques based on conventional lithography have been investigated for manufacturing 3D nanostructures, but they are inherently expensive, time-consuming, and complex [7, 8]. Recently, self-assembly techniques have received wide attention in the sub-micrometer scale due to their simple and lower-cost process. There have been a few reports where 3D nanostructures have been created by anodization process. For example, Krishnan and Thompson have reported that the fabrication of 3D nanostructures, such as nanofunnels and inverted nanofunnel, by controlling the pore spacing and diameter (Figure 2.1 (a)) [2]. Lee et al. have investigated the modulated pore structures by oscillatory kinetic behavior during hard anodization of aluminum, as shown in Figure 2.1 (b) [3-5]. The fabrication of AAO template with Y-branched pores has been suggested by Meng and coworkers (Figure 2.2) [6]. The generation of Y-branched nanopores can be obtained by sequential reduction of anodizing voltages. In this method, the rate of voltage reduction is quite critical because if the voltage is reduced suddenly, the nanopores can be divided abruptly [6]. Thus, we suggest a simple and novel anodization technique for fabricating 3D

(or hierarchical) nanostructures with various shapes through unconventional anodization. For conventional anodization, only cylindrical nanopores are produced by the first and second anodization in same anodization conditions such as the type of electrolyte and applied voltage. Anodization conditions, however, can be changed in each anodization step to obtain various hierarchical nanostructures, so we named it “unconventional anodization”.

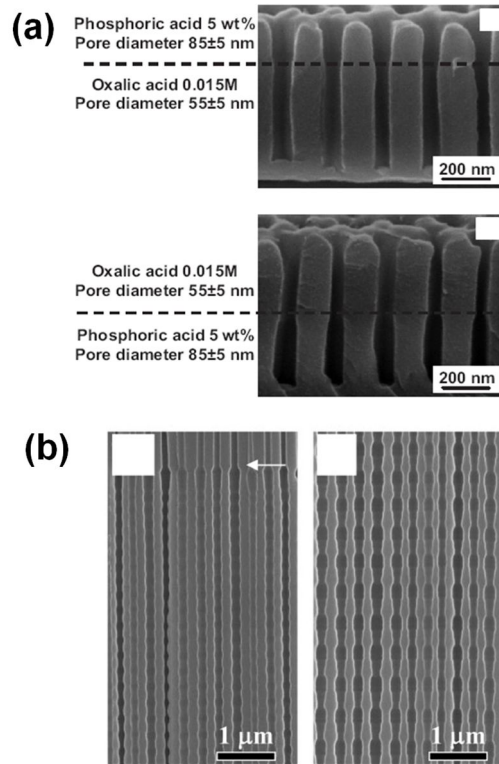


Figure 2.1. SEM images of nanofunnels and inverted nanofunnels [2] (a), and modulated pore structures [4] (b).

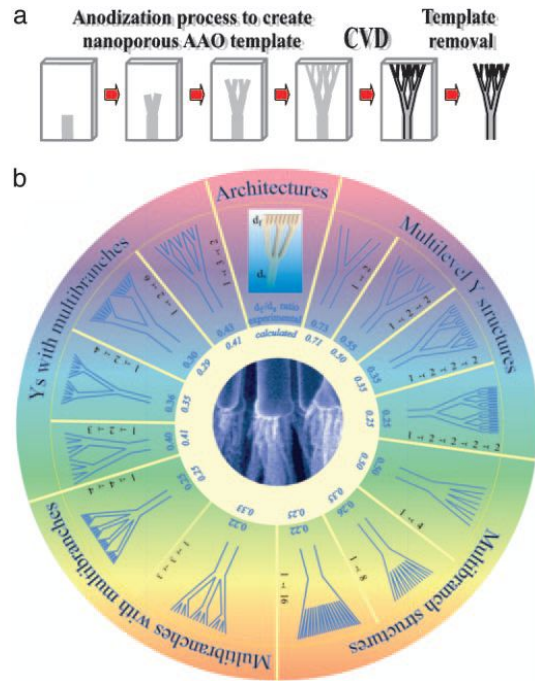


Figure 2.2. Schematic illustration to synthesize the Y-branched pores (a) and the resulting branched nanowire structures (b) [6].

2.2. Experimental section

The schematic route for unconventional anodization is depicted in Figure 2.3. Experimental details are as follows.

Fabrication of hierarchical AAO template:

Cylindrical nanopores were fabricated by conventional two-step anodization, as previously expressed in chapter 1. In order to obtain nanobranches in a cylindrical nanopore, the thickness of barrier layer got thinner by etching the nanopores in a 0.1M phosphoric acid solution at 30°C for 4hr after the second anodization (thinning process). Then, the third anodization was carried out at different voltage (40-140V) as the second anodization. The pore size was controlled by widening time. The hierarchical structures (< 100 nm) via multi-step anodization could be fabricated in a 0.3M oxalic acid solution. The thinning process was performed for 50 min in 0.1 M phosphoric acid at 30°C. Further anodization was carried out at 20V and 40V.

Cap opening of AAO template:

The barrier layer with hemispherical structure at the bottom part of nanopore was dissolved by floating the back side of AAO membrane on 0.1 M phosphoric acid at 60 °C.

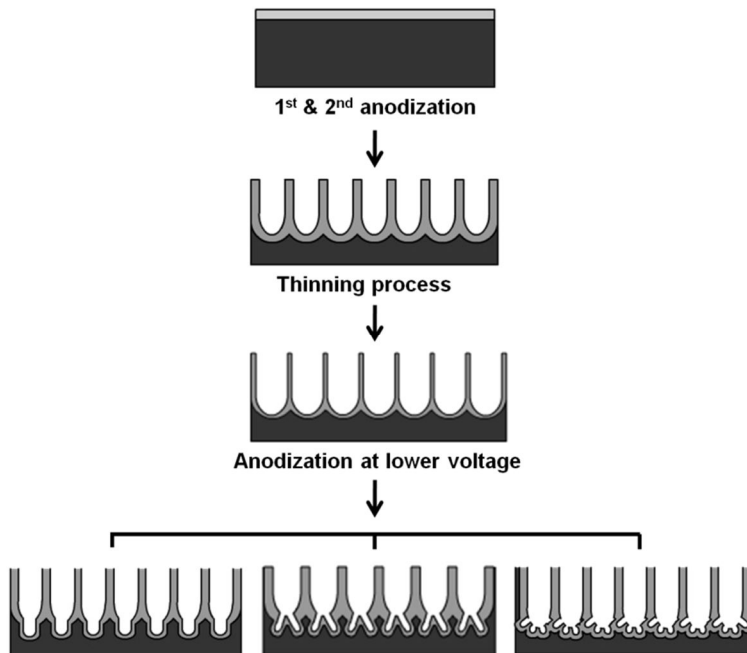


Figure 2.3. Schematic route to fabricate hierarchical structures via unconventional anodization.

2.3. Results and Discussion

The unconventional anodization consists of the thinning process of barrier layer and the anodization process at lower voltage. The anodization voltage ($V_{\text{appl.}}$) affects the thickness of barrier layer along with the interpore distance [9-11]. When the electric field is applied to the aluminum plate, the ion migration occurs through the barrier (oxide) layer. In order to form porous oxide film, the Al^{3+} is reacted with water at the oxide/electrolyte interface and the $\text{O}^{2-}/\text{OH}^-$ from the electrolyte is simultaneously reacted with aluminum at the metal/oxide interface. It means that the barrier layer with the appropriate thickness is required to exchange ions at electrolyte/oxide interface and metal/oxide interface because the reactions take place through the barrier layer. If thicker barrier layer forms under higher electric field, it cannot subsequently grow more under lower electric field due to thick barrier layer. Thus, to perform further anodization at lower voltage than the previous one, thinning the barrier layer is required. The relation between the thickness of barrier layer (t_{wall}) and applied voltage ($V_{\text{appl.}}$) was given by

$$t_{\text{wall}} = 1.2 \text{ nm/V} \times V_{\text{appl.}} (\text{V}) \text{ [12].}$$

Thinning process of barrier layer was carried out in a 0.1M phosphoric acid solution at 30°C, the barrier walls of nanopores got thinner from 176 nm to 36 nm according to thinning process time (Figure 2.4). For example, as the wall thickness of stem nanopores was approximately 67 nm, which could be obtained by thinning process for 4hr, the minimum value as an applicable voltage would be ~60V in our study. We performed multi-step anodization at various lower voltages ranging from 65V to 140V. Figure 2.5 shows the SEM image of AAO obtained by

unconventional anodization. The first and second row presents the top-view SEM image of hierarchical nanopores in a low magnitude and a high magnitude, respectively, and the third row shows the cross-sectional SEM images of hierarchical nanopores. Cylindrical nanopores were fabricated via conventional anodization process in a 0.1M phosphoric acid solution at 195V. However, hierarchical nanopores consisting of larger nanopores and smaller nanobranches were firstly manufactured in a 0.1M phosphoric acid solution at 195V for larger nanopores and then subsequently anodized in 0.1M phosphoric acid or 0.3M oxalic acid solution at different voltages ranging from 65V to 140V for the formation of smaller nanobranches. After the formation of nanobranches, hierarchical nanopores were widened in a 0.1M phosphoric acid solution for 10-30 min. At 40V, no oxide formation takes place at the oxide/electrolyte interface during porous oxide growth because the exchange of ions could not occur through the barrier layer due to thick thickness of the barrier layer. One-branched AAO template was obtained in a 0.1M phosphoric acid solution at 110V and 140V, and multi-branched AAO template was fabricated in a 0.3M oxalic acid solution at 65V and 80V. The SEM images of polymer replica (right) replicated AAO template (left) showed that the cylindrical and hierarchical nanopores were successfully fabricated, as shown in Figure 2.6.

The very tiny hierarchical structures (< 100 nm) via multi-step anodization could be fabricated in a 0.3M oxalic acid solution with the control of the thickness of barrier layer thickness and the applied voltage from 20V to 40V (Figure 2.7). The thickness of barrier layer was ~ 17 nm, which could be acquired by thinning process for 50 min, it was possible to manufacture nanobranched pore (Figure 2.8). Even though we merely controlled the applied voltage in conventional electrolyte environment, the shapes of nanoscopically hierarchical structures were well

fabricated with pore diameter less than 100nm. In fact, it is difficult to fabricate these complex nanostructures by conventional lithography techniques. However, unconventional anodization is more simple and cost-effective method to fabricate various shapes of hierarchical nanostructures at a large area, overcoming many drawbacks of conventional lithographic techniques.

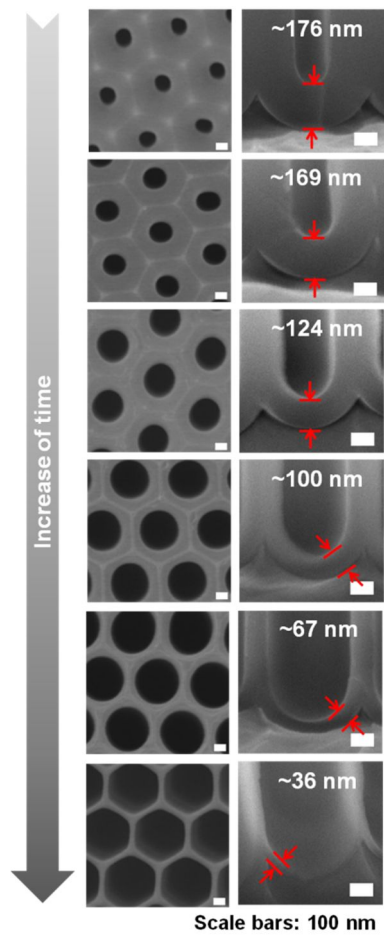


Figure 2.4. The change of barrier layer thickness with thinning process time.

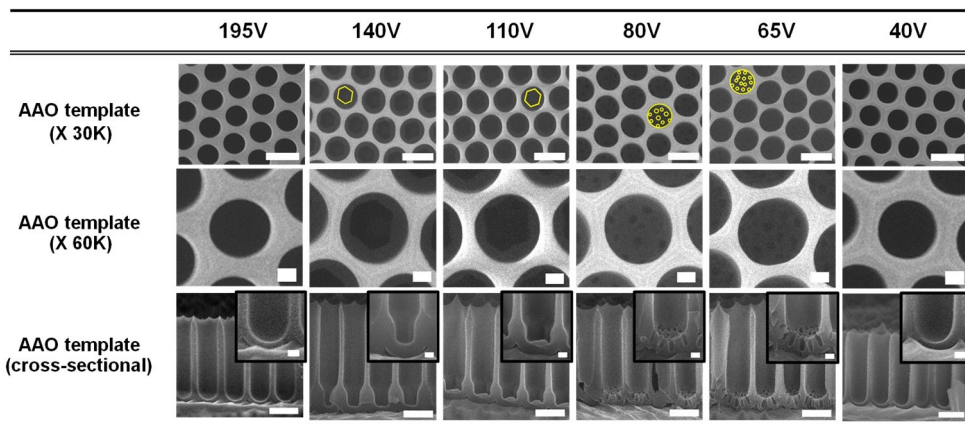


Figure 2.5. SEM images of hierarchical structures fabricated via the unconventional anodization. Scale bars are 500 nm (the first and third rows) and 100 nm (the second row and the inset in the third row).

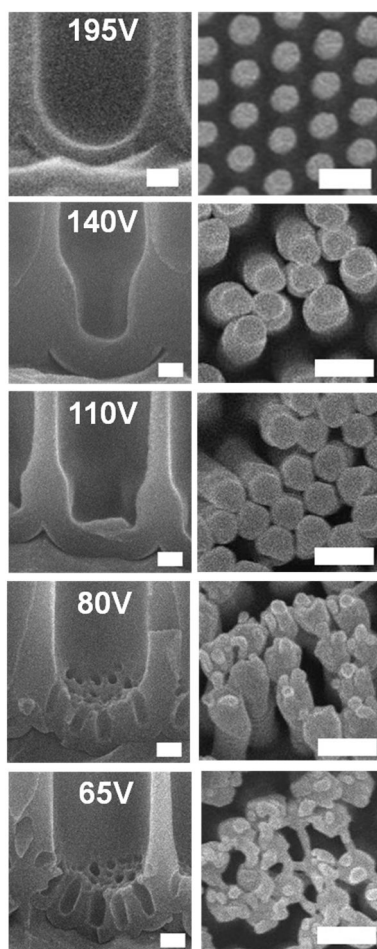


Figure 2.6. SEM images of hierarchical polymer nanostructures replicated from AAO templates. Scale bars are 100 nm (left) and 500 nm (right).

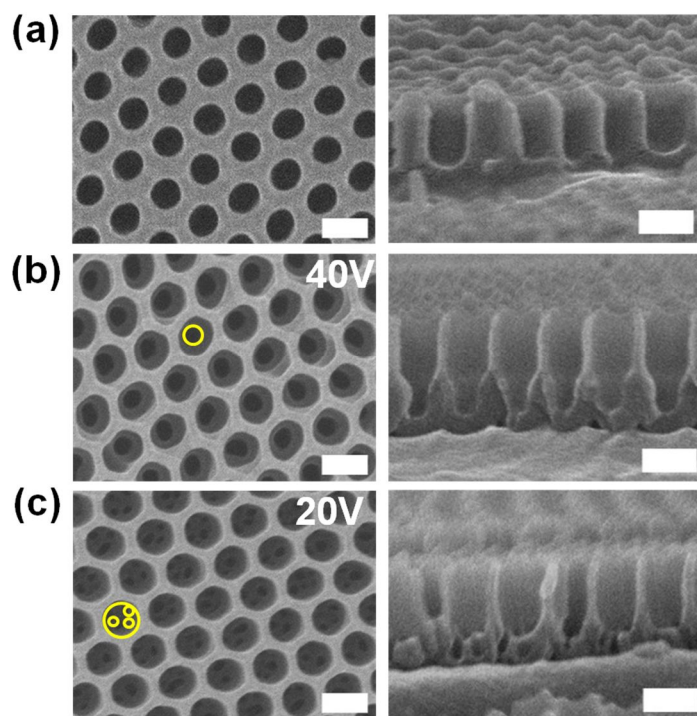


Figure 2.7. SEM images of hierarchical polymer nanostructures with $D_p < 100$ nm.

Scale bars are 100 nm.

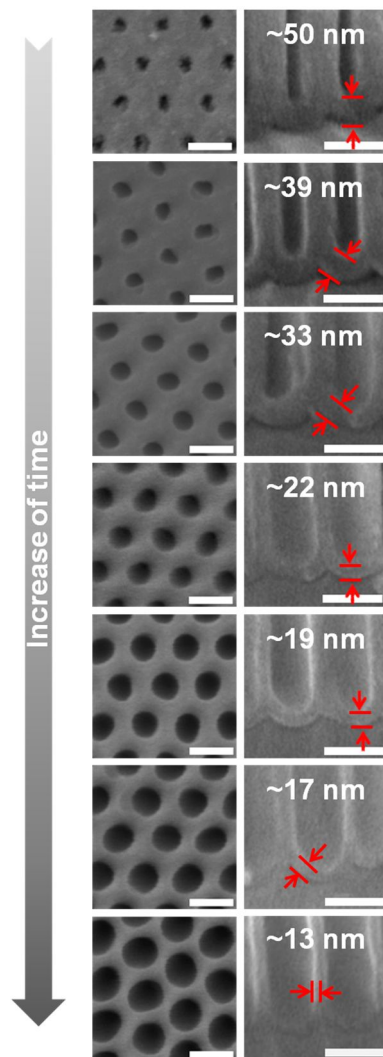


Figure 2.8. The change of barrier layer thickness with thinning process time. Scale bars are 100 nm.

Cylindrical nanochannel (nanohole) arrays can be promising in numerous industrial fields such as selective gas/ion exchange membranes or separation filters, pattern-transfer masks for e-beam evaporation, or reactive ion etching [13, 14]. In general, the AAO membrane consists of hexagonally packed nanopores and the bottom of each pore is closed by hemisphere-shaped oxide layer (barrier layer). It is necessary to eliminate the bottom barrier layer of nanopores in order to make an opened nanopore (nanochannel) array. There are three methods to open the barrier layer: wet chemical etching [15, 16], ion milling [17], and plasma etching [13]. For ion milling and plasma etching, even though the pores remain intact after the removal of barrier layer, these processes are required expensive equipment and it is possible to remove only a small area [15]. On the other hand, wet chemical etching can be a suitable method to open the barrier layer of AAO membranes because this method is convenient, inexpensive, and reliable [15]. In our study, the nanopore was opened by floating the membrane on 0.1M phosphoric acid solution at 60 °C, as shown in Figure 2.9 (a). Schematic illustration in Figure 2.9 (b) presents AAO membrane before (left)/after (right) the removal of bottom barrier layer of nanopores. To confirm whether the pore is opened, we measured water contact angle according to dissolution time (Figure 2.10). Water contact angle was decreased as the thickness of bottom oxide got thinner. When water contact angle was $<15^\circ$, the pore was completely opened and nanochannel arrays could be obtained. This result was good agreement with SEM images of the bottom layer.

From these results, we fabricated multi-scale nanochannel membrane via the unconventional anodization. Figure 2.11 presents that the membrane has two different nanochannel sizes. The top nanochannels of multi-scale membrane had the diameter of ~ 300 nm and the length of ~ 1 μm , and the opened bottom

nanochannels had the diameter of ~ 50 nm and the length of ~ 100 μm . The SEM images at the interface showed that the multi-scale (hierarchical) nanochannels were well-made. It can be applicable in membrane field because each nanochannel has different size and diffusivity.

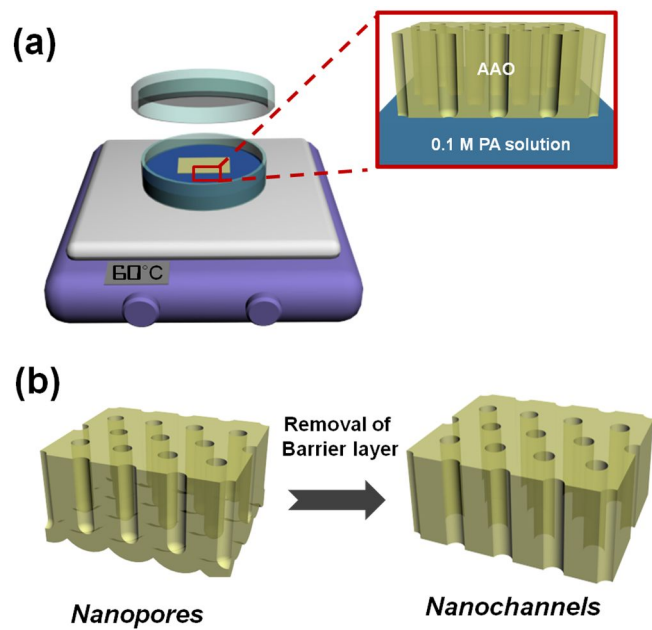


Figure 2.9. Schematic showing the fabrication of nanochannel membrane.

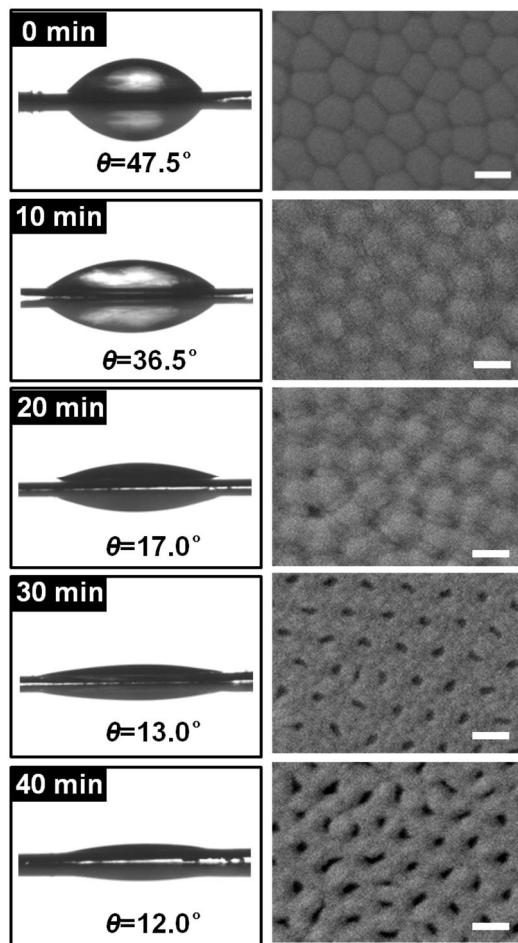


Figure 2.10. The change of water contact angle with the increase of dissolving time of barrier layer. Scale bars are 100 nm.

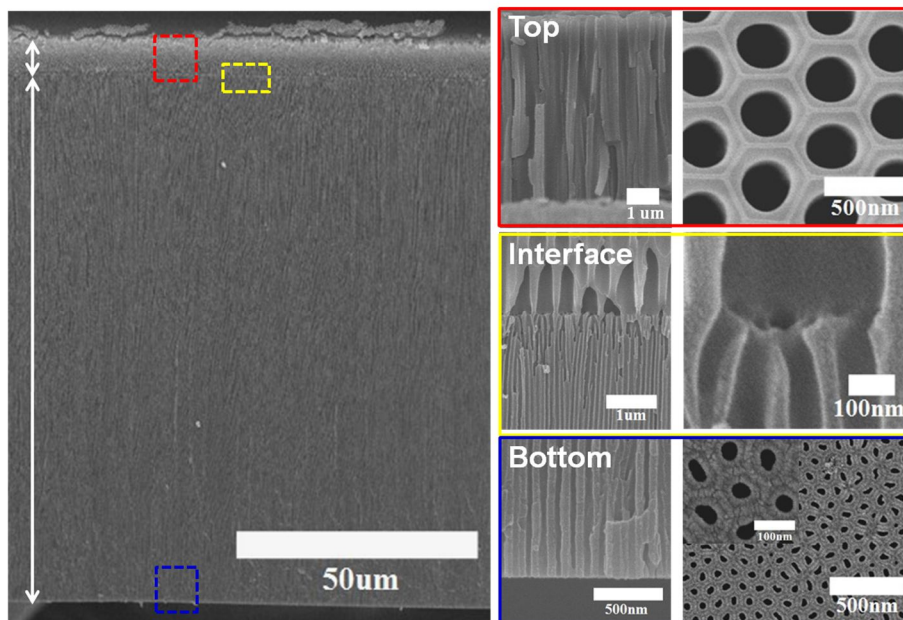


Figure 2.11. Multiscale nanomembrane obtained by the unconventional anodization.

2.4. Conclusion

In conclusion, we developed a simple method for the fabrication of various 3D (hierarchical) structures via sequential anodization. We controlled the shape and the number of nanobranches after thinning process of the barrier layer. One-branched AAO template was obtained at higher voltage (110V and 140V), and multi-branched AAO template was fabricated at lower voltage (65V and 80V). The very tiny hierarchical structures (< 100 nm) via unconventional anodization could be also fabricated in oxalic acid solution with the control of the thickness of barrier layer thickness and the applied voltage from 20V to 40V. It is noticeable to fabricate these complex nanostructures by unconventional anodization, overcoming the limitations of conventional lithography techniques.

2.5. References

- [1] A. Y. Y. Ho, H. Gao, Y. C. Lam, I. Rodriguez, *Adv. Funct. Mater.* **2008**, *18*, 2057.
- [2] R. Krishnan, C. V. Thompson, *Adv. Mater.* **2007**, *19*, 988.
- [3] W. Lee, R. Ji, U. Gosele, K. Nielsch, *Nature Mater.* **2006**, *5*, 741.
- [4] W. Lee, J. C. Kim, U. Gosele, *Adv. Funct. Mater.* **2009**, *20*, 21.
- [5] W. Lee, K. Schwirn, M. Steinhart, E. Pippel, R. Scholz, U. Gosele, *Nature Nanotech.* **2008**, *3*, 234.
- [6] G. W. Meng, Y. J. Jung, A. Y. Cao, R. Vajtai, P. M. Ajayan, *Proc. Natl. Acad. Sci. USA* **2005**, *102*, 7074.
- [7] C. Greiner, E. Arzt, A. del Campo, *Adv. Mater.* **2008**, *20*, 1.
- [8] A. del Campo, E. Arzt, *Micromol. Biosci.* **2007**, *7*, 118.
- [9] O. Jessensky, F. Muller, and U. Gosele, *Appl. Phys. Lett.* **1998**, *72*, 1173.
- [10] S. Ono, M. Saito, M. Ishiguro, and H. Asoh, *J. Electrochem. Soc.* **2004**, *151*, B473.
- [11] Z. X. Su, G. Hahner, and W. Z. Zhou, *J. Mater. Chem.* **2008**, *18*, 5787.
- [12] M. S. Hunter, P. Fowle, *J. Electrochem. Soc.* **1954**, *101*, 481.
- [13] J. Y. Liang, H. Chik, A. J. Yin, J. Xu, *J. Appl. Phys* **2002**, *91*, 2544.
- [14] H. Masuda, K. Yasui, K. Nishio, *Adv. Mater* **2000**, *12*, 1031.
- [15] C. Y. Han, G. A. Willing, Z. L. Xiao, H. H. Wang, *Langmuir* **2007**, *23*, 1564.
- [16] J. J. Schneider, N. Engstler, K. P. Budna, C. Teichert, S. Franzka, *Eur. J. Inorg. Chem.* **2005**, 2352.
- [17] T. Xu, G. Zangari, R. M. Metzger, *Nano Lett.* **2002**, *2*, 37.

Chapter 3.

Nature-Inspired Nanostructures and Their Properties*

*This chapter is based in part on two papers from Kyunghee Lee, Youn Sang Kim, and Kyusoon Shin, *Macromolecular Research* **2012**, *20*, 762-767, Copyright (2012) Springer, and Moon Kee Choi, Hyunsik Yoon, Kyunghee Lee, and Kyusoon Shin, *Langmuir* **2011**, *27*, 2132-2137, Copyright (2011) American Chemistry Society.

3.1. Introduction: Biomimetics

There has been extensive research on the mimicking of microscopic structure in nature. One of recent trend must be the simulation of asymmetric or hierarchical multilength-scale structure [1-3]. Hierarchical structures consisting of micrometer or nanometer scale structures have been discovered in many plant leaves and insect wings or legs, and exhibited superior properties on their surfaces (Figure 3.1) [4-7]. For example, the surface of lotus leaves with micrometer-scale roughness and submicrometer-sized asperities composed of epicuticular waxes exhibits extreme water repellent properties [8-10], and the surface of gecko's foot with micrometer and nanometer hairs reveals outstanding adhesion behaviors [11-14]. Thus, there has been a great deal of effort for mimicking unique hierarchical structures synthetically in order to realize their exceptional properties [15].

The artificial nature-inspired structures have been developed by many techniques such as photolithography [16], soft lithography [17, 18], plasma etching [19], chemical etching [20], and so on [21, 22]. Among various techniques, attention on anodic aluminum oxide (AAO) has been drawn as a candidate of template for the manufacture of artificial biomimetic structures, because it has structural regularity, uniform periodicity, and high density as well as availability of economic production [23-29]. In addition, the size of nanopores is easily tuned on a wide range, because experimental parameters for the formation of nanopores such as the type of electrolyte and the applied voltage is relatively well established and easy to control. However, there have been few reports where nonlinear multilevel-structured AAO templates have been created. One of innovative work was done by

Meng *et al.* who reported the fabrication of branched nanopores via voltage drop [30]. After the first anodization to form a stem pore, the applied voltage is slowly reduced, and then a stem pore is divided to branched pores. Recently, Ho *et al.* reported the fabrication of the multitiered AAO template by sequentially stepping down the anodization potential after etching the barrier layer partially [31]. They investigated the processing parameters in the sequential anodization.

Mimicking nature-inspired multilevel structures can be substantiated by the replication from the template like the AAO with multilevel structure. Replication by polymers should be a possibility, and it can be done by infiltrating polymers into the porous template in order to obtain polymeric nanopillars or nanotubes in the melt state above the glass transition temperature. However, this method generally requires the removal of the AAO template by wet-etching with strong acid or/and base to obtain polymer nanostructures. Thus, it would be very useful to reuse the nanotemplates by obtaining the polymeric nanostructures without deteriorating the nanotemplates [32-34]. Poly(dimethylsiloxane) (PDMS) can be a solution for obtaining nanostructures from the mater template without the removal of master template [35]. Since PDMS has a low surface energy ($\sim 20 \text{ erg/cm}^2$), it usually facilitates easy release of PDMS from the mold. Additional advantage of the demolding method by peeling-off over wet-etching is that it avoids pairing adjacent polymer nanostructures by capillary condensation. Despite the advantages of PDMS, this material suffers from a serious drawback, low permeability to some nanoscopic molds due to poor wettability of prepolymer on the surface of nanotemplate. Moreover, it sometimes requires the anti-adhesion coating on the surface and wall of the mold for easy release and replication of fine structures. Therefore, application of this material to fabricate nanostructures can be restricted

in some cases.

In this chapter, we deal with the fabrication method of nature-inspired (hierarchical) nanostructures by anodization and their properties: mimicking lotus leaf surface in chapter 3.2 and gecko's foot surface in chapter 3.3.

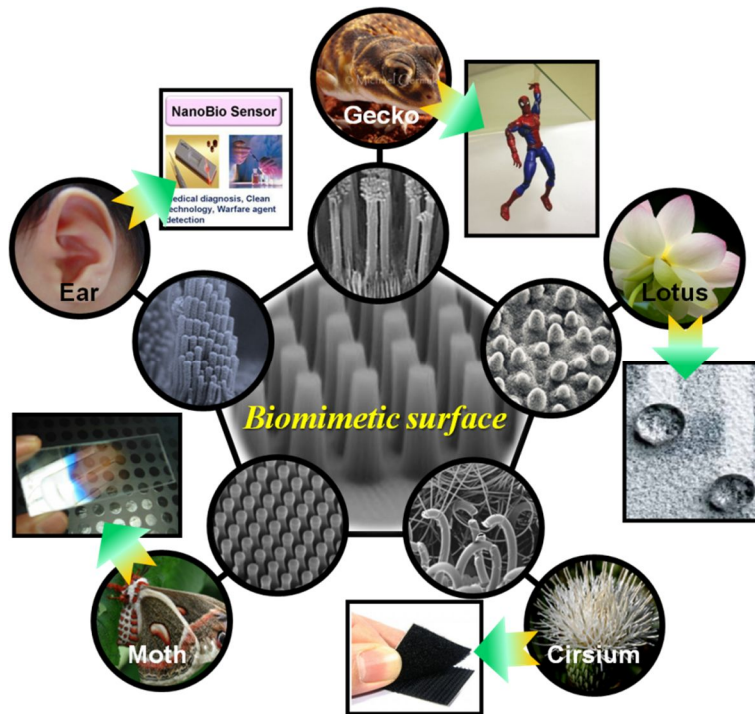


Figure 3.1. Various examples of biomimetic surface discovered in nature.

3.2. Mimicking Lotus Leaf Surface

3.2.1. Experimental Section

Among the superb properties induced by hierarchical structures, the wettability control of a solid surface through geometric surface structures has been of great importance for fundamental understanding of surface and practical applications in the generation of functional surface. However, few studies about the reproduction of hierarchical structures have been reported, as compared to the diverse structures found in many water-repellent plants (~200 species). In this study, we investigate a method of manufacturing diverse multilength-scale artificial water-repellent polymeric structures by the replication AAO templates that also have hierarchical structures through the control of anodization voltages and the type of electrolyte. In order to replicate the fine minute structures with high fidelity and to reuse the AAO template, photocurable perfluoropolyether (PFPE) has been suggested to replace PDMS. PFPE, which is liquid at room temperature, exhibits high permeability as well as low surface energy [36]. It is suitable to obtain tiny nanostructures from the master mold without any anti-adhesion layer. Thus, PFPE was used to obtain repetitive hierarchical structures with the reuse of AAO templates. Figure 3.2 represents schematic illustrations for the preparation of nature-inspired hierarchical polymer nanostructures. Hierarchically structured AAO template was fabricated via anodization, and photocurable PFPE replica was replicated from the AAO template. Nanoscopically ordered concave Al surfaces (periodicity~500 nm) were obtained after the first anodization of Al film in 0.1M phosphoric acid solution at 195V and selective etching of nanoporous alumina layers. Then, we fabricated nanoscopic

branched pores on the etched surface of Al by anodizing with the applied voltage ranging from 40V to 195V in a suitable electrolyte. After the fabrication of AAO template with hierarchical nanostructures, PFPE replica was obtained via photocuring ($\lambda \sim 365$ nm) for 4 hrs, and the replica was released from AAO template. Any chemical coating of AAO template such as a PDMS anti-adhesion layer was not applied, because hydrophobic-nature of PFPE made the release of PFPE easy. Experimental details are as follows.

Fabrication of hierarchical AAO template:

A high purity Al sheet (99.999% thickness ~ 0.5 mm, Goodfellow) was electropolished in a mixture of perchloric acid and ethanol (HClO_4 : $\text{C}_2\text{H}_5\text{OH}$ =1:4 in volumetric ratio) at 20V and 4 °C to reduce surface roughness. The first anodization was carried out in dilute 0.1M phosphoric acid ((H_3PO_4) (85%, Aldrich) at 195V and 0°C. After the first anodization, the nanoporous alumina layer was etched away with a mixture of chromic acid (H_2CrO_4) and phosphoric acid solution at 65 °C. The etched Al was subsequently anodized in phosphoric acid or oxalic acid ($\text{H}_2\text{C}_2\text{O}_4$) solution at different voltages (40-195V) for several minutes to manufacture hierarchical nanostructures. In order to obtain one-branched hierarchical nanopores, the etched Al was anodized at the same condition as the first anodization for 10-20 min. Nanoscopic multiple pores in a pore were fabricated by subsequent anodization in phosphoric acid or oxalic acid solution at different voltages (40-140V) for several minutes. Then, the nanopores were widened by immersion of alumina in a 0.1M phosphoric acid solution at 30 °C for 10-30 min. To obtain nanobranches in a cylindrical nanopore, when anodization

was carried out in 0.3M oxalic acid solution at 80V for a few minutes in the formation of branched pores, thinning of the barrier layer was preceded before anodization.

Fabrication of PFPT replica from AAO template:

Bifunctional perfluoropolyether (PFPE)-urethane methacrylate (MD700, Solvay Solexis, Italy) ($M_n = 3800$ g/mol) was employed. Darocur 1173 (2-hydroxy-2-methyl-1-phenylpropan-1-one), purchased from Ciba Specialty Chemicals (Switzerland), was added as a photoinitiator to the prepolymer at 4.0 wt%. Then, the photocurable prepolymer was poured onto nanoporous AAO templates, and polyethylene terephthalate (PET) film (thickness~50 μm) was covered on the PFPE prepolymer layers. Here, PET film functioned as a rigid substrate and a blocking layer against the permeation of air gas which could be interfere with UV curing. The PFPE prepolymer layers on AAO template were irradiated with UV light ($\lambda \sim 365$ nm) for a few hours to form crosslinked PFPE networks. After UV curing, the PFPE replica was slowly detached from the AAO template with constant speed.

Fabrication of PUA or TPT polymer replica from AAO template with anti-adhesion coating:

We also employed photocurable polyurethane acrylate (PUA, Minuta Tech.) and trimethylolpropane propoxylate triacrylate (TPT, Aldrich). Unlike PFPE, PUA and TPT were required surface modification of nanopores to separate from nanoporous AAO template. Thus, the AAO template was treated with oxygen plasma at 30W with the gas flow rate of 10.3 sccm for 2min at 100-200 mTorr (RIE-3000, South Bay Technology, Inc.). The AAO template was immersed in a 0.5 wt% aqueous of

3-(aminopropyl triethoxysilane) (APTES, Aldrich) for 10 min. Unreacted APTES was washed with distilled water. Then, the APTES-treated templates was reacted with monoglycidyl ether-terminated poly(dimethylsiloxane) (PDMS, $M_n = 5000$, Aldrich) at 80°C for 4hr. To remove unreacted PDMS and form PDMS monolayer as an anti-adhesion layer, the templates were immersed in isopropyl alcohol with sonication for 1 min. The thickness of PDMS was less than 10 nm. The curing process of PUA to obtain replica was similar to that of PFPE. PUA or TPT was drop cast onto PMDS-coated AAO template, and PET film was placed on the PUA or TPT layer. Then, the PUA or TPT layers on the AAO template were irradiate with UV light as same condition of PFPE photocuring as explained above. The PUA or TPT replica surface was modified with PDMS again to reduce surface energy via the same reaction with anti-adhesion coating of AAO template.

The analysis of structure of AAO and PFPE nanorods:

The structure of AAO template and PFPE, PUA, TPT replica were analyzed by field-emission scanning electron microscopy (FE-SEM, JSM-6701F, JEOL) after deposition of platinum with the thickness of a few nanometers to prevent electron charging.

Water contact angle measurement:

The static contact angles of distilled water on flat and hierarchical PFPE surfaces were measured with Kruss DSA 10 contact angle analyzer. The droplet volume was 4 μ l. The contact angles were measured more than 5 times for each sample at different regions.

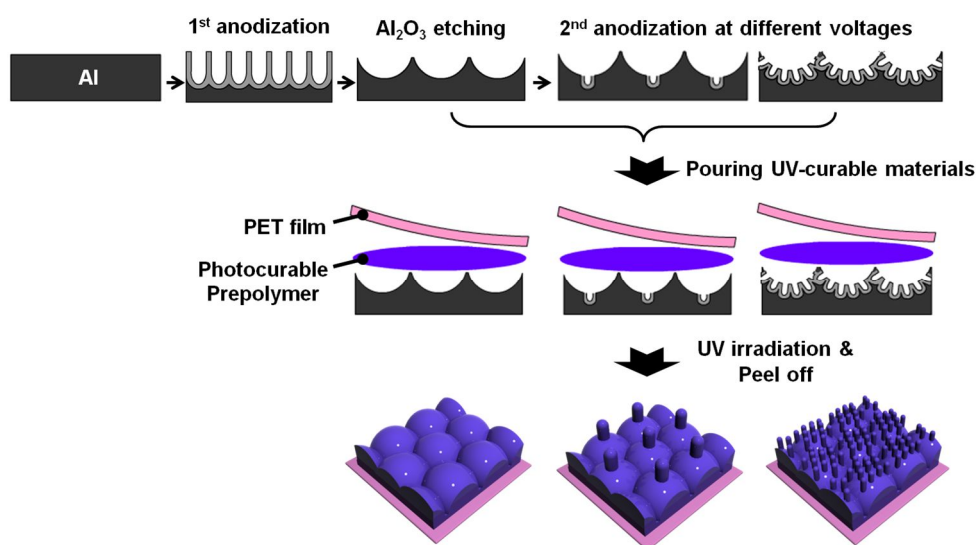


Figure 3.2. Schematic illustration of hierarchical polymeric nanostructures using AAO template.

3.2.2. Results and Discussion

Water-repellent leaf surfaces have been discovered in a few hundreds of plant species, and most species have micromorphological diversity on their surfaces. Figure 3.3 shows the examples of the morphology of water-repellent plants (*e.g.* *Colocasia esculenta*, *Lupines polyphyllos*, *Gladiolus watsonioides*, *Hygoryza aristata*, and *Alchenilla duplophylla* in ref. [6]) and artificial biomimetic polymer nanostructures fabricated by anodization process in this study (from (a) to (e)). Each species has hierarchical structures on its surface with diverse microscopic morphologies. Despite the different structures, it has reported that contact angles of these surfaces are found to be more than 150° for all surfaces. We fabricated various hierarchical nanostructures in order to investigate the effect of surface morphology on the surface wettability. The morphology of artificial polymer surfaces is analogous with that of water-repellent plant leaves in nature.

The SEM images of hierarchical AAO template and PFPE replica replicated from AAO is given in Figure 3.4. First of all, the top-view and cross-sectional SEM images of AAO templates in Figure 3.4 show that one- or multi-branched structures are well developed on the etched Al surface that was anodized at 40, 60, 80, 120, 140, and 195V (top-view images: the first and second rows and cross-sectional images: the third row). In general, it is possible to control the interpore distance and nanopore diameter by the variation of applied voltage in the anodization process. The choice of electrolyte and its concentration are also influential in the formation of nanopores. The etched surface with ~500 nm of periodicity was obtained in a 0.1M phosphoric acid solution at 195V. Subsequently, one-branched (or cylindrical) AAO template was manufactured at same conditions as former

anodization ones. The nanoscopic branched pores on the concave Al surface were also obtained by sequential anodization. The number of branches was controlled by the anodization voltage and the electrolyte itself. Fewer numbers of branches were formed in a 0.1M phosphoric acid solution at 120 and 140V, and larger numbers of branches were formed in a 0.3M oxalic acid solution at 40, 60, and 80V. As the applied voltage decreased, more branches were formed on the etched Al surface, and the barrier layer became thinner because of narrower interpore distance. The cross-sectional SEM images of the third row in Figure 3.4 show that the number of branches was thoroughly determined by the applied voltages. It is also found that the length of branches were almost similar (< 150 nm) for all samples. PFPE replicas were highly replicated from hexagonally ordered AAO template (the fourth row in Figure 3.4). The one-branched surface was observed, when the anodization voltage of 195V and 140V. The shape on convex pattern was rather a short cylinder or hexagonal prism. PFPE surface, replicated from the AAO anodized at 120V, looks like a doughnut. When the anodization voltage was 80V, branches were uniformly formed on the convex Al surface. However, when the anodization voltage was 40 or 60 V, PFPE branches were partially replicated. Since branched nanopores obtained at 40 and 60V were so narrow and complicated, it is thought that PFPE nanobranches were damaged upon pulling out.

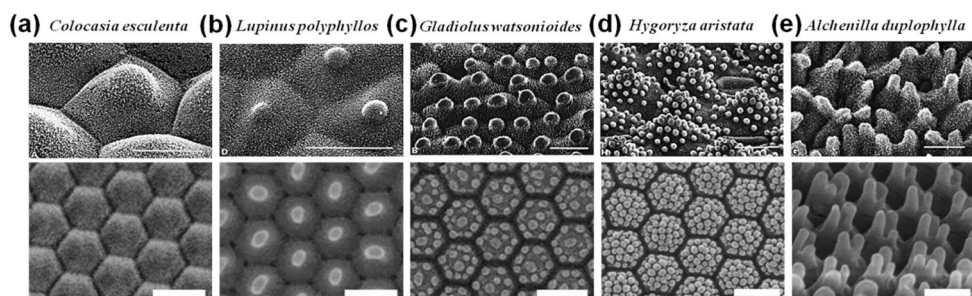


Figure 3.3. The morphology of various water-repellent plants [Reproduced from ref. 6. Copyright (1997) Oxford University Press] and artificial biomimetic polymer surfaces manufactured in this study: (a) *Colocasia esculenta*, (b) *Lupines polyphyllus*, (c) *Gladiolus watsonioides*, (d) *Hhygoryza aristata*, and (e) *Alchenilla duplophylla*. Scale bars= 20 μm for (a), (c)-(e) and 50 μm for (b) in the first row, and scale bars= 500 nm in the second row.

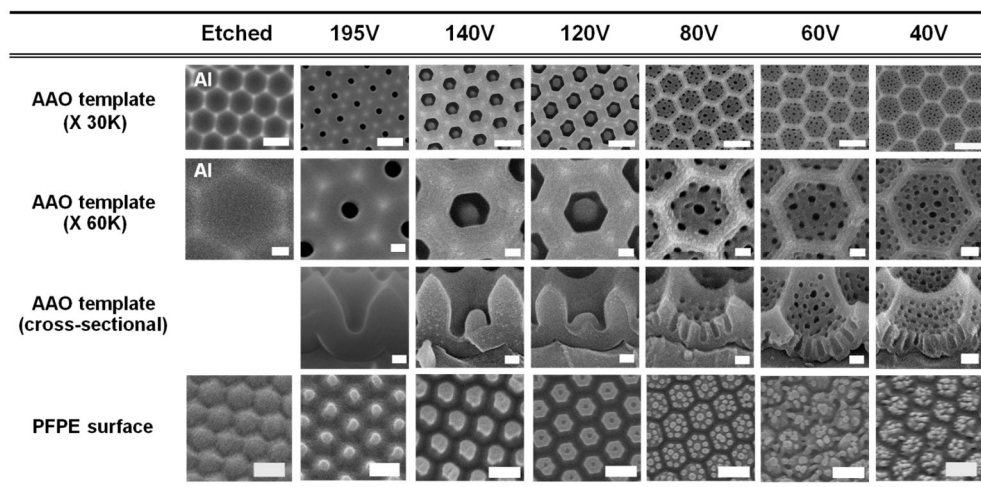


Figure 3.4. The SEM images of nanoscopic hierarchical structured AAO templates and PFPE rods. The top-view SEM images of etched (concave) Al surface and hierarchical AAO templates with the low magnitude (the first row, scale bars=500 nm) and the high magnitude (the second row, scale bars=100 nm), and the cross-sectional SEM images of hierarchical nanopores (the third row, scale bars=100 nm). The SEM images of convex PFPE surface and hierarchical nanostructures replicated from AAO templates are also given (The fourth row, scale bars=500 nm). The top row indicates the anodization voltage (40-195V) with the chemically etched Al that is given at the first left column.

We characterized water contact angles of nanoscopically hierarchical polymer surfaces to investigate the influence of surface structures on the surface wettability. Figure 3.5 represents that the wettability of a flat PFPE surface and hierarchical surfaces fabricated by sequential anodization process. The values of x -axis in the graph indicate the value of subsequently applied voltages to form branches. Water contact angle of a flat PFPE surface was $\sim 109.2^\circ$. The convex-patterned surface obtained from etched Al surface got more hydrophobic, as compared to a flat PFPE surface. Due to hexagonally well-ordered patterns with a periodicity of a few hundreds of nanometers, the water contact angles were increased around 20° . Upon the introduction of branches on the convex surfaces, the contact angle values were higher than 140° . Especially, in the presence of branches subsequently formed at the anodization voltage of 40, 60, and 80V on the surface of convex pattern, the water contact angles were slightly increased to $\sim 145^\circ$.

Figure 3.6 shows the surface morphology of PUA nanostructures replicated from AAO template and their surface wettability. SEM images show that each nanostructure is successfully replicated from AAO template. As the nanostructures are introduced to the surface, the water contact angle gets $\sim 20^\circ$ higher than that on flat surface. In addition, the surface with hierarchical nanostructures has $\sim 10^\circ$ higher value of contact angles than that on convex surface. Figure 3.7 displays the surface wettability of TPT nanostructures as well as the surface morphology of each TPT nanostructure replicated from AAO template. TPT nanostructures were also completely replicated from AAO template. Similar to the wettability trend of PFPE and PUA, the water contact angle on TPT nanostructured surface becomes much higher ($\sim 60^\circ$) than that on flat surface, as shown in Figure 3.7. Interestingly,

the highest water contact angle was discovered on a doughnut-shaped nanostructure surface obtained at 120V. It was expected that more air could be trapped on the doughnut-shaped surface because of structural peculiarity. But, we could not observe the noticeable wettability difference by the variation of the number of branches on convex pattern regardless of polymer types. However, it was obvious that nanoscopic branches acted as a factor to increase surface hydrophobicity.

We also investigated the wettability on PFPE, PDMS-coated PUA, and PDMS-coated TPT surface with various hierarchical structures. In Figure 3.8, PDMS-coated PUA and PDMS-coated TPT nanostructures were employed to compare with the wettability on PFPE nanostructures. PDMS is well-known as a hydrophobic material with low surface energy. The water contact angle of flat PFPE, PDMS-coated flat PUA and PDMS-coated flat TPT surface replicated Si wafer was 109.2° , 108.2° , and 104.5° respectively. The water contact angle of PDMS-coated flat PUA surface was similar to that of flat PFPE surface. The etched surface of these polymers got more hydrophobic than flat surface due to highly ordered convex nanopattern on surface, so the water contact angles were increase around $\sim 20^\circ$. In addition, according to the introduction of nanobranches on convex surface, water contact angles were increase above $\sim 30^\circ$ than flat surface regardless of the kind of polymeric materials. From these results, PUA or TPT (relatively less hydrophobic) nanostructured surfaces can be tuned to more hydrophobic surfaces through PDMS coating. After PDMS coating, the increase of water contact angle on PUA or TPT nanostructured surface (average increment of water contact angle $\sim 10^\circ$) can be interpreted by the combination effect of structural factor and chemical factor.

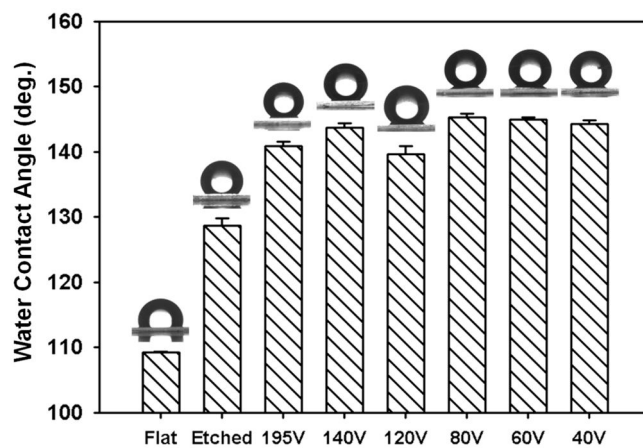


Figure 3.5. Water contact angles of flat, convex, and hierarchical PFPE surfaces.

The “Etched” surface was obtained from etched Al.

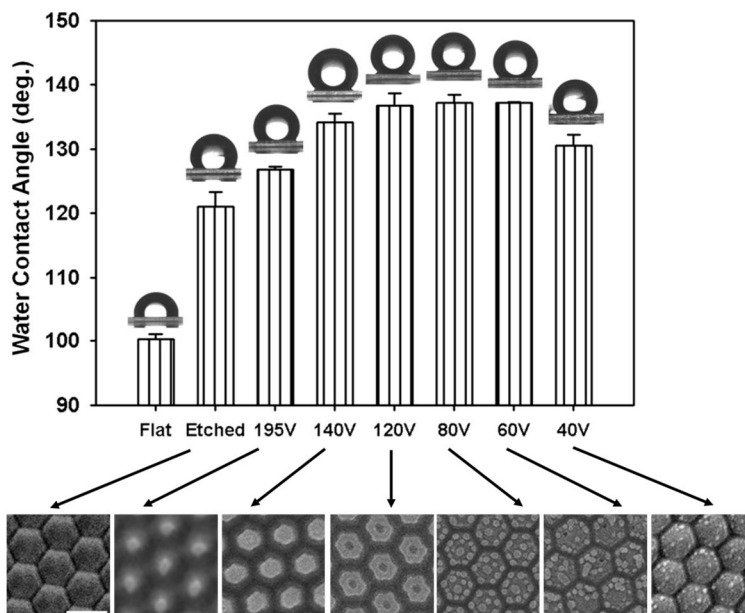


Figure 3.6. Water contact angles of flat, convex, and hierarchical PUA surfaces with SEM images of each nanostructures. Scale bar= 500 nm.

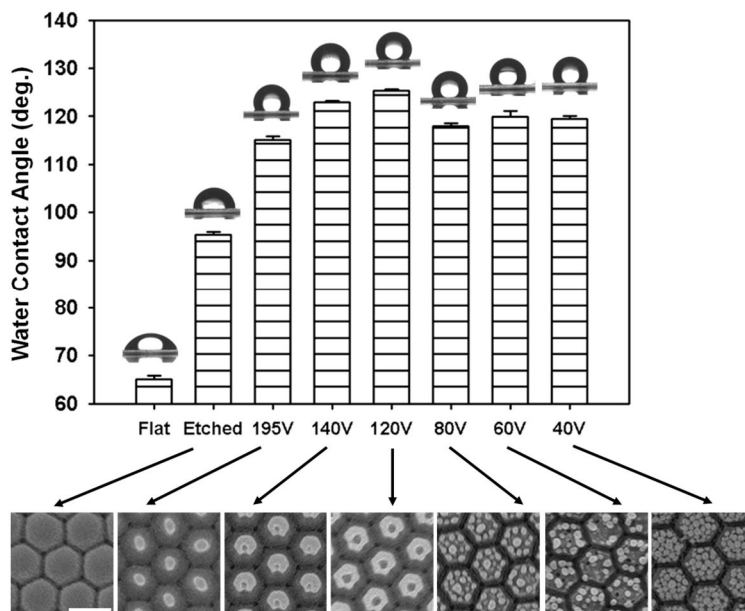


Figure 3.7. Water contact angles of flat, convex, and hierarchical TPT surfaces with SEM images of each nanostructures. Scale bar= 500 nm.

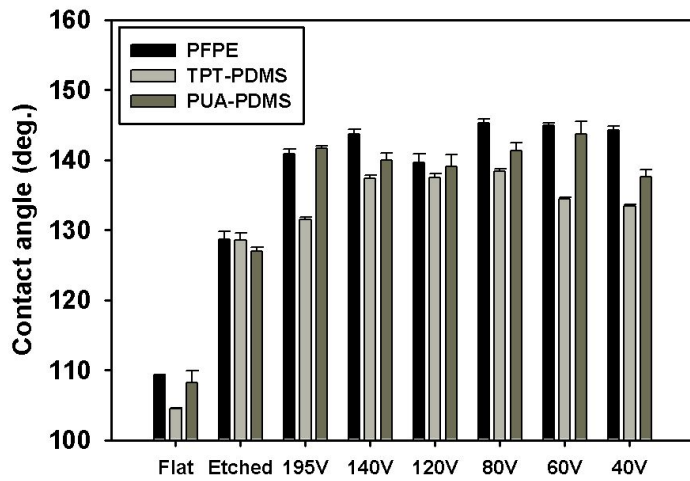


Figure 3.8. Comparison of water contact angles on PFPE, PDMS-coated PUA, and PDMS-coated TPT surfaces.

To improve surface hydrophobicity we fabricated hierarchical structures consisting of larger nanopillar with the height of a few micrometers and smaller branches with the diameter of a few tens or hundreds nanometers. Schematic route to the hierarchical structures is depicted in Figure 3.9 (a). In this study, we firstly made nanobranched AAO template by subsequent anodization after thinning of barrier layer. The thickness of barrier layer changed from 176 nm to 67 nm after the thinning process (Figure 2.4 in chapter 2). The formation mechanism of nanobranched pores at the bottom of nanopores were subsequently formed at 80V in 0.3 M oxalic acid solution. The SEM images in Figure 3.9 (b) show the top and cross-sectional view of hierarchical AAO template (top and middle) and nanostructured PFPE surfaces replicated from the AAO template (bottom). The yellow line represents the schematic indication of nanobranched in a stem pore. The second column presents high magnitude of SEM images. The lengths of stem pores and nanobranched were $\sim 1.3 \mu\text{m}$ and $\sim 200 \text{ nm}$, respectively. Hierarchical PFPE nanorods were slightly collapsed each other because of inherent low modulus of PFPE. We investigated the wettability of cylindrical and hierarchical PFPE nanostructured surfaces. The contact angle of cylindrical nanorods was found to be $\sim 140^\circ$. However, as several nanobranched were formed on the top of a stem nanorod, the water contact angles were $\sim 152^\circ$, comparable value with water-repellent leaf surfaces. As the stem pillar becomes longer and larger nanopillar in the hierarchical structures, so did slightly enhance the surface hydrophobicity.

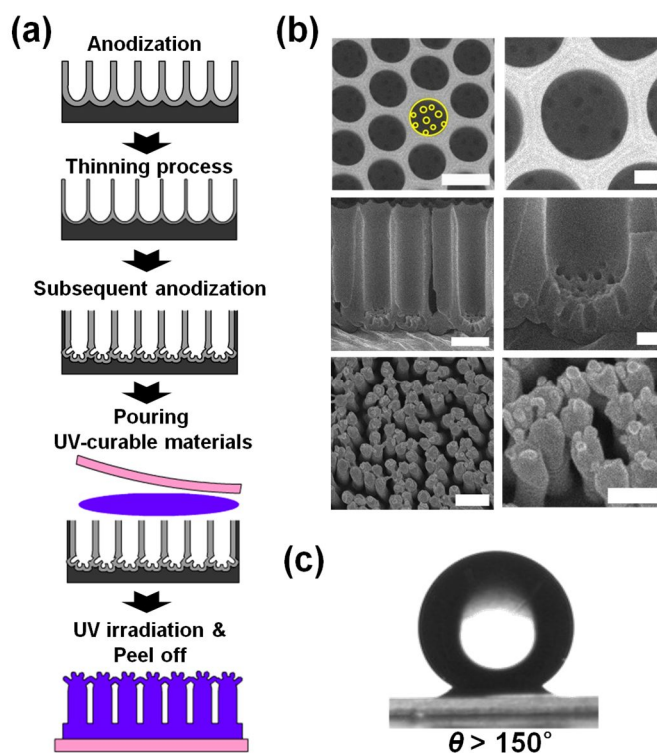


Figure 3.9. The hierarchical nanopillar surface: (a) schematic route to nanoscopic branches in a nanopore, (b) top and cross-sectional SEM images of hierarchical structures of AAO template (the first and second row, scale bars= 500 nm (left) and 100 nm (right)) and PFPE (the third row, scale bars= 1 μ m (left) and 500 nm (right)), and (c) the water contact angle of hierarchical nanopillar surface.

3.3. Mimicking Gecko's Foot Surface

3.3.1. Experimental Section

Gecko's foot have been shown a hierarchical structure, consisting of microscopic angled hairs called setae and hundreds of nanoscopic structures called spatulas on the tips of setae [37]. These structures on gecko's foot surface have shown high interfacial adhesion. In our study, there are two different approaches to mimic gecko-inspired structures: hierarchical nanostructures and asymmetric nanopillars. Firstly, hierarchical PS nanostructures with diverse shapes were replicated from hierarchical AAO template obtained by the unconventional anodization process. Secondly, asymmetric nanopillars were manufactured by oblique deposition of metal on cylindrical nanopillar replicated AAO template. Experimental details are as follows.

Fabrication of AAO template:

- (1) One-dimensional AAO: The experimental process for the preparation of typical AAO template was well described in chapter 1.1.
- (2) Hierarchical AAO: The experimental process for the preparation of hierarchical AAO template was well described in chapter 2.2 and chapter 3.2.

Fabrication of polymer replica from AAO template:

- (1) One-dimensional polymer nanostructures: Polyurethane acrylate (PUA, Minuta tech.) was used. The PUA replica was obtained from surface-modified AAO template. Experimental details are explained in chapter 3.2.

(2) Hierarchical polymer nanostructures: The home-made nanoporous membrane was filled with a polystyrene melt (M.W. \sim 280K, Aldrich) at 180 °C under vacuum. The polystyrene (PS) nanorod arrays were obtained after the remaining Al and alumina layers were dissolved in a cupric chloride solution and sodium hydroxide solution, respectively.

Fabrication of asymmetrically bent nanopillars:

One lateral side of the polymer nanopillars was coated with gold (Au, thickness \sim tens of nanometers thick) by oblique thermal evaporation. The deposition rate was 1 Å/s under high vacuum (10^{-6} Torr). Janus nanopillars were bent towards the Au-deposited side and their curvature was dependent on the thickness of Au layer.

Adhesion measurement:

(1) Asymmetrically bent nanopillars: The shear adhesion strength of the nanopillars was measured by a hanging test. Dry adhesion patch (1 cm \times 2 cm) was attached against a Si surface under a preload of 0.1 N/cm².

(2) Hierarchical nanopillars:

For adhesion measurements a commercial atomic force microscopy (Digital Instruments) was used. Silica balls with radius of 2.5 μ m were mounted on a Au-coated triangular Si₃N₄ cantilever with a nominal spring constant of 0.58 N/m. Adhesive force was measured using a single point measurement of a force calibration plot.

3.3.2. Results and Discussion

We fabricated various shape of hierarchical nanostructures such as convex, double-embossed, triple-embossed, one-dimensional, and multi-branched surfaces to demonstrate the influence of nanobranches. Figure 3.10 shows the design to make gecko-inspired structures by multi-step anodization. Then, adhesive property of each nanostructured surface can be analyzed by atomic force microscopy (AFM). The interaction between the tip with Au particle and sample surface can be described by force-distance curves in Figure 3.11. The force changes, as the sample surface approaches the tip. At non-contact region (large separation), there is no interaction, so the force is zero. The sample surface contacts with the tip due to attractive van der Waals interaction. When the sample is further moved towards the tip, the total force acting on the cantilever becomes repulsive. As the sample is retracted (contact region in the diagram), the force is reduced along the linear line. Below the zero force line, the net force acting on the cantilever becomes attractive because the tip is held at the sample surface due to adhesion.

We firstly measured the adhesive properties on PS bulk film, PS thin film (thickness <100 nm), and one-dimensional PS film. When nanorods are introduced to PS surface, the adhesive force decreases (Figure 3.12). In order to investigate the nanoscopic structure effect, the adhesive force on convex surfaces with different wavelength (interpore distance) was measured. When the wavelength of convex surface gets smaller from 500 nm to 70nm, the adhesive force increases, but it is still lower than that on thin film (Figure 3.13). In addition, we observed that the structural hierarchy can reduce the surface adhesive properties, as shown in Figure 3.14. Double-embossed nanostructures have lower adhesion than that on convex

structures regardless of the wavelength (Figure 3.14 (a)). When the PS surface has triple-embossed nanostructures, the adhesive force is slightly increased (Figure 3.14 (b)). But, it is apparent that the structural complexity interrupts to realize gecko-like surface in current study. Thus, we manufactured hierarchical structures with nanobranches on the tip of stem nanorod (length $\sim 1\mu\text{m}$). Even though this structure is more similar to natural gecko's foot surface, the adhesive force gets lower than that on one-dimensional nanostructures (Figure 3.15). This adhesion decline can be explained by the reduction of contact area between Au particle on the tip and the sample surface as nanostructures are introduced on the PS surface. The schematic illustration in Figure 3.16 helps to understand the contact area at the Au particle/nanostructure interface. This analogous phenomenon was previously reported by Burton and Bhushan [38]. They fabricated poly(methyl methacrylate) (PMMA) nanopillar arrays and analyzed the adhesive force with varying tip radius (Figure 3.17 (a)). For increasing tip radius, the adhesive force on flat PMMA film increases (Figure 3.17 (b)). With a larger radius, the real contact area increases and the adhesive force also increases. In addition, they observed the adhesive force on PMMA nanopillars is lowered than that of the PMMA film sample (Figure 3.17 (c)). This is because of the decrease in real contact area for each tip radius from a flat film. From this report, we conjectured that our efforts to mimic gecko-inspired structure did not provide an enhanced adhesive property due to the decrease of the contact area at the Au particle/nanostructure interface.

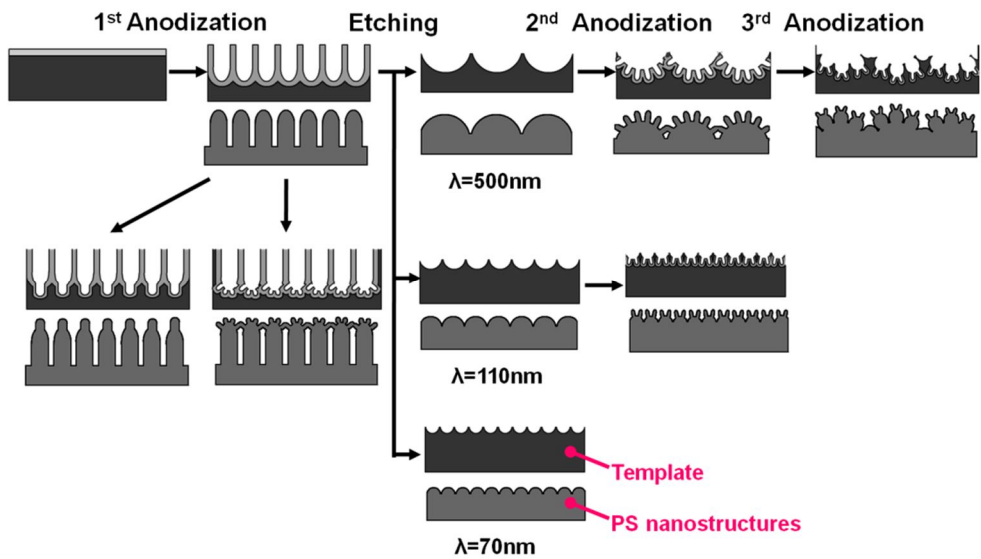


Figure 3.10. Schematic route to hierarchical polymeric nanostructures obtained from etched Al films or AAO template.

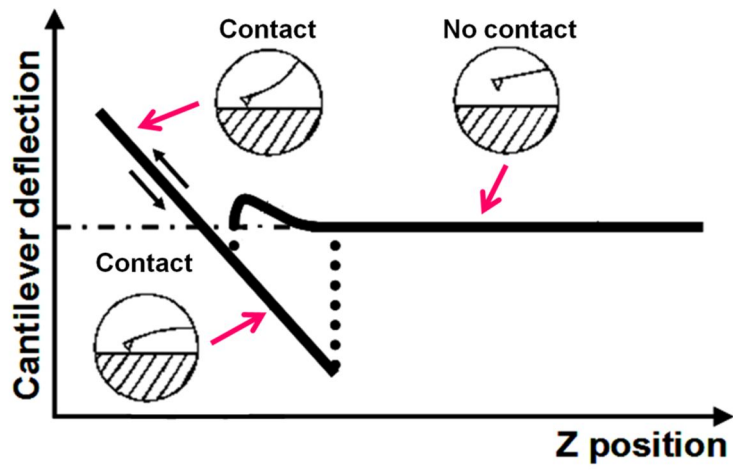


Figure 3.11. Force-distance curve depicting the interaction of the AFM tip with the sample surface.

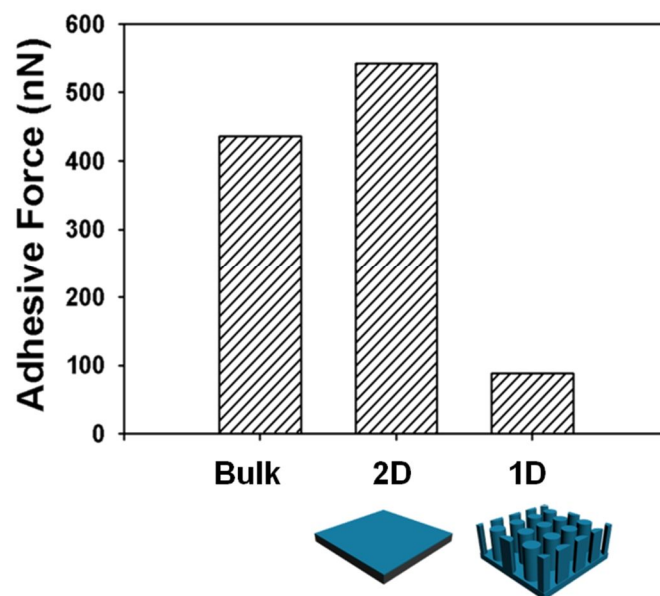


Figure 3.12. Adhesive forces on bulk PS, thin film, and one-dimensional PS nanorod arrays.

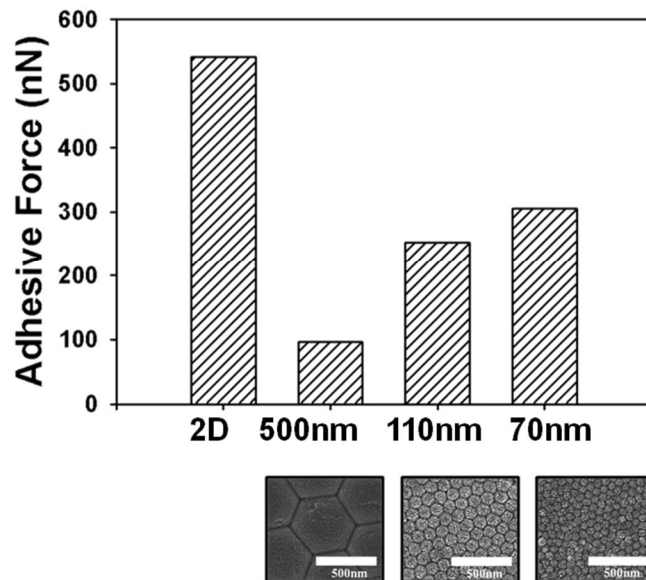


Figure 3.13. Adhesive properties and SEM images of convex surface replicated from the etched Al surface with wavelength variation.

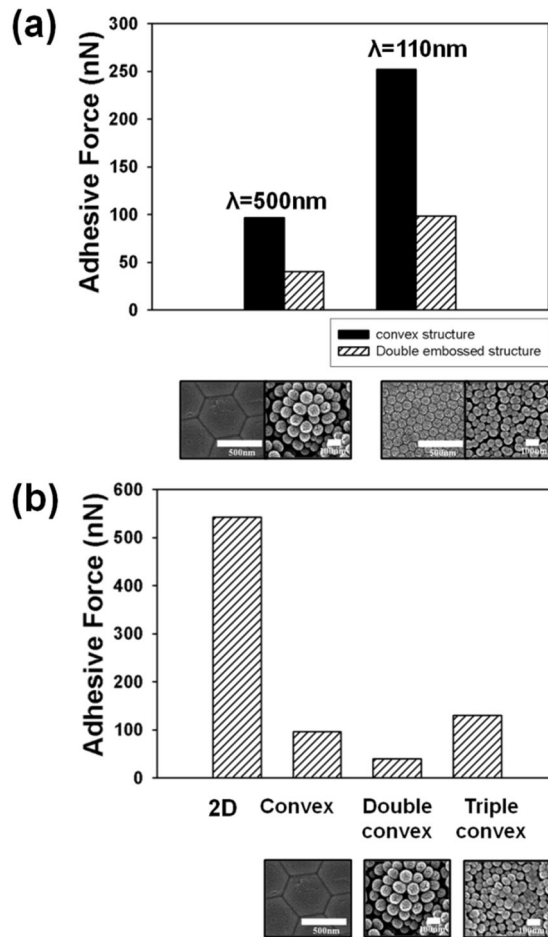


Figure 3.14. Structural complexity effect on adhesive force. Adhesive force on convex and double -embossed structures with 110 nm and 500 nm in wavelength (a), and convex, double-embossed, and triple-embossed nanostructures with 500 nm in wavelength (b). SEM images of each nanostructures are displayed under the graph.

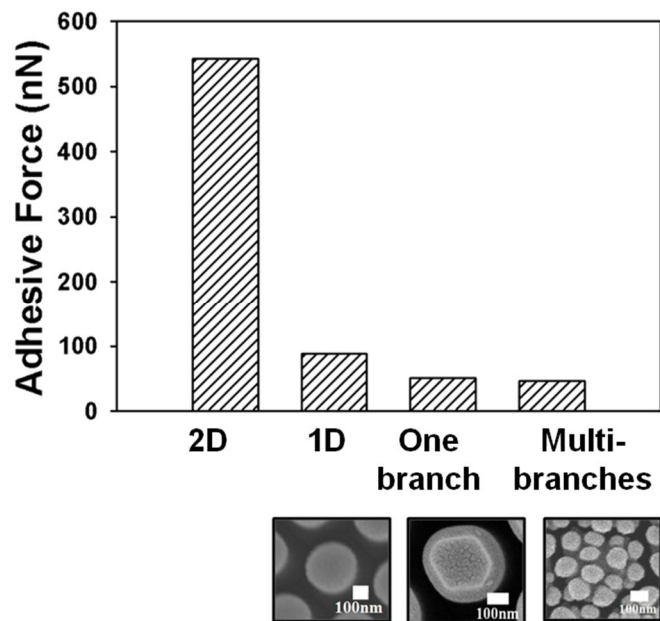


Figure 3.15. Adhesive properties and SEM images of branched structures based on one-dimensional nanostructures.

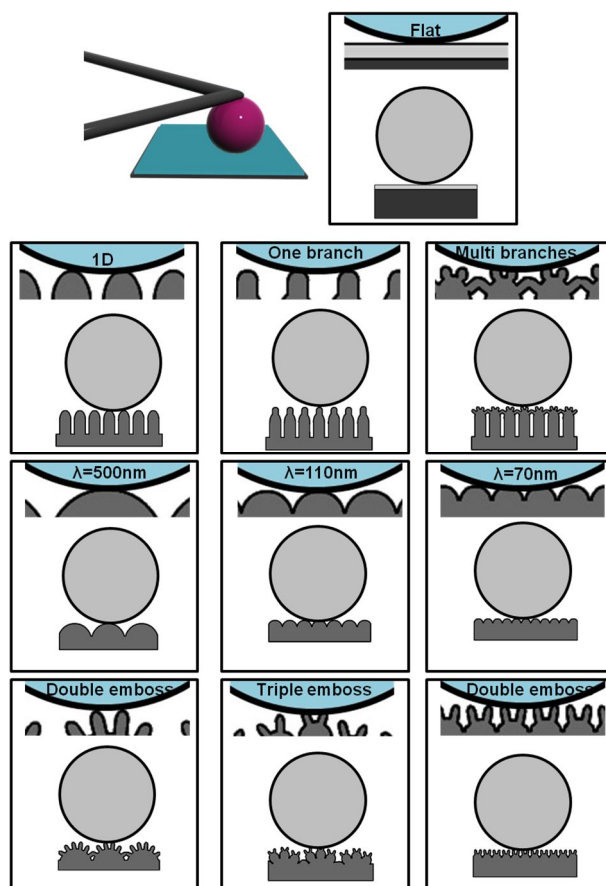


Figure 3.16. Schematic illustration of real contact area between the tip with Au-particle and nanostructured surfaces.

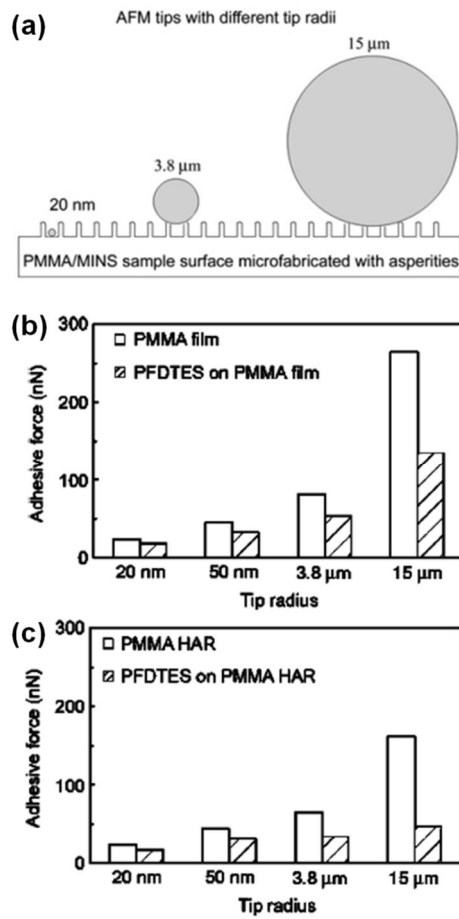


Figure 3.17. The relation between the adhesive force and the real contact area [38].

We adopted a different system based on anisotropic structures to obtain the enhanced adhesive properties because natural gecko setae exhibit the anisotropy of adhesion and friction during its attachment and detachment. Significant effort has been reported to fabricate angled gecko-inspired surface showing adhesion behaviors similar to those of gecko setae [39-42]. For example, Sitti's group has demonstrated the direction dependent adhesion behavior of angled fibers [39, 40]. Lee et al. fabricated angled polypropylene microfiber arrays with a gecko-inspired structure and they observed directional adhesion [41].

In this study, we proposed a simple method to fabricate the anisotropic polymer nanopillars by AAO template, and we investigated their adhesion behaviors. The schematic illustration of the experimental procedure to fabricate uniform asymmetric polymeric nanopillars is shown in Figure 3.18. After the fabrication of the high density nanopillar arrays (diameter~150 nm and length~1.5 μm), asymmetrically bent nanopillars were uniformly formed by gold (Au) evaporation. During Au evaporation, the nanopillars were bent toward the metal face because of a residual tensile stress (Figure 3.19 (a)). The morphology of asymmetrically bent (Janus) nanopillars was analyzed by SEM, as shown in Figure 3.19 (b). The Janus nanopillars in one direction have anisotropic shear adhesion property. In Figure 3.19 (c), the adhesion characteristics of the flat film, the one-dimensional nanopillars, and bent Janus nanopillars are compared. The dimensions of the bent Janus nanopillars were the same as that of the one-dimensional ones before the gold deposition. For the one-dimensional nanopillars, the shear adhesion force was measured as 4.12 N/cm^2 . On the other hand, the shear adhesion force of the bent Janus nanopillars was 6.45 N/cm^2 and 1.20 N/cm^2 , respectively, for the two opposite directions which are parallel and anti-parallel to the curved direction of

the nanopillars. Although the values of adhesive force obtained by bent Janus nanopillars are lower than previous results, it is meaningful that the nanopillars of anisotropic adhesion property can be fabricated by a simple template method.

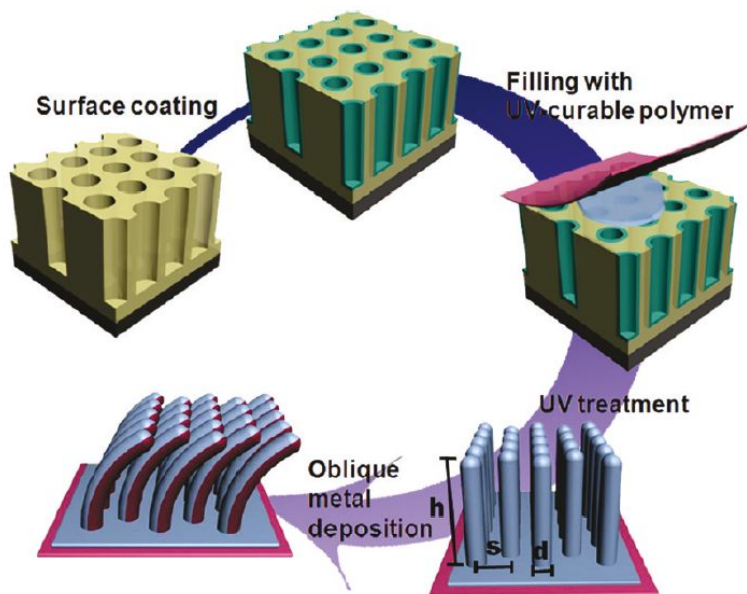


Figure 3.18. Schematic illustration of the experimental procedure to fabricate asymmetrically bent Janus nanopillar arrays prepared from reusable AAO templates.

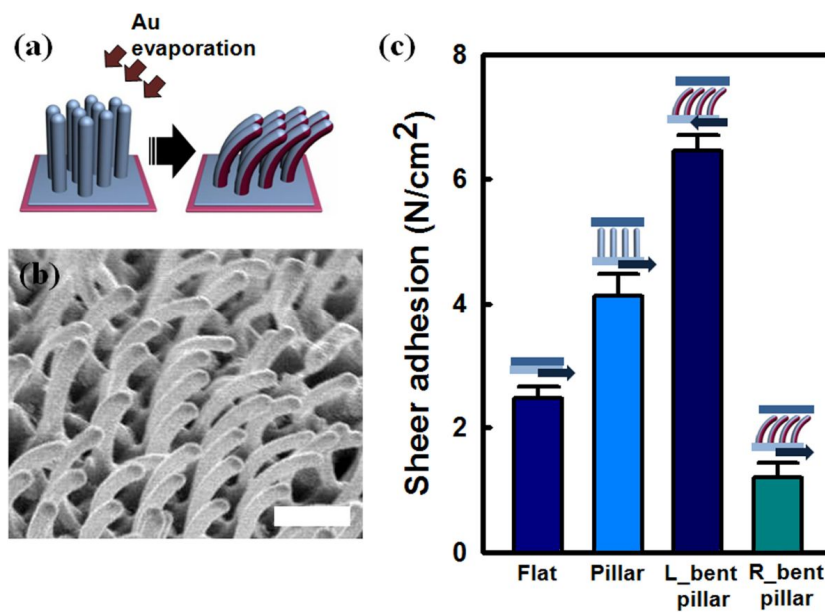


Figure 3.19. Asymmetrically bent Janus nanopillars and the shear adhesive properties of bent Janus nanopillars: A schematic illustration of the fabrication of bent Janus nanopillars by Au evaporation (a), SEM image of bent nanopillars prepared by 20 nm thick Au evaporation. Scale bar= 500 nm (b). The shear adhesion force of PUA nanopillar arrays (c).

3.4. Conclusion

In summary, we tried to fabricate nature-inspired nanostructures such as lotus leaf or gecko's foot surface to realize their superior properties. We presented diverse biomimetic polymeric nanostructures. The hierarchically structured nanopores in the AAO templates were obtained via anodization on highly ordered concave Al surfaces or in the cylindrical nanopores. Hierarchical nanostructured polymer surfaces were replicated from AAO templates.

Mimicking lotus leaf surface:

We analyzed surface wettability on hierarchically nanostructured surfaces. Hierarchical nanostructures formed on convex surfaces showed $\sim 40^\circ$ increase of water contact angle, as compared to a flat surface. Morphological diversity of these nanostructures did not vary the water contact angles. When the multiple nanobranches were placed on a long and large nanorod, the water contact angle was a bit increased (152°), and the surface wettability became close to water repellent plant leaf surfaces in nature. Although we could not fabricate more superhydrophobic surface like completely repellent plant leaves, the wettability of nanoscopically hierarchical structures could be studied. This current approach would be helpful in the manufacture of self cleaning surface or water repellent textiles.

Mimicking gecko' foot surface:

We firstly measured the adhesive force on hierarchical nanostructures by AFM.

With the increase of the structural complexity on polymeric surface, the adhesive force decrease because of the decrease of contact area between the tip with Au particle and the sample surface. However, as asymmetrically bent nanostructures were introduced on the surface, they showed the enhanced adhesive force and anisotropic adhesion characteristics.

3.5. References

- [1] B. Bhushan, Y. C. Jung, and K. Koch, *Phil. Trans. R. Soc. A* **2009**, 367, 1631.
- [2] B. Pokroy, S. H. Kang, L. Mahadevan, and J. Aizenberg, *Science* **2009**, 323, 237.
- [3] D. Sameoto and C. Menon, *J. Micromech. Microeng.* **2010**, 20, 115037.
- [4] K. Autumn, Y. A. Liang, S. T. Hsieh, W. Zesch, W. P. Chan, T. W. Kenny, R. Fearing, and R. J. Full, *Nature* **2000**, 405, 681.
- [5] K. Autumn, M. Sitti, Y. C. A. Liang, A. M. Peattie, W. R. Hansen, S. Sponberg, T. W. Kenny, R. Fearing, J. N. Israelachvili, and R. J. Full, *Proc. Natl. Acad. Sci. USA* **2002**, 99, 12252.
- [6] C. Neinhuis and W. Barthlott, *Ann. Bot.* **1997**, 79, 667.
- [7] W. Lee, M. K. Jin, W. C. Yoo, and J. K. Lee, *Langmuir* **2004**, 20, 7665.
- [8] K. Koch, B. Bhushan, Y. C. Jung, and W. Barthlott, *Soft Matter* **2009**, 5, 1386.
- [9] N. A. Patankar, *Langmuir* **2004**, 20, 8209.
- [10] V. Zorba, E. Stratakis, M. Barberoglou, E. Spanakis, P. Tzanetakis, S. H. Anastasiadis, and C. Fotakis, *Adv. Mater.* **2008**, 20, 4049.
- [11] W. K. Cho and I. S. Choi, *Adv. Funct. Mater.* **2008**, 18, 1089.
- [12] T. S. Kustandi, V. D. Samper, W. S. Ng, A. S. and Chong, H. Gao, *J. Micromech. Microeng.* **2007**, 17, N75.
- [13] M. P. Murphy, B. Aksak, and M. Sitti, *Small* **2009**, 5, 170.
- [14] A. Y. Y. Ho, L. P. Yeo, Y. C. Lam, and I. Rodriguez, *Acs Nano* **2011**, 5, 1897.
- [15] S. Wang and L. Jiang, *Adv. Mater.* **2007**, 19, 3423.
- [16] A. del Campo and C. Greiner, *J. Micromech. Microeng.* **2007**, 17, R81.

- [17] S. J. Choi, K. Y. Suh, and H. H. Lee, *J. Am. Chem. Soc.* **2008**, *130*, 6312.
- [18] S. J. Choi, K. Y. Suh, and H. H. Lee, *Nanotechnology* **2008**, *19*, 275305.
- [19] R. Di Mundo, F. Palumbo, and R. d'Agostino, *Langmuir* **2008**, *24*, 5044.
- [20] Y. Lee, K. Y. Ju, and J. K. Lee, *Langmuir* **2010**, *26*, 14103.
- [21] B. K. Lim, S. H. Lee, J. S. Park, and S. O. Kim, *Macromol. Res.* **2009**, *17*, 666.
- [22] J. S. Park, S. H. Lee, T. H. Han, and S. O. Kim, *Adv. Funct. Mater.* **2007**, *17*, 2315.
- [23] H. M. Bok, S. Kim, S. H. Yoo, S. K. Kim, and S. Park, *Langmuir* **2008**, *24*, 4168.
- [24] J. T. Chen, D. Chen, and T. P. Russell, *Langmuir* **2009**, *25*, 4331.
- [25] M. K. Choi, H. Yoon, K. Lee, and K. Shin, *Langmuir* **2011**, *27*, 2132.
- [26] Y. W. Lee, S. H. Park, K. B. Kim, and J. K. Lee, *Adv. Mater.* **2007**, *19*, 2330.
- [27] L. Zhang, Z. L. Zhou, B. Cheng, J. M. DeSimone, and E. T. Samulski, *Langmuir* **2006**, *22*, 8576.
- [28] H. Masuda and K. Fukuda, *Science* **1995**, *268*, 1466.
- [29] J. L. Zhang and Y. C. Han, *Langmuir* **2008**, *24*, 796.
- [30] G. W. Meng, Y. J. Jung, A. Y. Cao, R. Vajtai, and P. M. Ajayan, *Proc. Natl. Acad. Sci. USA.* **2005**, *102*, 7074.
- [31] A. Y. Y. Ho, H. Gao, Y. C. Lam, and I. Rodriguez, *Adv. Funct. Mater.* **2008**, *18*, 2057.
- [32] M. Kim, K. Kim, N. Y. Lee, K. Shin, and Y. S. Kim, *Chem. Commun.* **2007**, *22*, 2237.
- [33] K. Kim, M. J. Lee, C. Kim, E. Woo, M. Kim, Y. S. Kim, and K. Shin, *Sol. State. Phenom.* **2007**, *124-126*, 1269.
- [34] M. Park, G. Yu, and K. Shin, *J. Cryst. Growth.* **2011**, *326*, 28.

- [35] S. R. Quake and A. Scherer, *Science* **2000**, *290*, 1536.
- [36] J. P. Rolland, R. M. Van Dam, D. A. Schorzman, S. R. Quake, and J. M. DeSimone, *J. Am. Chem. Soc.* **2004**, *126*, 2322.
- [37] Y. Tian, N. Pesika, H. Zeng, K. Rosenberg, B. Zhao, P. McGuiggan, K. Autumn, J. Israelachvili, *Proc. Natl. Acad. Sci. USA* **2007**, *103*, 19320.
- [38] Z. Burton, B. Bhushan, *Nano Lett.* **2005**, *5*, 1607.
- [39] B. Aksak, M. P. Murphy, M. Sitti, *Langmuir* **2007**, *23*, 3322.
- [40] M. P. Murphy, B. Aksak, M. Sitti, *J. Adhesion Sci. Technol.* **2007**, *21*, 1281.
- [41] J. Lee, R. S. Fearing, K. Komvopoulos, *Appl. Phys. Lett.* **2008**, *93*, 191910.
- [42] M. P. Murphy, B. Aksak, M. Sitti, *Small* **2009**, *5*, 170.

Chapter 4.

Introduction

: Practical Applications of Patterned Surface

4.1. TFT-LCD Displays [1]

As an active matrix displays, the technologies of thin film transistor liquid crystal display (TFT-LCD) were developed from the early 80s. Application of active matrix devices such as thin film transistor (TFT) devices has provided to the availability of LCD with high resolution. The basic structure of TFT-LCD is shown in Figure 4.1. In general, LCD device consists of a nematic liquid crystal sandwiched between two glass plates. In detail, the glass sheet is coated with a transparent conducting metal oxide film which acts as an electrode. This electrode surface can be patterned to make the rows and columns of a passive matrix display or the individual pixels of an active matrix display. These electrodes are employed to apply the voltage across the LC cell, which is essential to induce the LC orientation. Then, a polymer alignment layer is introduced onto these electrodes. Rubbing process was performed onto this polymer surface to form periodic roughness such as microscopic grooves in the film. Surface topography helps align the LC molecules in a preferred direction. The alignment mechanism by micrograting will be given a detailed account in chapter 4.2.2. Two transparent electrodes with the alignment layer are separated by the spacer, and then LC molecules are inserted between the two electrodes. When an electric field is applied between the two electrodes, LC molecules will orient to control light passage. TFT-LCDs are used in television, computer monitor, mobile phones, video game systems, navigation systems, projectors, etc.

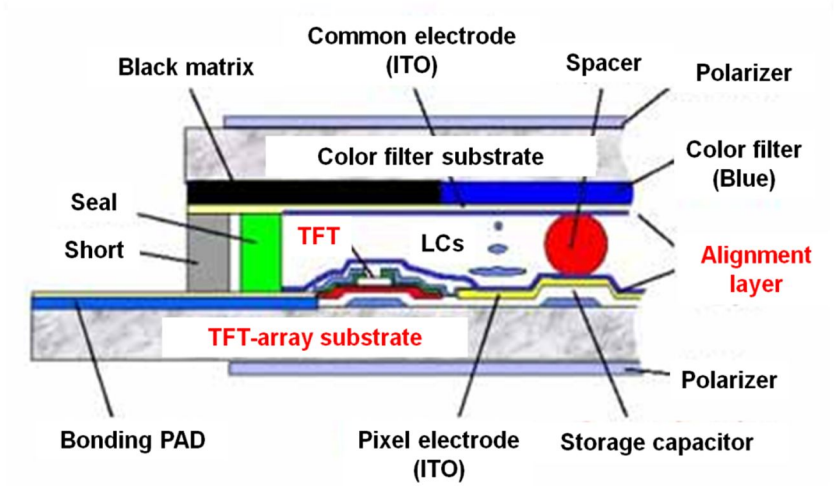


Figure 4.1. Basic structure of TFT-LCD devices. This schematic diagram comes from the address of web site: www.plasma.com.

4.2. Liquid Crystal Alignment

4.2.1. Liquid Crystal Alignment Methods [1]

In LCD devices, LC molecules are usually sandwiched between two transparent electrodes coated polymer alignment layer with a gap of 1-10 μm . Here, LC molecular orientations are governed by the influence of the rubbed polymer alignment surface. Typical orientations of LC molecules are shown in Figure 4.2.

These orientations are classified into two groups by the direction of the directors. Firstly, the directors of the LC molecules in the homogeneous, tilted and homeotropic cases are aligned in one fixed (preferred) direction. On the other hand, the director of the LC molecules in the splay, twist, bend, and hybrid cases are not fixed in one direction. In this orientation, the LC molecules undergo elastic deformation by the stress.

Homogeneous alignment:

When the LC molecules align parallel to the substrates, it is called “homogeneous alignment”. Commonly, the tilted alignment with low pretilt angle (less than $\sim 10^\circ$) is called homogeneous. In order to obtain homogeneous alignment, rubbed polyimide films are usually used as the alignment layer. Non-rubbing methods such as photoalignment and micrograting have been developed.

Tilted alignment:

Tilted alignment is an intermediated state between homogeneous and homeotropic, and the molecules are tilted at certain pretilt angle.

Homeotropic alignment:

When the LC molecules align perpendicular to the substrates, it is called “homeotropic alignment”. Homeotropic alignment can be acquired by the alignment layer coated with hydrophobic films such as silane compounds.

We summarized common LC alignment methods in Figure 4.3. From the early stage of LCD production, only the rubbing method has been employed for alignment technologies in LCD industry. Because the mechanical rubbing method is a simple, convenient, and low-cost, it is considered that the rubbing method cannot be replaced by any other method to realize a better alignment performance. However, the generation of defects or impurities in the rubbing method was issued since the TFT-LCDs production. In the rubbing method, the polyimide surface is rubbed by directly contacting with a cloth. From contact process, the TFT devices can be destroyed by the electrostatic charge caused by the friction between the polyimide surface and the cloth surface. Also, the devices can be polluted by surface defects or impurities, which are generated during mechanical rubbing. Especially, these problems led to quite lower reliability of the device performance in TFT device production. In addition, the mechanism of the LC alignment by mechanical rubbing is not clearly understood.

In view of the problems mentioned above, it may be necessary for studies on the development of other methods LC alignment besides the mechanism of the rubbing process. Thus, novel alignment technologies are required that not only overcome the disadvantages of contact method, but also increase in production yield. Methods using UV light radiation on photocurable polymer surfaces or

microscopic gratings (microgratings) have been suggested. In this section, we introduce three popular alignment technologies in detail: rubbing, photoalignment, and micrograting.

Rubbing:

Mechanical rubbing process in the manufacture of LCDs is to rub a polyimide substrate using a rotating drum which is covered by a cloth with microfibers. A typical rubbing machine consisting of a rotating drum and a substrate holding platform is shown in Figure 4.4 (a). Even though this process has some problems, for example the generation of electrostatic charge and surface impurities, rubbing is still effective alignment process because it is a simple and easy method to align LC molecules. Moreover it can be applied to a large area at low cost. In rubbing process, there are two alignment mechanisms: a short range interaction by the reorientation of the polymer chains and a long range interaction caused by the elastic energy induced by surface topography. The surface rearrangement of the rubbed polymer chains can strongly affects on the mechanism of LC alignment, as shown in Figure 4.4 (b). However, the alignment strength of LC molecules is dependent on surface structure caused by rubbing process with the cloths. Therefore, the surface grating may play an important role in the alignment of the LC. In spite of many efforts to demonstrate the mechanism of LC alignment by mechanical rubbing process, however, it is still not obvious how the surface reorientation of the polymer chain on alignment layer by rubbing the cloth occurs.

Photoalignment:

Photoalignment has been introduced as a promising noncontact alignment method

to overcome the problems of the contact method. It involves the reversible transition in the molecular shape by the the polarization direction of the absorption of light (Figure 4.5). For example, in a system of a nematic LC containing an azobenzene, the photoinduced alignment includes the destruction of the mesophases by the strong change in the molecular shape of the photoisomerized azobenzene units. The generation of anisotropy by using polarized light is called the Weigert effect. The mechanism of photoinduced alignment in some materials, however, is not yet understood because the photochemical reactions are different on the basis of each photoalignment material.

Micrograting:

Microscopic grating itself can cause LC molecules to align in the direction parallel to the groove structure on alignment layer surface (Figure 4.6). Several processes to fabricate the surface with microgroove structures for the LC alignment have been proposed. For example, the photolithographic technique using photoreactive polymers with light exposure and reactive etching on the SiO₂ surface has been used to fabricate microgrooves as a master mold. Polymer alignment layer with microgrooves have been replicated from this master mold. Microgroove surfaces with a pitch smaller than 1 μm can realize the better alignment behavior than that of any other alignment method. Therefore, this polymeric microgroove surface could be an effective method for the LC alignment.

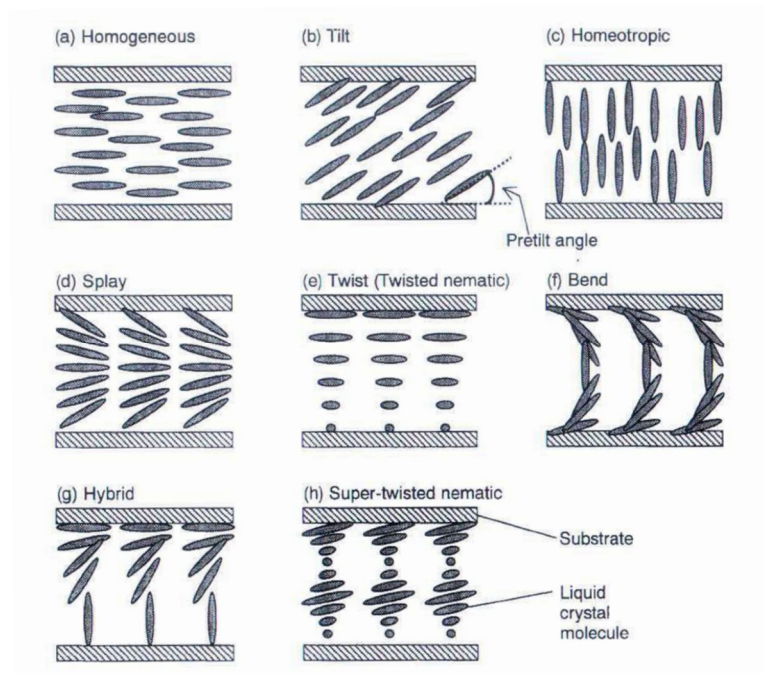


Figure 4.2. Typical orientations of nematic LCs [1].

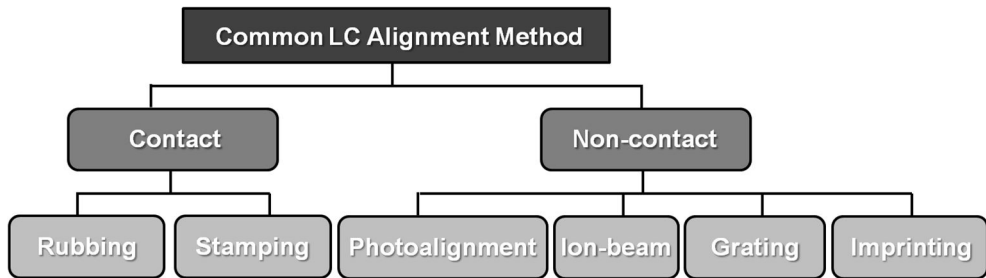


Figure 4.3. Common LC alignment methods: contact and non-contact method.

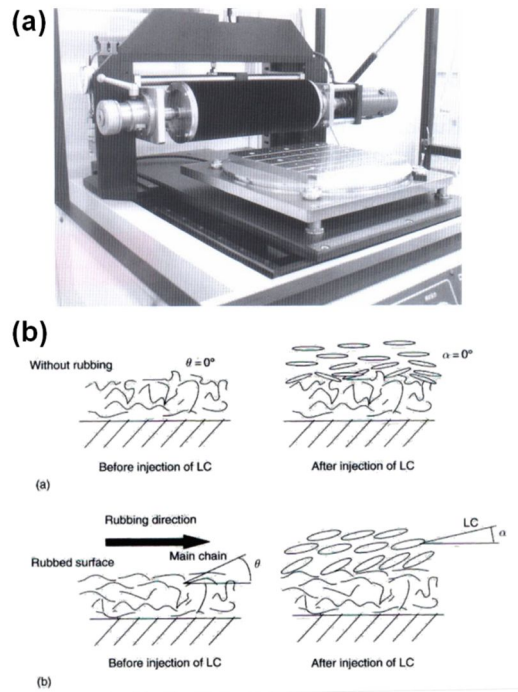


Figure 4.4. Contact alignment method: mechanical rubbing [1].

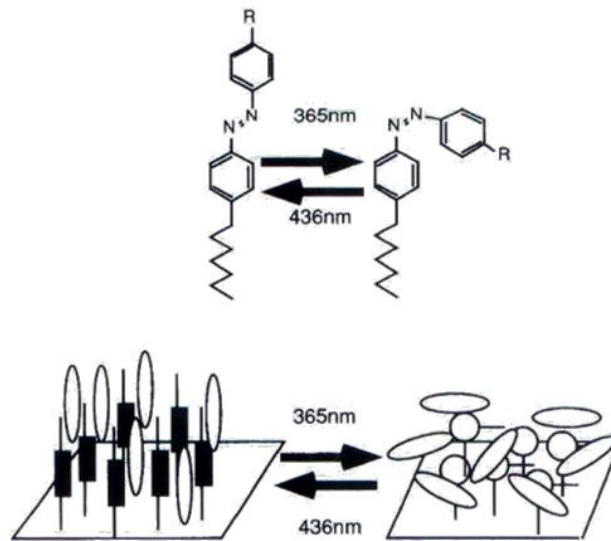


Figure 4.5. Non-contact alignment method (1): photoalignment [1].

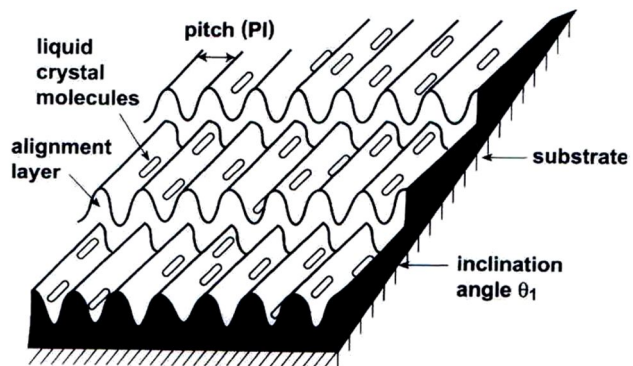


Figure 4.6. Non-contact alignment method (2): Micrograting [1].

4.2.2. The Mechanism of Liquid Crystal Alignment [2-7]

The LC molecules near the alignment layer surface affect the liquid crystal orientation in the bulk (the intermediation region of a LC cell) by molecular-molecular interactions. Mostly, there is a strong interaction between the alignment layer surface and the LC molecules near the surface. Such a relationship at the LC/substrate interface is called “surface anchoring”. In the case of the strong anchoring, the alignment of the LCs is hardly changed by applying external fields such as the electric or magnetic fields. Then, the LC orientation recovers to the initial states after the removal of external fields. On the other hand, for the weak anchoring, the LC orientation after removing the field is different from the initial orientation. The surface anchoring energy is defined as by Rapini-Papoular form:

$$f_A = \left(\frac{\omega}{2}\right) \sin^2(\emptyset - \theta),$$

where ω , \emptyset , and θ represent the anchoring strength, the preferred anchoring angle of easy axis, and the actual angle of director, respectively.

The reason for the LC alignment can be explained by two special interactions between the LC molecules and the alignment layer surface: a polar and non-polar interaction. In general, a polar interaction will prefer to align LC molecules with polar end group perpendicular to the substrate, and this molecular interaction (van der Waals interactions) will lead to uniformly ordered alignment. However, the non-polar interaction in general does not induce uniform alignment of LC molecules due to the absence of strong molecular interaction at LC/substrate interface.

A different but interesting study on the mechanism of LC alignment has been

done by Berreman. Berreman suggested “elastic-energy mechanism”, which is based on the LC alignment induced by surface geometry. When the geometrical factor (roughness or topography) is introduced to the surface, an additional elastic energy can occur due to the distortion of LC molecules along the surface groove. Thus, the directors of LC molecules are parallel to the surface grooves in order to minimize the elastic energy. If the directors are not paralleled to the grooves, the elastic deformation of LC molecules can occur adjacent to the surface where the directors of LC molecules change to parallel orientation. When the microgrooved patterns exist on the surface, the alignment of LC molecules can be described using the theory of Oseen-Frank elastic energy. The Frank elastic energy is given as

$$f = \frac{1}{2} \{K_{11}(\nabla \cdot n)^2 + K_{22}[n(\nabla \cdot n)]^2 + K_{33}[n \times (\nabla \times n)]^2\},$$

where K_{11} , K_{22} , and K_{33} are the splay, twist, and bend elastic coefficient, respectively.

If the microgrooved pattern has larger space between lines ($> 10\mu\text{m}$), the alignment of LC molecules can be determined by the surface (or side) effect of the pattern, and the director of LCs can be tilted. On the other hand, if the gap of microgrooved pattern gets smaller ($< 2\mu\text{m}$), the LCs prefer to distort along the side walls of the pattern because the space between the lines are not sufficient. It can be explained that the alignment of LCs on microscopically smaller patterns is dominated by the elastic deformation of LCs on surface topography. Furthermore, when the LCs are confined by nanoscopic geometry, they can suffer stronger packing frustration than microscopic confinement. Thus, the rearrangement of LC packing can be generated as the space is nanoscopically narrower and deeper because of the increase of the Frank elastic energy density.

In conclusion, there are two contributions affecting on the LC alignment on the

rubbed surfaces. One is the influence of short-range molecular forces between the LC molecule and the substrate surface based on the strength of surface anchoring. The other is a thoroughly geometrical effect that can generate the elastic deformation on grooved surface. The nematic director is parallel to the grooves in order to reduce the additional elastic energy. The equilibrium orientation of the nematic LC molecules near a grooved surface is probably determined by the geometrical factor.

4.3. Organic Thin Film Transistors

4.3.1. Organic Thin Film Transistors (OTFTs) [8-11]

Organic thin film transistors (OTFTs) were firstly identified as an electronic device in 1987. In principle, organic semiconductors are applicable for the field-effect transistors due to intrinsically low density of dangling bond on the surface of organic semiconductors. However, they have been not suitable for the thin film transistor owing to inherent poor electric properties of organic semiconductors. Unlike the inorganic electric devices, organic materials are strongly dependent on imperfections of film structures and insufficient purities. Thus, there were few interests in the OTFTs because of the poor electric performance. Many researchers have focused on improving the charge-carrier mobility since the first description of the OTFTs. Organic single-crystal field-effect transistors were suggested to enhance the electrical properties because it is similar to single-crystal structure of inorganic semiconductors. The availability of organic single-crystal semiconductor devices can open new low-cost microelectronics such as active matrix displays or sensors. However, it still remains a challenge in fundamental charge transport studies because of the difficulties of the fabrication techniques.

4.3.2. Thin-Film Transistor Architecture [8, 9]

A thin film transistor (TFT) generally consists of three parts: an insulator, a thin semiconducting layer, and three electrodes. Two of the electrodes, the source and drain, are in directly ohmic contact with the semiconductor; the third, the gate, is separated from the semiconductor by the insulator. The basic fabrication process consists of piling up thin films of the different elements. Because most organic semiconductors are unstable materials, the deposition of organic semiconductors on the insulator is much easier than the opposite structure. Thus, the large majority of current OTFTs are built according to the bottom-gate architecture. The TFT device based on bottom-gate structure can be classified in common two configurations: the bottom contact (BC) devices and the top contact (TC) device, as shown in Figure 4.7 (a) and (b), respectively. For the BC structure, the source and drain electrodes are placed on the insulator (gate dielectric) layer and organic semiconductors are coated on these two electrodes. So, it is possible to pattern the electrodes by means of microlithographic techniques. On the other hand, for the TC structure, the organic semiconductors lie between the insulator and the source and drain electrodes. This configuration provides higher device performance because of lower contact resistance and improved organic film formation on the impurity-free dielectric surface.

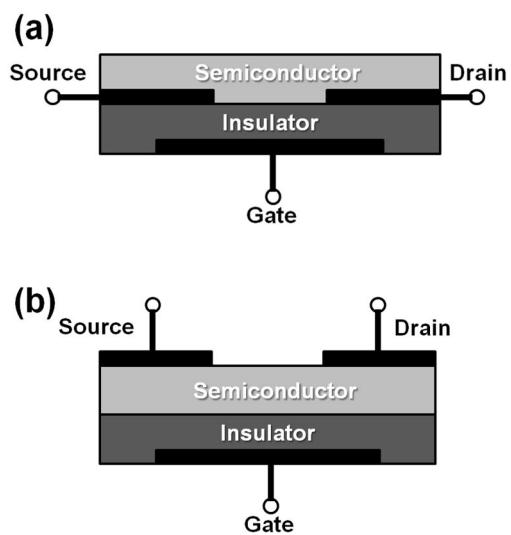


Figure 4.7. Architecture of OTFTs based on bottom-gate structure. Bottom contact (BC) device (a) and top contact (TC) device (b).

4.3.3. Operating Mode [8, 10]

In the p-type transistor with TC devices, when a positive voltage is applied to the gate, charge carriers are not induced at the insulator/semiconductor interface, and it is called “depletion region”. However, when a negative voltage is applied to the gate, an equal but opposite sign charge is induced and accumulated at the insulator/semiconductor interface, it called “accumulation region”. On the organic semiconductor layer, this charge forms a conducting channel, and it can be “on state”. Figure 4.8 shows typical output and transfer curves of the OTFTs. Because the conducting channel is proportional to the charge carrier, it is also proportional to the gate voltage. At low drain voltage, the current follows Ohm’s law, as shown in Figure 4.8 (a). Therefore, it is proportional to both the gate and drain voltages and this regime is called the linear regime. As the drain voltage increases, the current is steadily increased until pinch-off of the channel. At this point, the channel current becomes independent of the drain bias. This regime is called “saturation regime”. The curve in Figure 4.8 (b) is the transfer characteristic, which shows that the device performance such as electron/hole mobility, on/off ratio, and threshold volate.

4.3.4. OTFTs Parameters [11]

Field-effect mobility (μ):

Field-effect mobility represents the drift velocity of the charge carrier (cm/s) per unit applied field (V/cm), leading to the units for mobility of cm^2/Vs . It is relationship between the charge carrier speed in a material and the strength applied by electric field. The operation of the transistor is divided into two regimes in the output curve; linear and saturation regimes. Each value of the drain current is calculated as follows,

$$\text{Linear regime: } I_d = \frac{W\mu C_i}{L} (V_g - V_t - \frac{V_d}{2}) V_d$$

$$\text{Saturation regime: } I_d = \frac{W\mu C_i}{L} (V_g - V_t)^2$$

where I_d is the drain current, μ is the field-effect mobility of the organic semiconductor, W is the channel length, C_i is the capacitance per unit area of the dielectric layer, V_t is the threshold voltage, V_d is the drain, and V_g is the gate voltage. A linear regime is observed at low voltage, whereas a saturation regime indicates when the drain voltage exceeds the gate voltage. The value of the mobility is extracted from the slope of $I_d^{1/2}$ - V_g curve (transfer curve).

On/Off current ratio ($I_{on/off}$):

The on/off current ratio indicates the difference in source/drain current in the “on state” and “off state. Here, when the transistor is turned on ($V_g \neq 0$, “on state”) and when the transistor is turned off ($V_g = 0$, “off state”). This on/off ratio represents the

ability of the transistor to shut down. It is calculated from the $\log I_d - V_g$ curve.

Threshold voltage (V_t):

Threshold voltage (V_t) is the voltage at which the transistor turns from the “off” to the “on” state. It indicates the quality of the interface between the organic semiconductor and the gate insulator. The threshold voltage is determined by the extrapolation of the linear region of $I_d^{1/2} - V_g$ to the intercept on the V_g .

Subthreshold slope:

The subthreshold slope is the inverse slope of the $I_d - V_g$ measured below threshold.

It typically means the change in the gate voltage required to change the drain current by a factor of 10, leading to the 10 logarithmic units of mV/decade.

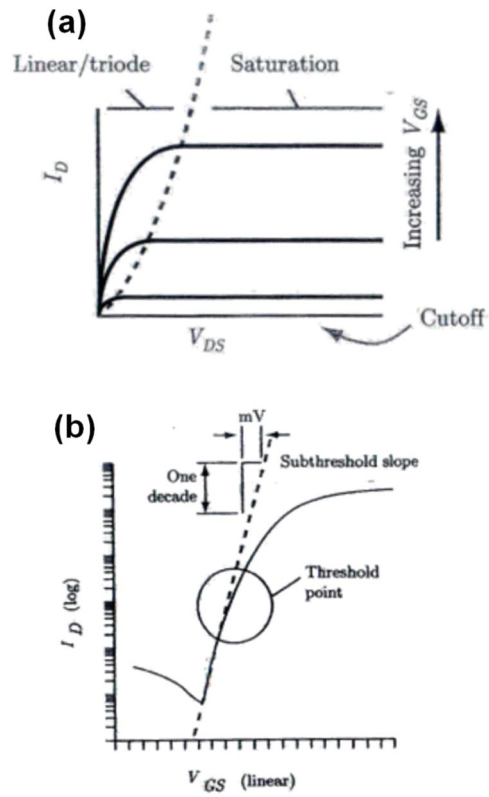


Figure 4.8. The typical output curves (a) and transfer curves (b) of OTFTs [11].

4.4. References

- [1] K. Takatoh, M. Hasegawa, M. Koden, N. Itoh, R. Hasegawa, M. Sakamoto, Eds., *Alingment technologies and applications of liquid crystal devices*, Taylor & Francis, London and New York **2005**.
- [2] D. W. Berreman, *Phys. Rev. Lett.* **1972**, *28*, 1683.
- [3] D. W. Berreman, *Mol. Cryst. Liq. Cryst.* **1973**, *23*, 215.
- [4] U. Wolffa, W. Greubela, H. KrÜGera, *Mol. Cryst. Liq. Cryst.* **1973**, *23*, 187.
- [5] Y. Kawata, K. Takatoh, M. Hasegawa, M. Sakamoto, *Liq. Cryst.* **1994**, *16*, 1027.
- [6] Y. Yi, G. Lombardo, N. Ashby, R. Barberi, J. E. Maclennan, N. A. Clark, *Phys. Rev. E.* **2009**, *79*, 041701.
- [7] K. Lee, H. Kang, J.-C. Lee, D. Kang, K. Shin, *Liq. Cryst.* **2011**, *38*, 1131.
- [8] H. Klauk, Ed, *Organic electronics; materials, manufacturing and applications*, WILEY-VCH Verlag GmbH & Co. KGaA.
- [9] G. Horowitz, *Adv. Mater.* **1998**, *10*, 365.
- [10] R. W. I. de Boer, M. E. Gershenson, A. F. Morpurgo, V. Podzorov, *Phys. Stat. Sol. (a)* **2004**, *201*, 1302.
- [11] I. Kymissis, Ed. *Organic field effect transistors: theory, fabrication and characterization*, Springer.

Chapter 5.

Nanoconfinement effect on LC alignment*

*This chapter is based in part on a paper from Kyunghee Lee, Hyo Kang, Jong-Chan Lee, Daeseung Kang and Kyusoon Shin, *Liquid Crystals* **2011**, 38, 1131-1136. Copyright (2011) Taylor & Francis.

5.1. Introduction

Control of molecular packing under nanoscopic confinement that would determine the property of the molecular assembly is getting more and more important nowadays due to performance improvement of miniaturized devices as well as understanding on the fundamental nature of molecular self-assembly [1-7]. Molecular packing should be perturbed especially under nanoscopic geometrical constraint, because the hyperstructural self-assembly of small organic molecules are usually on nanoscale [3, 5]. Liquid crystal (LC) molecules are one of the representative molecules in the current display industry, and the precise control of molecular alignment has been key issues in the LC researches [8-10]. Several innovative approaches were demonstrated in recent years on the control of LC alignment by employing surface patterning with nanoscale or microscale structures [11-15]. Lazarouk *et al.* obtained a vertical (homeotropic) orientation of LC molecules on nanoscopic irregular random structures [12]. Their method would provide anisotropic elastic interactions between the LC molecules and surface structures and assist the packing of LC molecules [16, 17]. As an aligning method, usage of surface microscopic patterning has advantages over conventional methods, such as the strong directivity of LC alignment and durability due to the inherent thermodynamic stability of the alignment of LC molecules [18]. On a submicrometer-scale pattern, much larger than typical packing dimension of LC molecules, the shift of LC alignment occurs with the variation of pattern size [19-22]. However, when small organic molecules are confined by especially nanoscopic geometry, they would suffer stronger packing frustration than by

micrometer- or submicrometer-scale confinement. If the feature of the geometry is very uniform and regular, in addition to the nanoscopic confinement, it is expected that even only a slight change of nanostructure dimension would influence the orientation of the small molecules very significantly. In order to find the effect of molecular confinement, it is prerequisite to examine the molecular structure and orientation on uniform regular surface patterns with nanoscopic dimensions that would be comparable to the scale of molecular packing. In this study, we manufactured highly-ordered nanorod arrays as an alignment layer, and investigated the orientation of LC molecules on the nanostructured layer. The effect of the nanostructure size on the LC alignment was also investigated in order to vary the degree of confinement imposed on the LC molecules. We believe that understanding the orientation of LC molecules on the nanoscopic features would be helpful to extend the knowledge to other small molecules and that this fundamental feature can reach to the application of practical industry.

5.2. Experimental Section

Schematic illustration of the experimental procedures is given in Figure 5.1. The details are as follows:

Fabrication of LC cell with microscopic and nanoscopic line patterns:

We fabricated a master mold on a silicon wafer using high-resolution photolithography. Then, polyurethane acrylate (PUA) was dropped on a very thin antiadhesion (PDMS) layer coated Si mold, and covered with a flexible polyethylene terephthalate (PET) film. After UV curing ($\lambda \sim 365$ nm) for 4hr, the PUA line patterns are obtained by simply peeling-off. Using PUA micro/nanopattern films, approximately 1.5 cm x 1.5 cm in size, the LC cells were assembled with spacers of 4.5 μm diameter. A nematic LC, 5CB (4-Cyano-4'-pentylbiphenyl) (Merck Co.), was infiltrated into the LC cell via capillary action. The LC cell was warmed above isotropic temperature (~ 40 °C) to erase the ordered phase, and then cooled to the room temperature.

Fabrication of PS film replicated from the AAO mold:

A nanoporous anodic aluminum oxide (AAO) membrane was produced using a conventional two-step anodization method, as described elsewhere [23]. A high purity Al sheet (99.999% thickness ~ 0.5 mm, Goodfellow) was electropolished in a mixture of perchloric acid and ethanol (HClO_4 : $\text{C}_2\text{H}_5\text{OH}$ =1:4 in volumetric ratio) and anodized in a 0.3 M oxalic acid solution for 12 hrs. After the first anodization, the alumina layer was selectively etched away from the aluminum sheet in a

mixture of chromic acid and phosphoric acid solution at 65 °C, and then the second anodization was performed for 50 ~ 130 s to fabricate the AAO with various pore lengths under the same conditions as the first anodization. The diameter of the nanopores was controlled by dipping the AAO membrane in a 0.1M phosphoric acid solution at 30 °C for 20 ~ 60 min. The home-made nanoporous membrane was filled with a polystyrene melt (M.W. ~ 280K, Aldrich) at 180 °C under vacuum. The polystyrene (PS) nanorod arrays were obtained after the remaining Al and alumina layers were dissolved in a cupric chloride solution and sodium hydroxide solution, respectively.

The LC cell assembly:

Using nanostructured PS films, approximately 1.5 cm x 1.5 cm in size, the LC cells were assembled with spacers of 4.5 μm diameter. A nematic LC, MLC-7026-000 (Merck Co., $\Delta\epsilon < 0$), was infiltrated into the LC cell via capillary action at room temperature.

Characterization:

The PS nanorod arrays were observed by field emission scanning electron microscopy (FE-SEM) (Carl Zeiss, SUPRA 55VP), and the LC orientation was analyzed by polarized optical microscopy (POM) (Nikon, ECLIPSE E600 POL) equipped with polarizers and digital camera (Nikon, COOLPIX995). The static contact angles of distilled water and MI (methylene iodide) on the flat bulk film and nanostructured PS film were measured using a Kruss DSA10 contact angle analyzer.

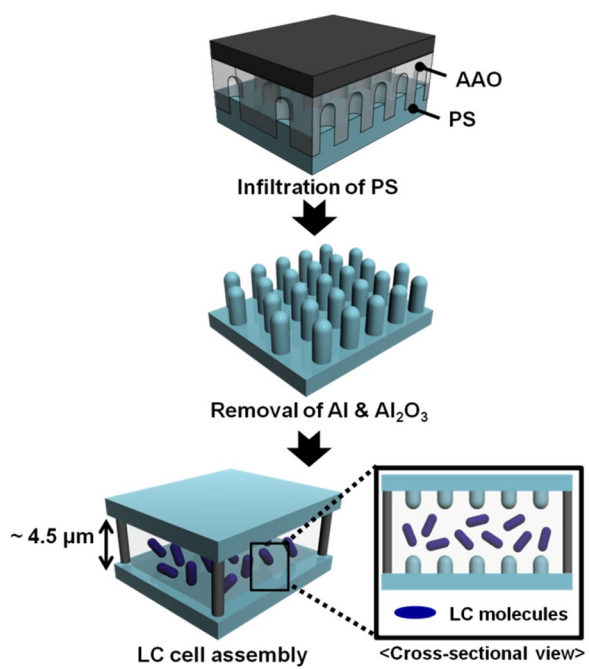


Figure 5.1. Schematic diagrams of LC Cells with nanostructured PS alignment layer.

5.3. Results and Discussion

5.3.1. The Effect of Surface Pattern Size on LC Alignment: Microstructure vs. Nanostructure

As the dimension of pattern decreases, it can be conjectured that the confinement would render higher degree of molecular confinement and orientation (Figure 5.2) [18]. The surface alignment of the LC molecules on grating surface was suggested by Berreman [16]. When the physical topography is introduced to the surface, the elastic energy mechanism is dominant because the surface topography directly affects the surface order parameter [16, 17]. To examine the effect of the degree of spatial confinement on LC alignment, we fabricated micropattern and nanograting replicated from Si master mold. This physical alignment technique using a periodic structure is sufficiently effective to manufacture reproducible and uniform alignment of nematic LC molecules [18]. Figure 5.3 displays the SEM and POM images of line pattern. The pattern width was 300 nm, 670 nm, 2.7 μm , 3.6 μm , and 5.1 μm from the left to right direction. We observed the transition of LC alignment to vertical alignment between 300 nm and 670 nm in the width of the line pattern. The order parameter in a larger pattern width (> 300 nm) is low due to a weak confinement, and it indicates that the LC molecules can align randomly in a given space. On the other hand, the LC molecules on nanograting of 300 nm are oriented vertically along the nanograting because of stronger confinement effect. It means that the elastic deformation of LC molecules in this narrow space can be generated due to spatial restriction, and it leads to the alignment transition from random to vertical orientation.

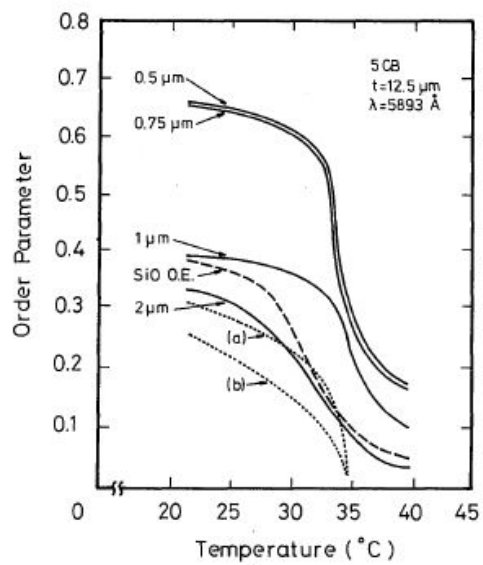


Figure 5.2. Order parameter of LC alignment with the variation of pattern size [18].

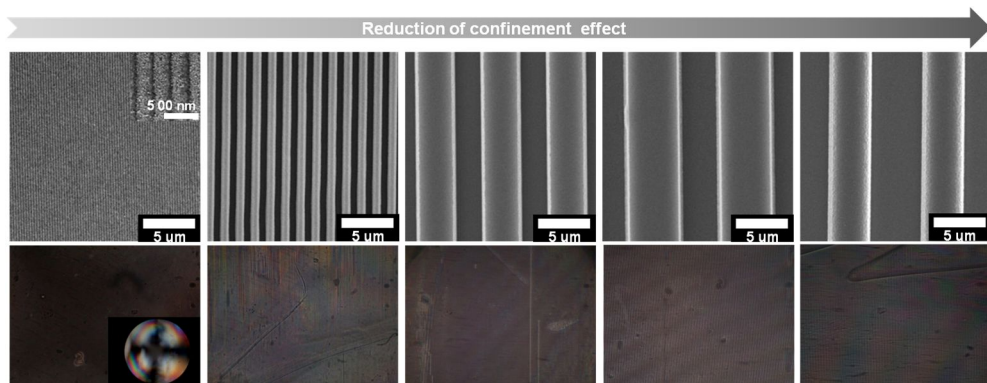


Figure 5.3. SEM (top) and POM (bottom) images of line patterns with the variation of pattern widths ranging from 300 nm to 5.1 μm.

5.3.2. The Influence of Nanoconfinement on LC Alignment

Schematic route to fabricate the LC cells is shown in Figure 5.3. The orientation of the rod-shaped LC on the PS nanorod arrays of different diameters with a fixed length, as shown in Figure 5.4. The diameters of each nanoporous AAO template were approximately 38 nm (D_1), 45 nm (D_2), 55 nm (D_3), 69 nm (D_4), 79 nm (D_5), and 83 nm (D_6) from top to bottom and the length of the rods of all films was estimated to be 142 ± 9 nm, as shown in the SEM images in the first and second columns in Figure 5.4, respectively. The nanoscopic structures were highly replicated to PS films from the AAO templates (the third column of Figure 5.3). The LC alignment on the nanorod arrays was analyzed using the POM, as shown in the fourth column in Figure 5.4. For $D_p \sim 38$ nm (D_1) and $D_p \sim 45$ nm (D_2), LC molecules showed both random planar and tilted orientation. A Maltese cross in the conoscopic POM image was found, although not distinctive, in $D_p \sim 55$ nm (D_3). This means that some LC molecules were oriented vertically to the PS substrates in the LC cell, as the diameter of nanorods became larger than a critical value. When D_p ranged from 69 nm (D_4) to 86 nm (D_6), the Maltese cross patterns became more noticeable in the conoscopic POM. The distinctive Maltese cross must be a sign of the highly ordered vertical alignment of LC molecules on the PS nanorod arrays. In brief, vertical LC alignment appeared for larger diameters ($D_p > 55$ nm), whereas random LC alignment was observed for smaller diameters. It is interesting that only the slight variation of lateral dimension of the nanostructure changes the LC orientation dramatically. The transition of LC alignment from random to vertical orientation occurred only in a small change of diameter of nanorod. Frustration, induced by nanoscopic confinement, would be imposed more strongly

on the LC with increasing rod diameter, because the separation between them became narrower. The gap between the two adjacent nanorods decreased with increasing diameter of the PS nanorods with the same periodicity of nanopatterns (~110 nm) in this experiment. Therefore, the vertical orientation of LCs could be observed when the diameter, or degree of constraint, is above a certain level.

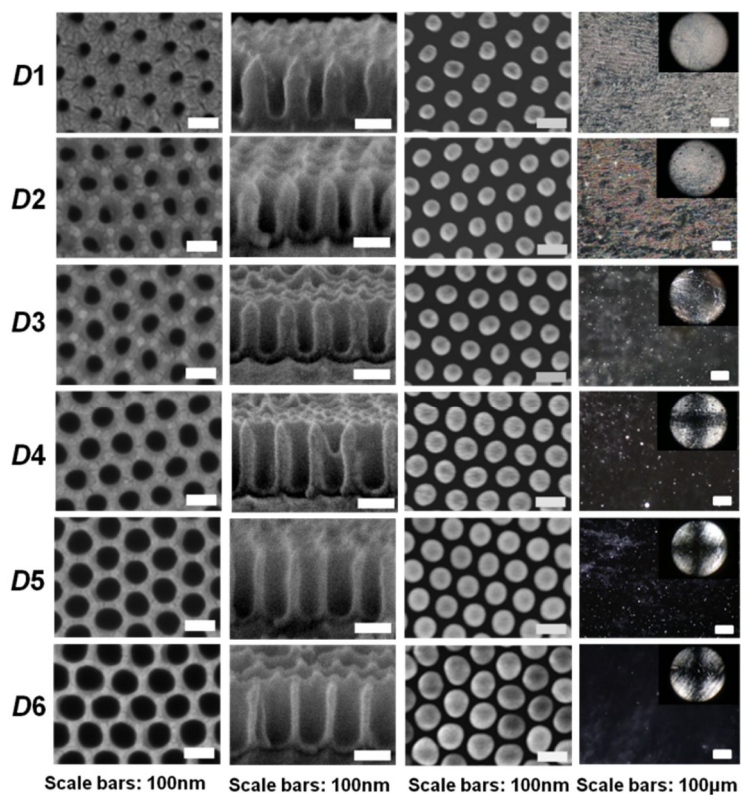


Figure 5.4. SEM images of diameter-controlled AAO templates and PS nanorod arrays ranging from 38 nm to 86 nm and POM images of LC cell. SEM images: (a) top view and (b) side view of diameter-controlled AAO templates, (c) top view of PS nanorod arrays. (d) POM images of LC cells. Insets: conoscopic images.

The LC alignment on the highly ordered nanostructured substrates was also examined with the variation of the length of the nanorods with a fixed rod diameter. SEM images of length-controlled nanoporous AAO templates were given in the first column in Figure 5.5. The lengths of nanopores were 80 nm ($L1$), 113 nm ($L2$), 153 nm ($L3$) and 187 nm ($L4$), respectively. Since PS melt was drawn into the nanopores via capillary wetting under vacuum, PS melt filled the whole nanopores and PS nanorod arrays were highly replicated from each AAO templates. As shown in the $\sim 45^\circ$ -tilt SEM images in the second column of Figure 5.5, the top surfaces of the rods are not depressed down but convexed upward. It implies that PS melt filled the whole nanopores and the lengths of the rods must be the same as the lengths of the nanopores. The diameter of PS nanorods was 68 ± 4 nm, which is similar for all films (the third column of Figure 5.5). The POM images represent that the LC alignment altered with the change of lengths of the nanorods (the fourth column of Figure 5.5). When the PS nanorods were shorter, the orientation of the LC molecules on the nanostructured PS film was the same as on a flat film. A mixed random planar and tilted orientation appeared at $L_p \sim 80$ nm ($L1$). However, the change in LC orientation occurred with the increase of the nanorod length. When $L_p \sim 113$ nm ($L2$), the alignment of LC molecules began to change to a partial vertical orientation from random. The uniform vertical orientation of LC molecules was finally found for $L_p \sim 153$ nm ($L3$) and $L_p \sim 187$ nm ($L4$). In short, the LC molecules on shorter rods were randomly oriented, whereas they were oriented perpendicularly to the substrate plane on longer rods ($L_p > 113$ nm). It is noteworthy that, upon the slight variation of rod lengths (~ 33 nm), sharp shift of LC alignment from random to homeotropic orientation also appeared as in the variation of diameters.

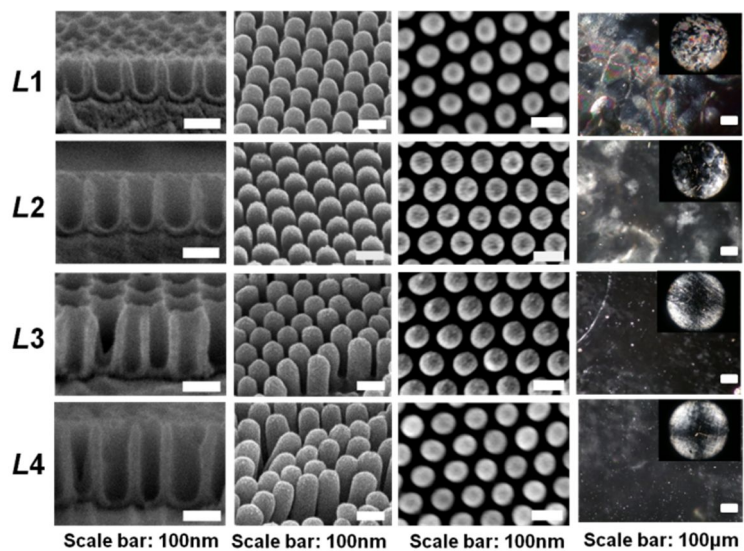


Figure 5.5. SEM images of length-controlled AAO templates and PS nanorod arrays ranging from 80 nm to 187 nm and POM images of LC cell. SEM images: (a) side view of length-controlled AAO templates, (b) tilt view and (c) top view of PS nanorod arrays. (d) POM images of LC cells. Insets: conoscopic images.

Near the nanorod surface, LC molecules would suffer from the elastic distortion because of local packing disorder of LC molecules along surface topography, and this distortion would require higher elastic energy than that on flat surface in the presence of curvature. The alignment of LC molecules in the absence of external field can be given by the sum of the elastic free energy and the surface free energy. The Frank elastic energy is given as

$$f = \frac{1}{2} \{K_{11}(\nabla \cdot n)^2 + K_{22}[n(\nabla \cdot n)]^2 + K_{33}[n \times (\nabla \times n)]^2\},$$

where K_{11} , K_{22} , and K_{33} are the splay, twist, and bend elastic coefficient, respectively [24]. The surface free energy is defined as by Rapini-Papoular form

$$f_{\Lambda} = \left(\frac{\omega}{2}\right) \sin^2(\emptyset - \theta),$$

where ω , \emptyset , and θ represent the anchoring strength, the preferred anchoring angle of easy axis, and the actual angle of director, respectively [25]. Upon imposing larger curvature and higher degree of confinement, the assembly of LC molecules should rearrange in order to reduce additional elastic strain energy occurring from molecular packing conforming to surface topography. So, the transition of LC molecules to vertical alignment resulted in the energy minimization by reorientation, and then the local packing of LC molecules at the interface propagates to intermediate region in LC cell, and determines the alignment of LC molecules in the cell. It is expected that surface nanopatterns provide more compulsory deformation of LC molecules than micrometer- or submicrometer-scale patterns, because packing of LC molecules is usually on nanoscale. Thus, the packing of LC molecules in the nanoscopic space undergoes severe distortion, and it increases the Frank elastic energy. The appearance of LC alignment transition in such a small difference of PS nanorod size is thought to be strongly correlated with

a large perturbation of molecular packing by geometrical constraint. Yi *et al.* observed the shift of LC (4-pentyl-4'-cyanobiphenyl) alignment from random to homeotropic alignment on poly(methyl methacrylate) square patterns (periodicity~hundreds of nanometers) with the decrease of pattern size [11]. In this study, however, the increase of pattern size induces the orientation change from random to vertical alignment. The difference between the previous and current study is ascribed to magnitude of pattern scale. The nanopatterns of our study are so small enough to give strong perturbation to LC molecules, and thus a slight increase of pattern size makes the LC molecules align. But, larger patterns of the previous study couldn't impose enough constraint on LC molecules. So, contrary to the current observation, LC alignment may be obtained by reducing the pattern dimension. Moreover, it should be noted that interfacial tension between the substrate and the LC molecules be another important factor to determine the orientation of LC molecules, as indicated by Rapini-Papoular form of surface free energy [26-28]. The interfacial free energy as well as the degree of confinement should be within a suitable range in order to control the LC alignment in the current method.

5.4. Conclusion

In conclusion, we found that the alignment of LC molecules on the nanostructured substrates is affected severely by the diameter and length of the PS nanorods. Homeotropic alignment of the LC molecules on these substrates was observed, as the diameter or length of nanorods became larger or longer within the range of the current experiment. Since the size of the nanoscopic pattern is comparable to the scale of characteristic packing of the LC molecules, the transition of LC alignment is thought to be caused by the packing frustration on the LC molecules imposed by the nanoscopic confinement. The sub-wavelength size of the nanoscopic pattern would provide uninfluenced or enhanced optical property due to Mie scattering as well as thermodynamic stability. This method might not be as economical as other conventional LC aligning methods. However, owing to self-assembly based, easy, and precise fabrication in a large area, our current approach could be still useful in the manufacture of LC devices such as the vertical alignment mode in flexible display devices. Considering that repetitive manufacture of the nanorod arrays is available [30], this method, using geometrical patterned substrate, could be another simple and robust alternative to tune the orientation of small organic molecules including LC.

5.5. References

- [1] K. W. Noh, E. Woo, K. Shin, *Chem. Phys. Lett.* **2007**, *444*, 130.
- [2] K. Shin, E. Woo, Y. G. Jeong, C. Kim, J. Huh, K. –W. Kim, *Macromolecules*, **2007**, *40*, 6617.
- [3] K. Shin, H. Q. Xiang, S. I. Moon, T. Kim, T. J. McCarthy, T. P. Russell, *Science*, 2004, *306*, 76.
- [4] M. Steinhart, P. Göring, H. Dernaika, M. Prabhakaran, U. Gösele, E. Hempel, T. Thurn-Albrecht, *Phys. Rev. Lett.*, **2006**, *97*, 027801.
- [5] M. Steinhart, S. Senz, R. B. Wehrspohn, U. Gösele, J. H. Wendorff, *Macromolecules*, **2003**, *36*, 3646.
- [6] T. Thurn-Albrecht, J. Schotter, G. A. Kästle, N. Emley, T. Shibauchi, L. Krusin-Elbaum, K. Guarini, C. T. Black, M. T. Tuominen, T. P. Russell, *Science*, **2000**, *290*, 2126.
- [7] E. Woo, J. Huh, Y. G. Jeong, K. Shin, *Phys. Rev. Lett.* **2007**, *98*, 136103.
- [8] J. van Haaren, *Nature*, **2001**, *411*, 29.
- [9] N. A. J. M. van Aerle, A. J. W. Tol, *Macromolecules*, **1994**, *27*, 6520.
- [10] K. Weiss, C. Wöll, E. Böhm, B. Fiebranz, G. Forstmann, B. Peng, V. Scheumann, D. Johannsmann, *Macromolecules*, **1998**, *31*, 1930.
- [11] Y. Yi, G. Lombardo, N. Ashby, R. Barberi, J. E. MacLennan, N. A. Clark, *Phys. Rev. E* **2009**, *79*, 041701.
- [12] S. Lazarouk, A. Muravski, D. Sasinovich, V. Chigrinov, H. S. Kwok, *Jpn. J. App. Phys.* **2007**, *46*, 6889.
- [13] T. Maeda, K. Hiroshima, *Jpn. J. App. Phys.* **2004**, *43*, L1004.

- [14] T. Maeda, K. Hiroshima, *Jpn. J. App. Phys.* **2005**, *26*, L845.
- [15] T. -T. Tang, C. -Y. Kuo, R. -P. Pan, J. -M. Shieh, C. -L. Pan, *J. Disp. Technol.* **2009**, *5*, 350.
- [16] D. W. Berreman, *Phys. Rev. Lett.* **1972**, *28*, 1683.
- [17] D. W. Berreman, *Mol. Cryst. Liq. Cryst.* **1973**, *23*, 215.
- [18] A. Sugimura, N. Yamamoto, T. Kawamura, *Jpn. J. App. Phys.* **1981**, *20*, 1343.
- [19] Y. Yi, M. Nakata, A. R. Martin, N. A. Clark, *Appl. Phys. Lett.* **2007**, *90*, 163510.
- [20] S. -R. Kim, A. I. Teixeira, P. F. Nealey, A. E. Wendt, N. L. Abbott, *Adv. Mater.* **2002**, *14*, 1468.
- [21] J. B. Kim, J. S. Park , H. J. Ahn, M. J. Lee, S. J. Jo, M. Kim, D. Kang, Y. S. Kim, S. J. Lee, H. K. Baik, *Adv. Funct. Mater.* **2008**, *18*, 1340.
- [22] F. S. Yeung, J. Y. Ho, Y. W. Li, F. C. Xie, O. K. Tsui, P. Sheng, H. S. Kwok, *Appl. Phys. Lett.* **2006**, *88*, 051910.
- [23] H. Masuda, K. Fukuda, *Science* **1995**, *268*, 1466.
- [24] F. C. Frank, *Discuss. Faraday Soc.* **1958**, *25*, 19.
- [25] A. Rapini, M. Papoular, *J. Physique Coll.* **1969**, *30*, C4.54.
- [26] T. Bellini, N. A. Clark, V. Degiorgio, F. Mantegazza, G. Natale, *Phys. Rev. E* **1998**, *57*, 2996.
- [27] A. D. Price, D. K. Schwartz, *Langmuir* **2006**, *22*, 9753.
- [28] D.-R. Chiou, Li.-J. Chen, *J. Phys. Chem. C* **2009**, *113*, 9797.
- [29] H. J. Ahn, J. B. Kim, K. C. Kim, B. H. Hwang, J. T. Kim, H. K. Baik, J. S. Park, D. S. Kang, *Appl. Phys. Lett.* **2007**, *90*, 253505.
- [30] D. Y. Lee, D. H. Lee, H. S. Lim, J. T. H. Han, K. Cho, *Langmuir* **2010**, *26*, 3252.

Chapter 6.
Surface Wettability and Topography Effect
on LC Alignment

6.1. Introduction

As one of the most conventional methods to control the alignment of liquid crystals (LCs), surface rubbing has been developed and widely used [1-4]. Mechanical rubbing is simple and economic, but, it cannot give inherent stability to the LC alignment. There have been studies to control the LC orientations that would make the alignment of LC stable. It has been suggested that the alignment of LCs on a solid substrate can be possibly influenced by the chemical nature and roughness of surface [5]. In terms of chemical nature of surface, when the surface free energy is relatively low, it was reported that the intermolecular forces between LC molecules would be stronger than the forces between the LC and the substrate [5]. As the critical surface free energy of the solid substrate is greater than that of LCs, the intermolecular forces at the interface of LC/substrate would dominate and the orientation of LCs could be changed [5]. Price and Schwartz investigated the alignment behavior of nematic LCs (5CB, 4'-*n*-pentyl-4-cyanobiphenyl) with increasing surface wettability and observed the transition from homeotropic (vertical) to tilted orientation [6]. Park et al. reported that the azimuthal and polar alignments of LCs are determined by chemical patterns on the surface [7]. Thus, there have been approaches to control the alignment of LCs via chemical modification of substrate surfaces [8-10]. Also, it has been suggested to control of LC orientation by use of the structural variation of substrate surface. Followed by Berreman's argument, it has been demonstrated that the alignment of LCs could be manipulated by surface geometry [11-19]. A surface structure on the substrate has been reported to induce LC alignment with a high order parameter [20]. Yeung and

coworkers observed that the pretilt angles of LCs can be controlled from 0 to 90° by the introduction of polyimide nanostructures [21].

As technology on nanoscale sciences advances, several methods were suggested for the generation of nanoscopic patterns during the last decades. Especially via self-assembly, regular and uniform nanopatterns can be manufactured economically, and it enables usage of the nanopatterns for a wide range of purposes available. It has been only recently demonstrated that the alignment of LC mixtures on uniform highly ordered polystyrene nanorod arrays changes from random planar to homeotropic orientation on the dimensional variation of the nanoscopic surface structures [22]. It is expected that the surface chemical nature of the topographical structure may have an influence on the orientation of LCs. However, approaches with uniform nanoscale-surface structured materials are limited so far. In this study, we investigate the effect of the surface chemical nature and surface topography on the LC alignment. Several photocurable polymers with different surface free energies (12.15, 24.91, and 44.66 mN/m) were used to examine the effect of surface interaction on the alignment of LC. Nanoscopic topography was obtained using diameter-controlled nanoporous anodized aluminum oxide (AAO) templates via replica molding [23]. The UV-assisted nanomolding provides the simple fabrication of polymer templates for the tuning of LC alignment and makes AAO template reusable [24, 25].

6.2. Experimental Section

Schematic illustration of the experimental procedures is given in Figure 6.1. The details are as follows:

Preparation of nanoporous AAO templates:

Anodic aluminum oxide (AAO) template was fabricated by conventional two-step anodization method. An Al sheet (99.999% thickness ~0.5 mm, Goodfellow) was electropolished in a mixture of perchloric acid and ethanol (HClO_4 : $\text{C}_2\text{H}_5\text{OH}$ = 1:4 by volumetric ratio) at 20V to reduce the surface roughness. Then, the flattened Al sheet was anodized in a 0.3 M oxalic acid solution ($\text{H}_2\text{C}_2\text{O}_4$) at 40V for 12-16 hrs. After the first anodization, the Al_2O_3 layer was selectively etched away from the aluminum sheet in a mixture of chromic acid (H_2CrO_4) and phosphoric acid (H_3PO_4) solution. The second anodization was performed for 100~120 s to fabricate highly ordered nanopores under the same conditions as the first anodization. The nanopores were widened by immersing in a 0.1M phosphoric acid solution at 30 °C for 10-60 min.

Replication of UV-curable polymer substrates from AAO templates:

Three UV-curable polymers were used for the manufacture of nanostructured surfaces; perfluoropolyether (PFPE, Solvay Solexis), polyurethane acrylate (PUA, Minuta Tech.), and trimethylolpropane propoxylate triacrylate (TPT, Aldrich). PFPE and TPT precursor solutions were prepared by mixing with photoinitiator, 2-hydroxy-2-methylpropiophenone. To minimize adhesion between photocurable

polymers and AAO templates, surface modification of nanopores was required [26]. The AAO template was treated with oxygen plasma at 30W with the gas flow rate of 10.3 sccm for 2 min at 100-200 mTorr (RIE-3000, South Bay Technology, Inc.). The AAO template was immersed in a 0.5 wt.% aqueous of 3-(aminopropyl triethoxysilane) (APTES, Aldrich) for 10 min. Unreacted APTES was washed with distilled water. Then, the APTES-treated templates was reacted with monoglycidyl ether-terminated poly(dimethylsiloxane) (PDMS, $M_n = 5000$, Aldrich) at 80 °C for 4 hr. To remove unreacted PDMS, the templates were immersed in isopropyl alcohol with sonication for 1 min. The mixture of UV-curable prepolymer and curing agent were poured onto nanoporous AAO templates, and polyethylene terephthalate (PET) film (thickness~50 μm) was put on the polymer layers. The prepolymer filled the cavity by capillary force, and were then irradiated with UV light ($\lambda \sim 365$ nm) for several hours. After UV curing, crosslinked polymer networks were formed, and the polymer replica was slowly peeled off from the AAO template.

The LC cell assembly:

The LC cells (~ 1.5 cm \times 1.5 cm) were assembled with spacers of 4.5 μm in diameter. A nematic LC, MLC-7026-000 (Merck Co., $\Delta\epsilon < 0$), was introduced into the LC cell via capillary action at room temperature.

Characterization:

The surface of AAO template and UV-curable polymer replica were analyzed by field-emission scanning electron microscopy (FE-SEM, JSM-6701F, JEOL) after platinum coating. LC orientation was analyzed by polarized optical microscopy

(POM) (Nikon, ECLIPSE E600 POL) equipped with polarizers and digital camera (Nikon, COOLPIX995). The static contact angles of distilled water, methylene iodide, and MLC-7026-000 on the flat film and nanostructured UV-curable polymer film were measured using a CAM-200 (KSV) contact angle analyzer.

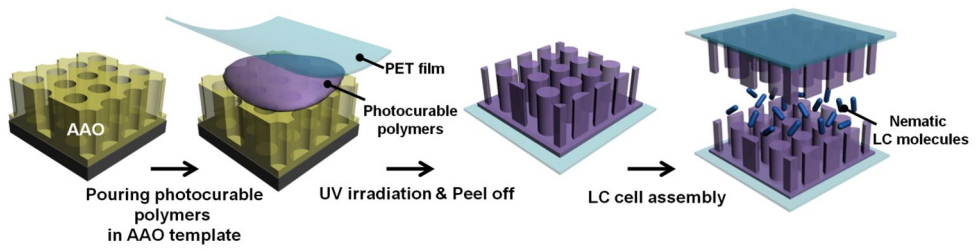


Figure 6.1. Schematic route to the LC cells with the polymer nanorod arrays via UV-assisted nanomolding with AAO templates.

6.3. Results and Discussion

SEM images of home-made AAO templates are shown in Figure 6.2. The diameters of nanopores in the SEM images from top to bottom were approximately 37 nm ($D1$), 47 nm ($D2$), 60 nm ($D3$), 70 nm ($D4$), and 83 nm ($D5$), respectively. The length of nanopores for all templates was fixed as $\sim 138 \pm 6$ nm. The SEM images of the highly ordered hexagonal pore arrays represent that the dimension of each nanopore is precisely controlled.

The contact angles of water and methylene iodide (MI) on a polymeric solid surface implicates the information on surface properties, because the contact angle, or wetting of liquid on a substrate, is sensitive to chemical nature and structures of the surface [27]. We measured the water and MI contact angles, and then calculated the surface free energy of each polymeric surface (PFPE, PUA, and TPT) using Owens-Wendt model. The Owens-Wendt model is give as

$$(\gamma_s^d \gamma_l^d)^{0.5} + (\gamma_s^p \gamma_l^p)^{0.5} = 0.5 \gamma_l (1 + \cos \theta)$$

where γ is surface free energy, the subscript s and l indicates a solid and a liquid, and the superscript d and p denotes the dispersive and polar component of surface free energy, respectively [28]. The dispersive, polar, and total surface free energy of PFPE, PUA, and TPT, calculated by Owens-Wendt model, are summarized in Table 1. The total surface free energies of PFPE, PUA, and TPT are 12.15 mN/m, 24.91 mN/m, and 44.66 mN/m, respectively (Table 6.1).

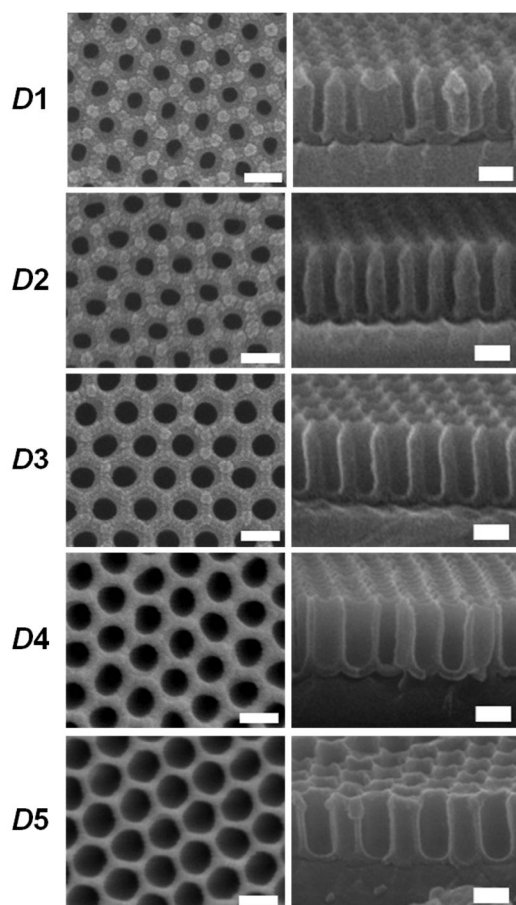


Figure 6.2. Top and cross-sectional SEM images of the diameter-controlled AAO templates. *D1*: 37 nm, *D2*: 47 nm, *D3*: 60 nm, *D4*: 70nm, and *D5*: 83 nm with the fixed *L* ($\sim 138\pm 6$ nm) for all templates. Scale bars are 100 nm.

	γ_s^d	γ_s^p	γ_s
	mN/m		
Perfluoropolyether, PFPE	10.13	2.02	12.15
Polyurethane Acrylate, PUA	23.17	1.74	24.91
Trimethylolpropane Propoxylate Triacrylate, TPT	37.88	6.78	44.66

Table 6.1. Surface free energy of photocurable polymer. The dispersive, polar, and total surface free energy was calculated followed by Owens-Wendt model.

The diameter-controlled AAO templates were employed as a primary mold for the preparation of topographically patterned polymer substrates. The SEM images in Figure 6.3 show the surface nanostructures of photocurable polymer according to the diameter of nanorods and the insets depict conoscopic images. Each nanorod of PFPE, PUA, and TPT was highly replicated from AAO templates, and the diameters of nanorods appeared similar to the diameter of nanopores of AAO template, although there is a possibility of volume change during crosslinking. Since the photocurable prepolymer in a liquid state are infiltrated into nanopores via wetting on the surface of pore wall, the rods are highly replicated from the master AAO template. Nevertheless, it is observed that some nanorods are stuck together and partially collapsed each other for the rods with larger diameter probably due to van der Waals' interaction among nanorods. The spacing between nanorods becomes closer as the nanorod diameter increases with the fixed center-to-center distance, and thus attractive interaction among nanorods is thought to make the rods collapse together. Among three types of polymeric materials, the vertical alignment of LCs was discovered in only PUA nanorod surface with larger diameter in conoscopic POM images of Figure 6.3. The fully vertical alignment was observed in $D \sim 70$ nm, whereas the weak vertical alignment was shown in $D \sim 83$ nm. It was thought that the order of vertical alignment of LC molecules could be restricted by the partially collapsed nanorod arrays in larger diameter.

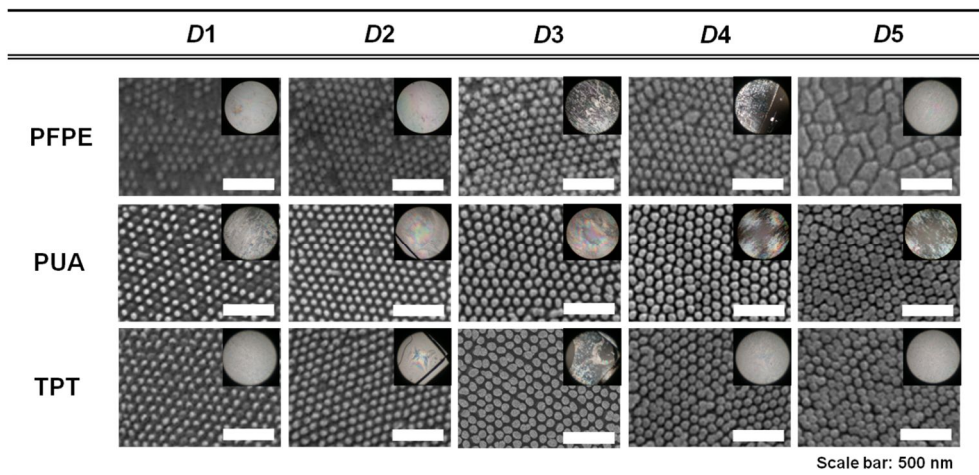


Figure 6.3. Top view SEM images of the photocurable polymer nanorod arrays replicated from the diameter-controlled AAO templates and the conoscopic images.

In the absence of external electromagnetic fields, it has been reported that the orientation of nematic LCs is governed by forces working in vicinity of the LC-substrate interface [29]. The contact angle is an experimentally available measurement for the calculation of the surface energy at the interface, and can make a guess for the alignment tendency. We measured the water and MI contact angles for the comparison of the surface energy of each diameter-controlled polymer substrate. For a nanostructured surface, the surface energy is determined by the combination effect of compositional nature and topography. Although the surface energy can be increased/decreased in comparison with the flat surface when nanostructures are introduced on the surface, there was no distinctive difference of the surface energy with the variation of nanorod diameter (Figure 6.4). Thus, we directly measured the surface wettability of the LC droplet on each polymer substrate (diameter~ D_4), which exhibited different LC alignment depending on the type of photocurable polymer in Figure 6.3, to examine the effect of interfacial interaction between the LC molecules and photocurable polymeric substrates more qualitatively. In order to generate the transition of LC alignment by the change of nanorod size, the LC molecules should penetrate into the space between nanorods. The contact angles of LCs on flat and D_4 substrate surface with the elapsed time (<13 s) are shown in Figure 6.5. The contact angle of LC droplet on all substrates became steady after 13 s. Figure 6.5 (a) shows that the contact angle of the LC on PFPE substrate gets $\sim 30^\circ$ higher than that of flat surface, right after the placing the LC on the PFPE substrate. Considering that the volume of the LC droplet appeared as the same with the elapsed time, there is a possibility that the LC molecules on nanostructured PFPE surface could not penetrate into the space between PFPE nanorods due to repelling nature of PFPE against the LCs, and thus the alignment

of the LC molecules could not be influenced by the variation of nanorod diameter.

In the mean time, the contact angle of the LC on PUA and TPT substrates becomes lower than that on flat surfaces, as shown in Figure 6.5 (b) and (c), respectively. After the placement of LC droplet on the PUA and TPT substrate, the LC droplet seemed to penetrate into the space between nanorods immediately, and the height of the drop decreases apparently. The apparent spread of the droplet (or decrease of the height) with the elapsed time implicates that the LC molecules would penetrate into the space between nanorods, and the orientation of the LC molecules would be completely influenced by confinement imposed by the structure of the surface. Associated with the LC alignment in Figure 6.3, the change of LC alignment was observed in nanostructured PUA substrates only. It can be explained that the LC alignment on nanorod arrays is determined by two competition interactions; LC-LC interaction and LC-substrate interaction. For TPT substrate, the LC droplet was easily spread on flat and nanostructured surface, given in Figure 6.4 (c). It means that the attraction between the polar group of the nematic LC molecules and TPT surface could be stronger because of hydrophilic nature (~ 45 mN/m) of TPT surfaces. Thus, the interaction at the LC-TPT interface (polar-polar interaction) could be dominant over the LC-LC interaction by geometrical environment. In addition, the nanostructured TPT surfaces have higher surface energy than that on flat surface. It was considered that the LCs on flat and nanostructured surface preferred randomly planar alignment. As a result, the interfacial free energy or the degree of confinement may not be within a suitable range. However, for PUA substrate, it seemed that the change of LC alignment would be induced by the degree of nanoconfinement. Compared with PFPE and TPT substrate, PUA substrate has relatively moderate surface energy (~ 24.91

mN/m), which is the intermediate value between TPT and PFPE surface energy. When the LC molecules were onto the flat PUA surface without a weak spatial restriction, they preferred randomly planar alignment. However, nanoscopic confinement would be imposed more strongly on the LC molecules with the increase of nanorod diameter, the LC molecules could intensely interact each other because the center-to-center distance between nanorods is fixed and the separation between nanorods gets narrower [30-32]. The alignment of LC molecules in the absence of an external field can be given by the sum of the elastic free energy and the surface free energy. The elastic free energy density of Frank is given as

$$f = \frac{1}{2} \{K_{11}(\nabla \cdot n)^2 + K_{22}[n(\nabla \cdot n)]^2 + K_{33}[n \times (\nabla \times n)]^2\},$$

where K_{11} , K_{22} , and K_{33} are the splay, twist, and bend elastic coefficient, respectively [33]. The surface free energy density is defined as

$$f_A = \left(\frac{\omega}{2}\right) \sin^2(\phi - \theta),$$

by Rapini-Papoular form, where ω , ϕ and θ represent the anchoring strength, the preferred anchoring angle of easy axis, and the actual angle of director, respectively [34]. The surface chemical composition does not change according to surface topography, so we assumed that the surface anchoring energy was constant regardless of surface roughness. When the surface anchoring energy is in a moderate range, the packing of LC molecules under spatial restriction could be affected by the degree of confinement. Upon imposing a higher degree of confinement, the packing of LC molecules would go through severe elastic distortion and it increases the Frank elastic energy. Consequently, the LC molecules reorient in order to reduce additional elastic strain energy by surface topography. Thus, it is conjectured that the transition to homeotropic alignment would result in

energy minimization under nanoconfinement.

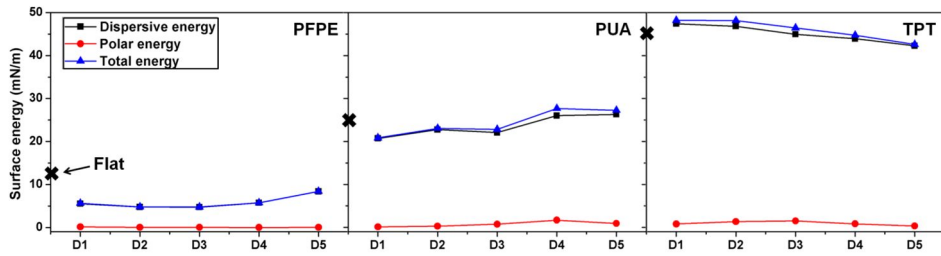


Figure 6.4. The surface energy of nanostructured PFPE, PUA, and TPT surfaces with the diameter variations ($D1$ - $D5$).

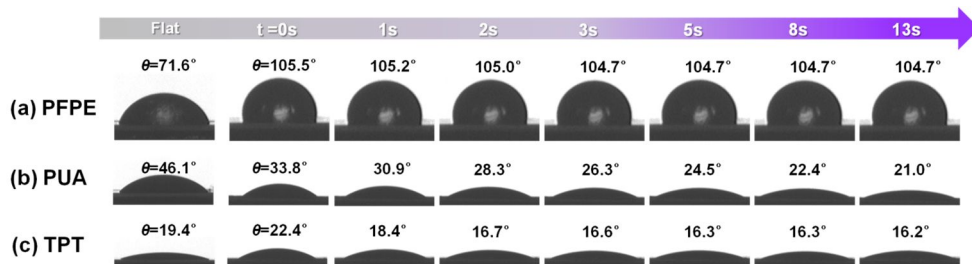


Figure 6.5. The change of the LC contact angles on flat and $D4$ substrates with the elapsed time (< 13 s); PFPE (a), PUA (b), and TPT (c).

In addition, we thought that the LC molecules have different orientation behavior on PFPE, PUA, and TPT surface because each polymer has different chemical nature. Thus, x-ray diffraction (XRD) measurements were performed using the synchrotron source on 9A beamline at the Pohang Accelerator Laboratory (PAL) in Korea (exposure time=5s except PFPE sample (20s)). At $1.25 < q < 1.5$, we observed a sharp peak and expected that it indicates the peak of bulk MLC, which has the spacing (d) of ~ 4.5 Å (Figure (a) and (b)). Unfortunately, we couldn't find any peak of MLC on PET surfaces. In fact, the PFPE, PUA, and TPT alignment layer were fabricated on PET film via the UV-assisted molding. So, we conjectured that the peak of MLC was hidden due to strong PET peak. As a result, we couldn't demonstrate the difference of the LC orientation on each polymer surface.

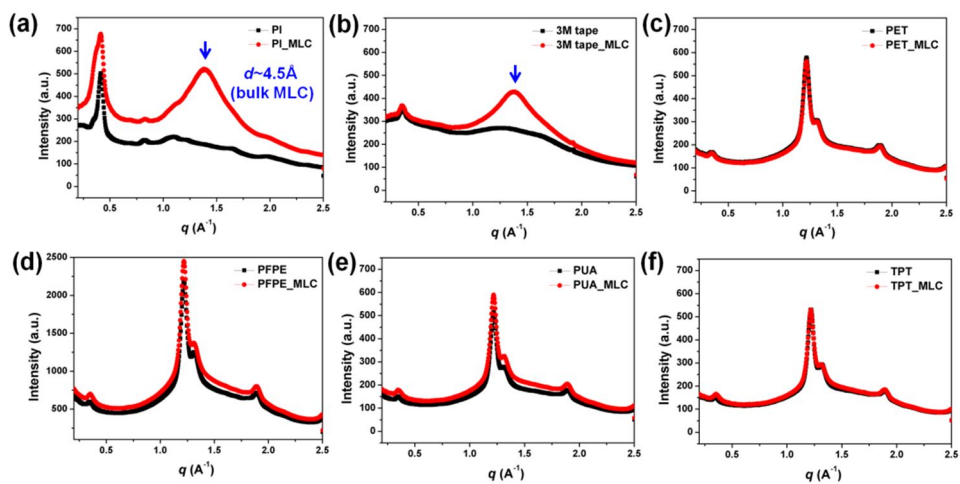


Figure 6.6. XRD analysis of LC cell with polyimide (a), 3M tape (b), PET (c), PFPE (d), PUA (e), and TPT (f).

In order to examine the effect of variation of interfacial free energy at the interface between the LC molecules and the topographically patterned polymeric substrates, we coated thin organic film (3-(aminopropyl triethoxysilane) (APTES) and poly(dimethylsiloxane) (PDMS)) on the surfaces of the PUA replicas. Here, the water contact angle of the flat surface coated with APTES and PDMS was very similar to that of TPT ($\sim 68.3^\circ$) and PFPE ($\sim 109.2^\circ$), respectively. The LC molecules showed different alignment behavior on the PUA substrates coated with APTES or PDMS, as compared to the one on the pristine nanostructured substrates. It was found that the LC alignment on the nanostructured PUA substrates only without surface-coating was governed by the nanorod size. While the homeotropic alignment on the PUA substrate was observed in larger diameter, such alignment was not found in APTES-coated PUA and PDMS-coated PUA substrate examined within the same range of nanorod dimension as in the pristine PUA substrate. In turn, it can be explained that the alignment of the LC molecules can be influenced by the chemical nature (surface wettability) of thin outermost surface as well as surface topography (the degree of confinement).

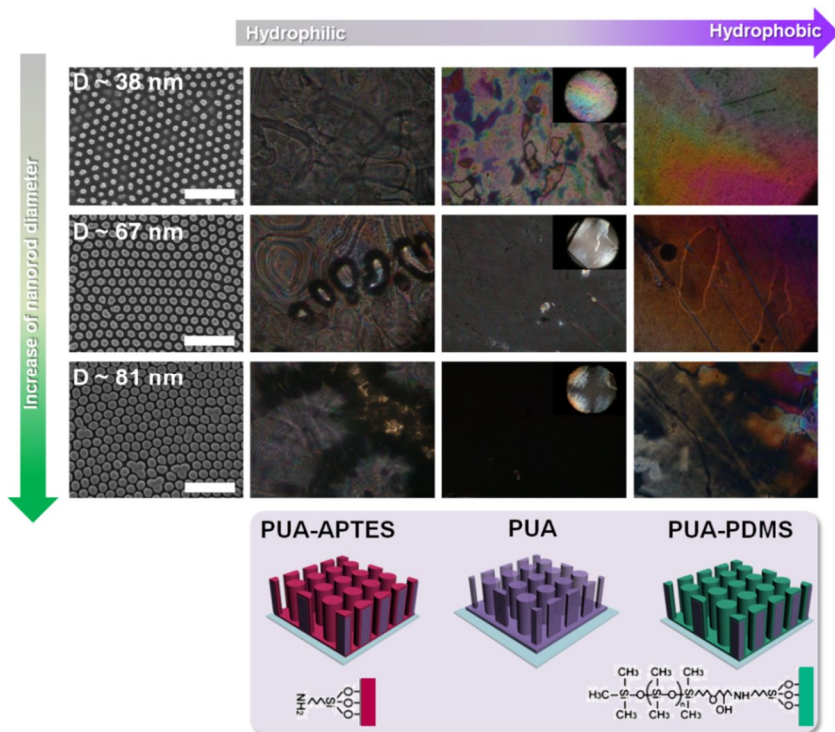


Figure 6.7. SEM and POM images of PUA, APTES-coated PUA, and PDMS-coated PUA substrates. Scale bars are 100 nm.

The schematic illustration in Figure 6 helps the understanding of LC molecular alignment on flat and nanostructured polymeric surfaces. LC molecules prefer randomly planar orientation on flat surfaces, and there is no difference of LC alignment according to the surface energy of the photocurable polymers. However, for the polymeric surface with moderate surface energy (PUA surface), the alignment state is influenced by the nanorod size. In this examination, the LC molecules aligned homeotropically above the critical nanorod diameter (D_c) because the assembly of LC molecules could rearrange in order to reduce the additional elastic energy occurring from the surface topography under higher degree of confinement.

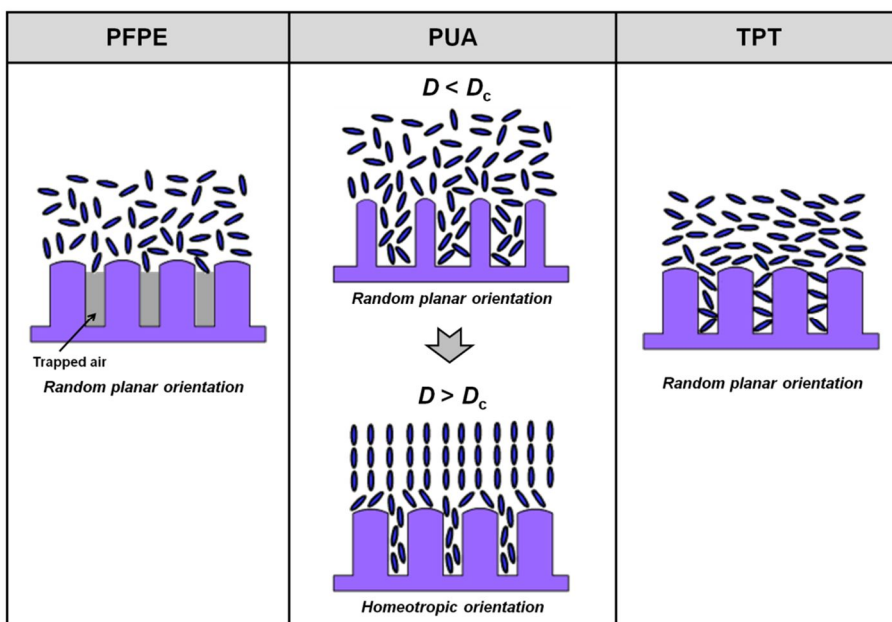


Figure 6.8. Schematic illustration of LC alignment on PFPE, PUA, and TPT nanorod arrays on the basis of the degree of confinement.

6.4. Conclusion

In conclusion, we demonstrated the combined influence of surface chemical compositions and nanoscopic topography on the LC alignment. We discovered that the vertical alignment of the LC molecules on the photocurable polymer nanorod arrays is determined by both surface chemical nature and topography. The change of the LC alignment with the variation of the diameter of nanorod is found on the PUA substrates with the intermediate surface free energy (24.91 mN/m) in this study. The transition from random planar to homeotropic alignment was observed, as the diameter of the nanorod goes larger ($D > 60$ nm). The current study implicates that interfacial free energy and surface roughness would be in a suitable range in tuning the LC alignment. Most of all, in order to make the surface structure effective in the control of the LC orientation, it should be the basic premise that the LC molecules should wet and penetrate the spaces between nanorods which would impose strong confinement on the LC molecules. In addition, we believe that this work can be useful for understanding of the LC alignment behavior in vertical alignment (VA) mode for flexible LC display applications.

6.5. References

- [1] S.W. Lee, B. Chae, H.C. Kim, B. Lee, W. Choi, S.B. Kim, T. Chang, M. Ree, *Langmuir* **2003**, *19*, 8735.
- [2] J. van Haaren, *Nature* **2001**, *411*, 29.
- [3] N. Vanaerle, A.J.W. Tol, *Macromolecules* **1994**, *27*, 6520.
- [4] K. Weiss, C. Woll, E. Bohm, B. Fiebranz, G. Forstmann, B. Peng, V. Scheumann, D. Johannsmann, *Macromolecules* **1998**, *31*, 1930.
- [5] L.T. Creagh, A.R. Kmetz, *Mol. Cryst. Liq. Cryst.* **1973**, *24*, 59.
- [6] A.D. Price, D.K. Schwartz, *Langmuir* **2006**, *22*, 9753.
- [7] S. Park, C. Padeste, H. Schiff, J. Gobrecht, T. Scharf, *Adv. Mater.* **2005**, *17*, 1398.
- [8] B.H. Hwang, C.J. Choi, M.K. Jo, J.B. Kim, H.M. Choi, S.S. Chae, Y.S. Kim, H.K. Baik, *Langmuir* **2010**, *26*, 5072.
- [9] J.B. Kim, C.J. Choi, J.S. Park, S.J. Jo, H.H. Hwang, M.K. Jo, D. Kang, S.J. Lee, Y.S. Kim, H.K. Baik, *Adv. Mater.* **2008**, *20*, 3073.
- [10] S.K. Oh, M. Nakagawa, K. Ichimura, *J. Mater. Chem.* **2001**, *11*, 1563.
- [11] D.W. Berreman, *Phys. Rev. Lett.* **1972**, *28*, 1683.
- [12] D.W. Berreman, *Mol. Cryst. Liq. Cryst.* **1973**, *23*, 215.
- [13] Y. Kawata, H. Takatoh, M. Hasegawa, M. Sakamoto, *Liq. Cryst.* **1994**, *16*, 1027.
- [14] J.B. Kim, J.R. Lim, J.S. Park, H.J. Ahn, M.J. Lee, S.J. Jo, M. Kim, D. Kang, S.J. Lee, Y.S. Kim, H.K. Baik, *Adv. Funct. Mater.* **2008**, *18*, 1340.
- [15] S. Lazarouk, A. Muravski, D. Sasinovich, V. Chigrinov, H. S. Kwok, *Jpn. J.*

- Appl. Phys.* **2007**, *46*, 6889.
- [16] B.W. Lee, N.A. Clark, *Science* **2001**, *291*, 2576.
- [17] T. Maeda, K. Hiroshima, *Jpn. J. Appl. Phys.* **2004**, *43*, L1004.
- [18] Y. Yi, G. Lombardo, N. Ashby, R. Barberi, J.E. MacLennan, N.A. Clark, *Phys. Rev. E* **2009**, *79*, 041701.
- [19] Y. Yi, M. Nakata, A.R. Martin, N.A. Clark, *Appl. Phys. Lett.* **2007**, *90*, 163510.
- [20] A. Sugimura, N. Yamamoto, T. Kawamura, *Jpn. J. Appl. Phys.* **1981**, *20*, 1343.
- [21] F.S. Yeung, J.Y. Ho, Y.W. Li, F.C. Xie, O.K. Tsui, P. Sheng, H.S. Kwok, *Appl. Phys. Lett.* **2006**, *88*, 051910.
- [22] K. Lee, H. Kang, J.-C. Lee, D. Kang, K. Shin, *Liq. Cryst.* **2011**, *38*, 1131.
- [23] Masuda, H.; Fukuda, K. *Science* **1995**, *268*, 1446-1468.
- [24] M.K. Choi, H. Yoon, K. Lee, K. Shin, *Langmuir* **2011**, *27*, 2132.
- [25] D.Y. Lee, D.H. Lee, H.S. Lim, J.T. Han, K. Cho, *Langmuir* **2010**, *26*, 3252.
- [26] M.J. Lee, N.Y. Lee, J.R. Lim, J.B. Kim, M. Kim, H.K. Baik, Y.S. Kim, *Adv. Mater.* **2006**, *18*, 3115.
- [27] M. Zenkiewicz, *J. Achieve. Mater. Manufac. Eng.* **2007**, *24*, 137.
- [28] D.K. Owens, R.C. Wendt, *J. Appl. Polym. Sci.* **1969**, *13*, 1741.
- [29] I. Haller, *Appl. Phys. Lett.* **1974**, *24*, 349.
- [30] K.W. Noh, E. Woo, K. Shin, *Chem. Phys. Lett.* **2007**, *444*, 130.
- [31] K. Shin, E. Woo, Y.G. Jeong, C. Kim, J. Huh, K.-W. Kim, *Macromolecules*, **2007**, *40*, 6617.
- [32] E. Woo, J. Huh, Y.G. Jeong, K. Shin, *Phys. Rev. Lett.* **2007**, *98*, 136103.
- [33] F.C. Frank, *Discuss. Faraday Soc.* **1958**, *25*, 19.
- [34] A. Rapini, M. Papoular, *J. Physique Coll.* **1969**, *30*, C4. 54.

Chapter 7.

Patterning of Solution-Processed Organic

Semiconductors*

*This chapter is based in part on a paper from Kyunghee Lee, Joohee Kim, Kyusoon Shin, and Youn Sang Kim, *Journal of Materials Chemistry* **2012**, *22*, 22763-22768. Copyright (2012) The Royal Society of Chemistry.

7.1. Introduction

7.1.1. Solution-Processed Organic Semiconductors

Pentacene is well-known as an organic p-type semiconductor material in OTFTs (Figure 7.1 (a)). It is composed of five benzene rings and its molecular structure is an open herringbone structure with a combination of face-to-face and edge-to-face interactions. In OTFTs, the thin film of pentacene deposited by evaporation provides high field-effect mobility ($>1 \text{ cm}^2/\text{Vs}$). However, the deposition of pentacene is achieved only under vacuum process because it is not dissolved in common organic solvents. In the early 2000s, Anthony et al. suggested soluble and stable functionalized pentacene, 6, 13-bis (triisopropylsilylethynyl) pentacene (TIPS-PEN) (Figure 7.1 (b)) [1-3]. Trialkylsilyl groups are attached at the 6, 13-positions of the pentacene molecule to improve the solubility in most organic solvents [1]. Furthermore, these functionalized groups help strong two-dimensional face-to-face packing of TIPS-PEN, leading to an excellent hole mobility [1].

Deposition Techniques of TIPS-PEN:

By attaching a functional side group, soluble and stable functionalized pentacene can be prepared. Therefore, it is more accessible for the solution process of organic semiconductors using standard fabrication methods.

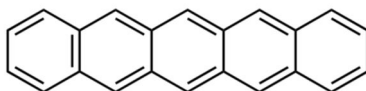
(1) Spin coating [4, 5]: Spin coating is a common deposition technique in organic semiconductor processing that makes uniform thin film of soluble organic materials but suffers from large waste volumes. In addition, because of the rapid

deposition speed during spin coating process, the drying time is short, so only small crystalline aggregates can form in the micrometer range or below.

(2) Drop casting [6-10]: As a better method for crystalline film formation, drop casting has been introduced. In this method, the solvents are allowed to evaporate slowly, leading to the formation of bigger crystals. However, the drop volumes are much larger and the directional alignment is difficult to achieve due to the radial characteristics.

(3) Inkjet printing [11, 12]: Inkjet printing is an attractive deposition technique because of the usage of small amounts of organic materials. Compared to other techniques, it has the benefit of very low waste volumes. However, it is difficult in controlling the resulting crystal morphology, and only radial alignment can be obtained due to rapid solvent evaporation in small droplets.

(a)



(b)

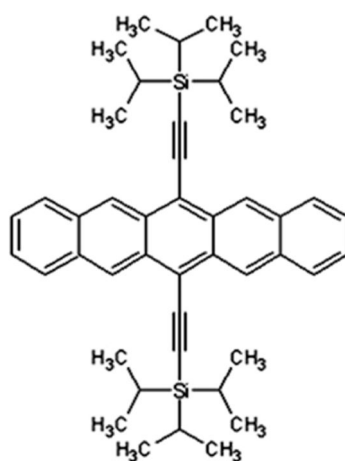


Figure 7.1. Pentacene (a) and 6, 13-bis (triisopropylsilylethynyl) pentacene (TIPS-PEN) (b).

7.1.2. Patterning of Organic Semiconductors

Patterning organic semiconductors in OTFTs is considered as an important deposition technique to eliminate or reduce parasitic current paths (crosstalk) between neighboring devices [22-26]. For large arrays of devices or complex circuits, a significant decrease of the “off” current can be occurred by this parasitic leakage current [24]. However, the patterned semiconductors show minimized electric crosstalk and exhibit the enhanced charge carrier mobility. Therefore, the patterning technique in the solution-based crystal deposition process is highly desirable. Some examples for patterning organic semiconductors are explained as follows.

Self-Assembled Monolayer (SAMs) [23]:

To control the nucleation sites, sizes, and orientation of organic semiconductors in designated locations, Bao *et al.* reported a method for inducing site-specific growth of organic semiconductor crystals using micopatterned self-assembled monolayers (SAMs). They examined the ability of various SAM-modified gold substrates to template the formation of organic semiconductor crystals (Figure 7.2). These substrates were placed in a saturated anthracene/THF solution, where subsequent crystal growth occurred by solvent evaporation (route (1)). Additionally, dip-coating was also used to achieve selective crystallization of organic semiconductor molecules (route (2)). Highly localized crystal growth onto oligophenylene thiol-patterned regions was observed.

Patterned wettability [24, 25]:

Solvent wetting and dewetting processes on surfaces have promising techniques to realize the patterned surface. Bao and coworkers have investigated the assembly of organic semiconducting single crystals by the difference of surface wettability. An organic crystal suspension was first drop-cast on a substrate with patterned hydrophilic and hydrophobic regions and then removed (Figure 7.3 (a)). A series of OM images showing the evaporation process of copper phthalocyanine (CuPc) crystal suspension are shown in Figure 7.3 (b). The patterned CuPc aggregates are found only on the hydrophilic patterns, whereas few crystals are discovered in the hydrophobic region (Figure 7.3 (C)).

Selective contact evaporation printing [26]:

The selective contact evaporation printing method, based on the selective etching of TIPS-PEN crystals by thermal evaporation of TIPS-PEN molecules at the interface with PDMS elastomer, has suggested by Park and coworkers (Figure 7.4 (a)). A pre-patterned PDMS mold is in conformal contact with a large and flat single crystal TIPS-PEN film, and then TIPS-PEN in contact with the PDMS mold were selectively evaporated and diffused into the PDMS when the substrate was heated to 100 °C. The etched microdomains of single crystal TIPS-PEN can be obtained by the selective contact evaporation printing. In addition, additional the selective contact evaporation printing with a different PDMS mold provides further control of micopattern shapes and sizes. In Figure 7.4 (b), micropatterns with squares (1, 2, 7, and 8) and rectangles (3, 4, 5, and 6) with various sizes are demonstrated by optical microscopy. An individual single crystal showed a very smooth and uniform edge surface (9). The heights of single crystals were also very uniform at approximately 75 nm (10).

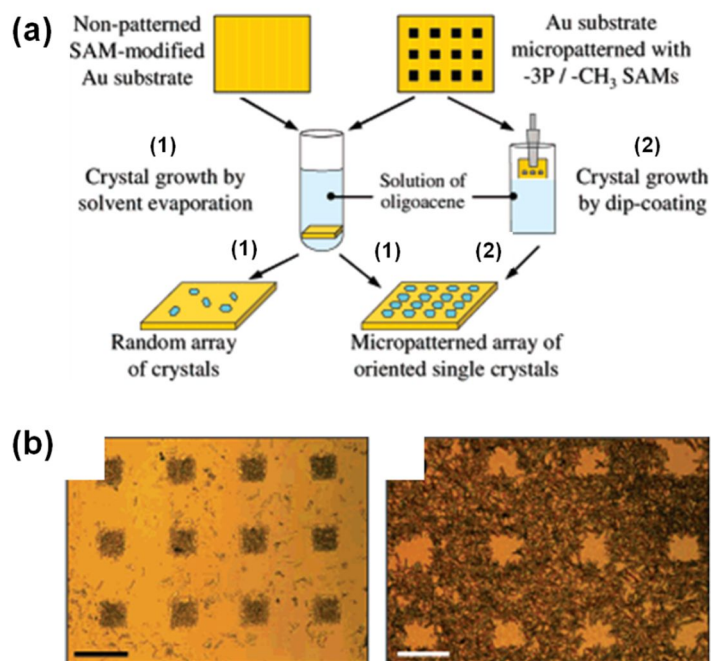


Figure 7.2. Schematic illustration of experimental procedure for the SAM-induced growth of organic semiconductor crystals (a), and the OM images of patterned arrays of anthracene crystals grown on micropatterned SAMs. Scale bars =300 μm [23].

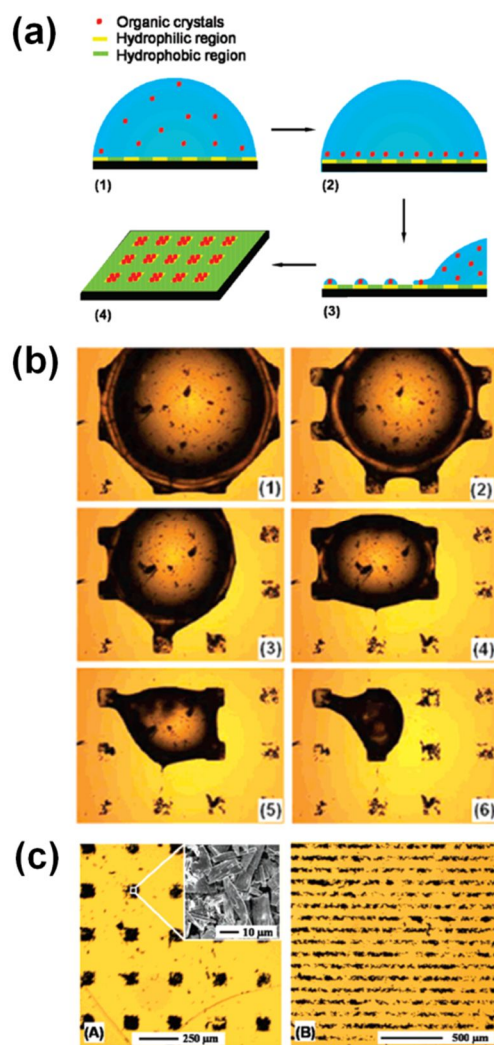


Figure 7.3. Schematic of procedures for organic single crystal assembly (a), the OM images showing the evaporation process of the CuPc crystal suspension [25].

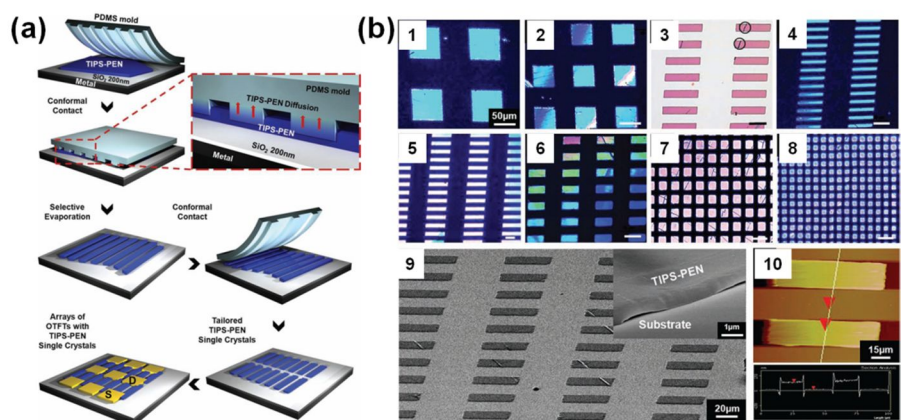


Figure 7.4. Schematic illustration of the selective contact evaporating printing process (a), and the OM images of micropatterned of single crystal TIPS-PEN prepared by the selective contact evaporating printing method with various sizes and shapes (b) [26].

7.1.3. Motivation

Solution-processable organic semiconductors have become attractive materials for low-cost, large-area, and flexible devices based on organic thin film transistors (OTFTs) such as active matrix display backplanes, smart cards, and radio-frequency identification (RFID) tags [1, 2]. In building up of organic semiconductor devices, 6,13-bis(triisopropylsilylethynyl) pentacene (TIPS-PEN), chemically modified pentacene derivatives, has been of great interest because of its good semiconducting behavior due to strong π - π stacking of functional groups as well as high solubility toward common organic solvents [3]. Several groups have reported effective approaches to produce organic crystal semiconductors using solution processes such as spin coating [4, 5], drop casting [6-10], ink-jet printing [11, 12], and dip coating [13, 14]. The formation and growth of TIPS-PEN crystals in solution processes is strongly affected by the evaporation rate of the solvents [15, 16]. Pure solvents, however, are limited to control the evaporation rate due to their intrinsic properties. Especially, solvents with a lower boiling point are not proper to grow the large single crystals, because the crystallization time is too short [15, 16]. Gelinck *et al.* have suggested azeotropic binary solvent mixtures to prepare the large single crystals of TIPS-PEN by controlling evaporation rates [17]. The change from small polycrystals to large single crystals was found at the azeotropic point with a moderate initial mixing ratio, and it resulted in the enhanced transistor performance (average mobility $\sim 0.18 \text{ cm}^2\text{V}^{-1}\text{s}^{-1}$) [17]. Cho *et al.* have employed binary solvent mixtures for inducing two flows in a droplet, convective flow and marangoni flow, to obtain the large crystals while drying solvents [12]. Highly ordered TIPS-PEN crystals in a small droplet were produced by balancing the

evaporation- and diffusion-driven flows, and showed the improved device performance with an effective field-effect mobility of $0.12 \text{ cm}^2\text{V}^{-1}\text{s}^{-1}$ [12].

Even when the desirable crystalline OTFTs with high mobility and outstanding electrical characteristics are obtained, there still remains technical problem to integrate organic semiconductor crystals in practical device applications. Single crystal OTFTs are manufactured one device at a time by handpicking, but this handpicking has critical limitations such as placing organic single crystals in submicrometer scale on a substrate and controlling the precise locations of them [18-21]. Moreover, selective deposition of organic semiconductors is essential to reduce or eliminate parasitic current paths (crosstalk) between neighboring devices [22]. Several approaches to control the deposition of organic semiconductor crystals at a required position have been suggested. Bao and coworkers have demonstrated on solution processing for selective deposition of organic single crystals in a certain location by the introduction of wettability-controlled patterns on surfaces [24, 25]. Even though single crystals selectively deposited on the selected regions, it was impossible to obtain uniform films due to the different numbers and shapes of the organic crystals in patterned region. The patterning of single TIPS-PEN crystals on the basis of selective etching of TIPS-PEN by thermal evaporation has been recently developed [26]. It was a novel process to fabricate the micropatterned single crystals with different sizes and shapes. However, it has been still limited by the location and size of the pre-formed initial single crystal grown on the substrate before selective etching. Thus, it is highly required but challenging to obtain well-defined organic semiconductor pattern with uniformity and crystallinity in OTFT at the same time with simplicity.

7.2. Experimental Section

A schematic illustration of the experimental procedures is shown in Figure 7.5. The bottom surface of the PDMS pad was attached to a slide glass in order to induce a directional evaporation to the patterned top surface during the drying step. When the patterned PDMS pad was immersed in 1 wt% TIPS-PEN/chlorobenzene solution for 1 hr, the PDMS pad was swollen by the organic solvents, containing the TIPS-PEN solution. After drying the solvents under vacuum conditions, the swollen PDMS pad returned to its original size and shape, and mostly TIPS-PEN crystals formed along the patterns at the top surface. Experimental details are as follows.

Preparation of the TIPS-PEN/PDMS stamp:

PDMS molds were fabricated by mixing PDMS prepolymer with crosslinker (Sylgard 184, Dow Corning Corp) at a ratio of 10:1 (w/w). The mixture was poured onto pre-patterned Si masters and then cured at 80 °C for 4 hrs. After the PDMS mold was fully cured, it was simply peeled-off from the Si master mold. The PDMS molds with periodic lines had several sizes ranging from 10 to 40 μm. A rectangular pattern with length x width dimensions of 20 x 70 μm² was employed. The bottom surface of the PDMS pad was attached to glass after UVO treatment for 20 min, and the PDMS/glass stamp was treated at 90 °C for 1 hr for stronger binding. 6, 13-bis(triisopropylsilylethynyl) pentacene (TIPS-PEN) (99.9 % purity) was purchased from Sigma-Aldrich, Korea. The micropatterned PDMS pad was immersed in 1 wt% TIPS-PEN/chlorobenzene (or TIPS-PEN/toluene) solution for

30-60 min. Then, the soaked solvent in the PDMS pad was evaporated under vacuum for 3-5 hrs.

Direct pattern transfer Process:

To transfer the TIPS-PEN crystals on the protruding parts of the PDMS stamp onto the substrates, we used a Si wafer and ITO-glass (thickness: 120 nm, sheet resistance: $15 \Omega/\text{cm}^2$) as a gate electrode and SiO_2 (200 nm-thick thermal oxide) and 10 wt% PMMA in toluene as a gate insulator. All substrates were subjected to 10 min washes in acetone, and in isopropyl alcohol, and then rinsed with distilled water before being dried with nitrogen. In order to facilitate the continuous TIPS-PEN crystal film on the substrates, the pure solvent (chlorobenzene or toluene) was coated on the SiO_2 surface by spin-coating at 1500 rpm for 10 s, and 10 wt% PMMA solution (thickness ~ 500 nm) was coated on the Si or ITO-glass by spin-coating at 3000 rpm for 30 s before conformal contact with the substrates. The TIPS-PEN/PDMS stamp was in conformal contact with Si/ SiO_2 , Si/PMMA, and ITO-glass/PMMA surfaces, and then pressed for a few seconds at 90°C and detached.

Characterization:

Optical microscopy (Olympus BX41, Japan) and atomic force microscopy (SPA300HV, Japan) in tapping mode were used to observe the morphology of the transferred TIPS-PEN films on the SiO_2 and PMMA gate dielectric layer after the removal of residual solvent in the dielectric layer. 2-Dimensional grazing-incidence x-ray diffraction (2D-GIXRD) measurements were performed using the synchrotron source on the 3C and 9A beamline at the Pohang Accelerator

Laboratory (PAL) in Korea. To investigate the crystallinity of the TIPS-PEN, $\theta/2\theta$ mode X-ray diffraction (Bruker D8 Discover, Germany) measurements were performed.

OTFT fabrication and characteristics:

Au electrodes for the source and drain (thickness = 100 nm, width = 1000 μm , length = 100 μm) were thermally evaporated in $\sim 3 \times 10^{-6}$ Torr (5 $\text{\AA}/\text{s}$) through a shadow mask on a patterned thin TIPS-PEN film. The current-voltage measurements were executed under ambient conditions using an Agilent 4155B semiconductor parameter analyzer. All electrical measurements were taken in dark ambient conditions.

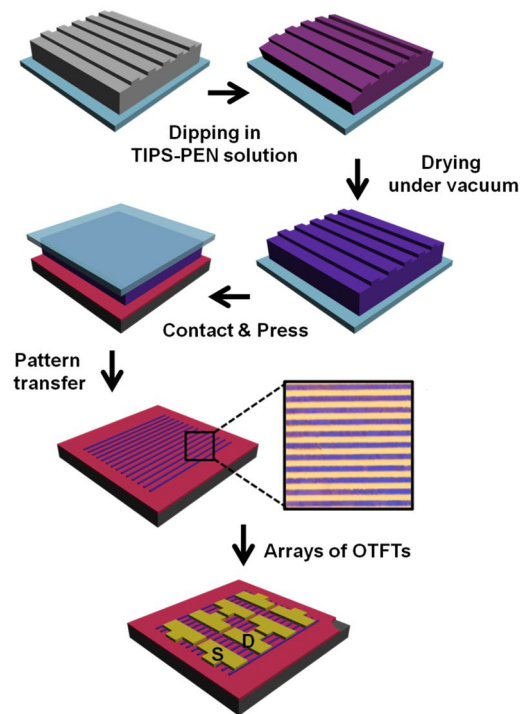


Figure 7.5. Schematic route to the micropatterned TIPS-PEN semiconductors via direct pattern transfer.

7.3. Results and Discussion

Rather than solvent mixtures, we employed single-component solvents. As a matter of fact, using single-component solvents have been reported to be usually unsuccessful in obtaining uniform and highly crystalline thin films by conventional deposition techniques [12, 15, 27]. For example, when the film was prepared by spin-coating of the TIPS-PEN solution, as shown in Figure 7.6, it usually appeared to have discrete crystalline islands due to fast evaporation rate during spin-casting. The discontinuous regions interrupted the formation of the continuous channel for charge carrier transport in an active layer despite the presence of crystalline structures (Figure 7.7). In the case of drop casting, concentric ring structures (“coffee-staining structure” [28]) that was marked at the perimeter of the droplet was observed during solvent evaporation (Figure 7.6 (b)). Drop casting on chemical patterns produced aggregated structure of TIPS-PEN crystals at the edge of the surface pattern (Figure 7.6 (c)). In the mean while, as given in Figure 7.6 (d), micropatterned crystalline uniform TIPS-PEN films could be prepared by direct pattern transfer printing from the patterned PDMS stamp. The TIPS-PEN crystals on the PDMS stamp could be transferred to other substrates by the difference in surface adhesion between PDMS stamp and the substrate. It is thought that the transferred TIPS-PEN micropatterns form the crystalline structures with a good uniformity. Furthermore, it did not need further etching for patterning the semiconductors to avoid the crosstalk.

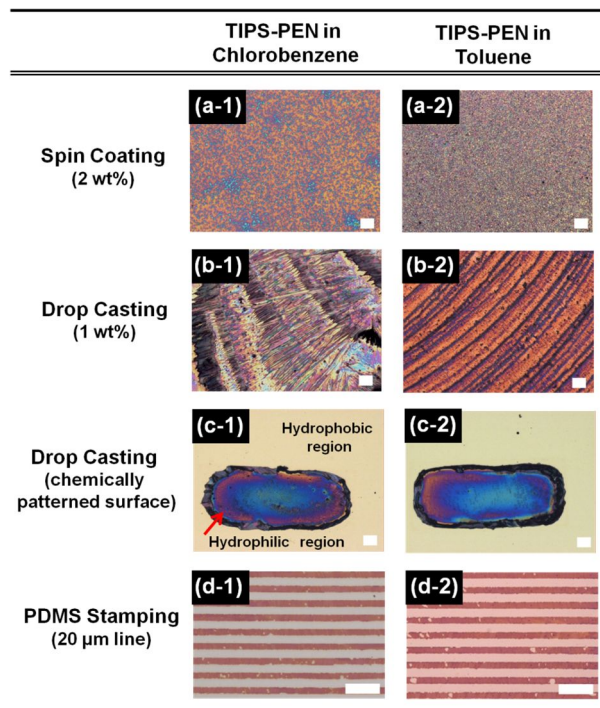


Figure 7.6. The optical images of surface morphologies of TIPS-PEN films obtained by various deposition methods. Each films are prepared by spin coating with 2 wt% TIPS-PEN solution (a), drop casting with 1 wt% TIPS-PEN solution on SiO₂ surface (b) and on chemically patterned SiO₂ surface (c), and direct pattern transfer process with 1 wt% TIPS-PEN solution (d). Scale bars are 100 μm.

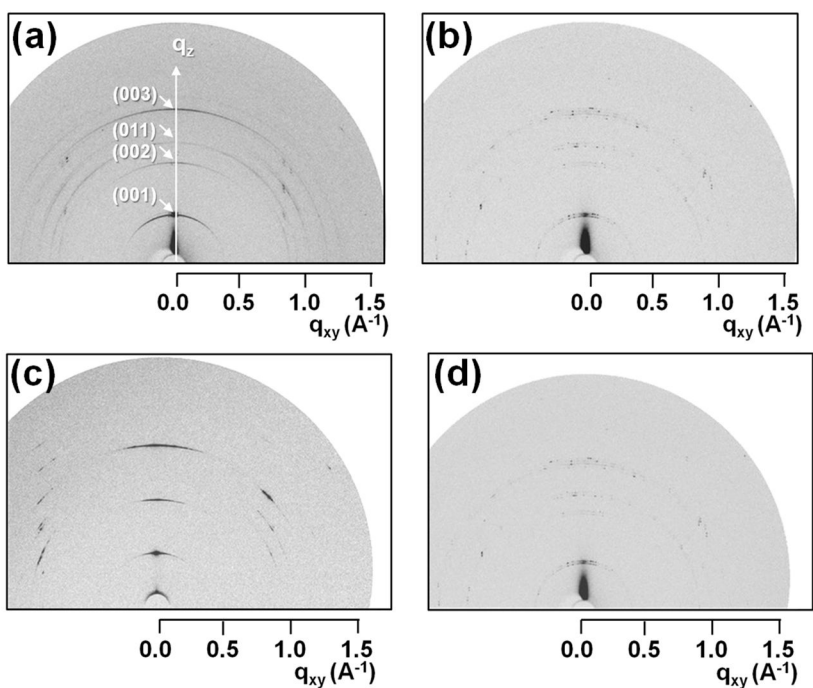


Figure 7.7. 2D GIXRD patterns for TIPS-PEN films obtained by conventional deposition techniques. The films prepared by spin coating with 2 wt% TIPS-PEN in toluene (a) and chlorobenzene (b), and drop casting with 1 wt% TIPS-PEN in toluene (c) and chlorobenzene (d).

In this study, we present a direct pattern transfer method using a patterned poly(dimethylsiloxane) (PDMS) stamp including TIPS-PEN crystals to fabricate uniform organic semiconductor films on the desired position. Our method is based on the crystallization of TIPS-PEN along the patterned surface of a PDMS stamp that can be obtained by soaking the stamp in TIPS-PEN solution and drying solvents. Via direct transfer printing using PDMS stamp, the crystalline TIPS-PEN films can be simply transferred on a substrate. Here, the bottom (unpatterned) surface of the PDMS pad was bound to a glass substrate to lead directional crystallization to the patterned surface of the PDMS pad during evaporation process. When the bottom of the PDMS pad was not stuck to the glass substrate, bulky TIPS-PEN crystals formed at the unpatterned bottom surface, and few TIPS-PEN crystals existed on the patterned top surface (Figure 7.8).

The evaporation time was inherently an important factor in obtaining uniform thin films. It appears more significantly with the variation of the size of PDMS stamp. As the evaporation was elapsed too long, the films of TIPS-PEN get thicker from the edge to center of the pattern (Figure 7.9). For a PDMS surface with $\sim 50 \text{ mm}^2$, an effective evaporation time was approximately 4 hrs under vacuum in this study. Upon the TIPS-PEN/PDMS stamp being in conformal contact with the substrates, the TIPS-PEN crystals on the PDMS surface were transferred on the substrates because of lower surface energy of PDMS ($\sim 21 \text{ mN/m}$). The TIPS-PEN crystals on PDMS stamp, however, was not completely transferred to the substrates, so the films were discontinuous (Figure 7.10 (a)). In order to solve this problem, the TIPS-PEN/PDMS stamp was placed on the substrates after spin-coating of pure solvents on substrate (Si/SiO₂) or dielectric polymer solutions on substrate (Si or ITO-glass). By doing so, the residual solvent after spin-casting improves the

interfacial contact between the TIPS-PEN crystals on the protruding regions of the PDMS stamp and the substrates. After that, the TIPS-PEN/PDMS stamp was slightly pressed for a few seconds, and detached. Then, uniform thickness of TIPS-PEN micropatterns could be obtained (Figure 7.10 (b) and (c)). Here, we thought that TIPS-PEN crystals located at the outermost of the TIPS-PEN/PDMS stamp could be partially recrystallized by residual solvent on the substrate when the stamp was contact with the substrate. So, the molecular ordering (or orientation) of TIPS-PEN at the TIPS-PEN/substrate interface could be influenced by the recrystallization. However, we conjectured that the degree of crystallinity of TIPS-PEN film would be mainly governed during the fabrication process of the TIPS-PEN/PDMS stamp, because a small quantity of residual solvent remained on the substrate after spin-coating of solvents or solutions and the contact time (<10 s) was insufficient to recrystallize completely.

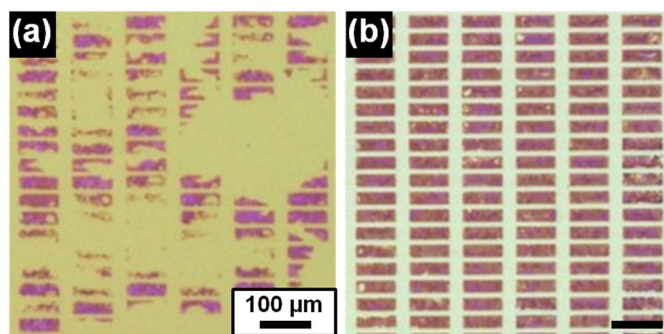


Figure 7.8. The optical images of the transferred TIPS-PEN films by the direct pattern transfer process with PDMS pad without glass substrate (a) and the PDMS pad attached to a glass substrate (b).

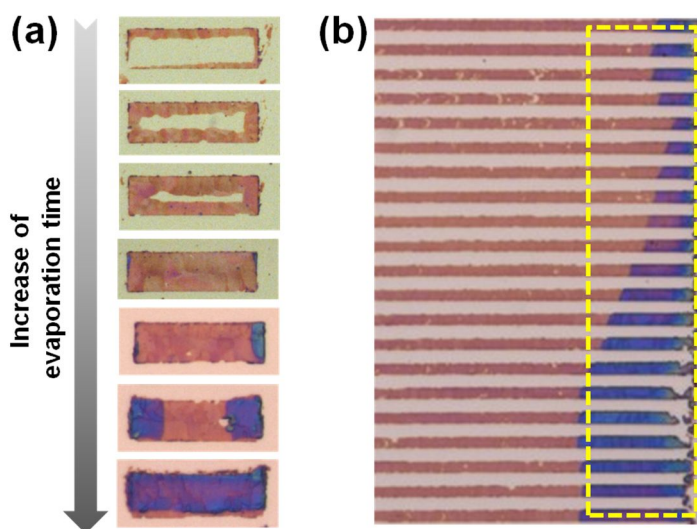


Figure 7.9. The degree of TIPS-PEN crystallization with the elapsed time upon solvent evaporation in rectangular patterns (\sim length x width dimensions of $20 \times 70 \mu\text{m}^2$) (a) and in line patterns ($20 \mu\text{m}$) (b). The nucleation and growth of organic crystalline materials prefers to occur at the edge region of patterns. Below the effective evaporation time, the TIPS-PEN crystals are mostly discovered at the pattern edge. Then, the crystal growth is dominant from the edge to center direction until the films are homogeneous. After the effective evaporation time, the nucleation and growth at the edge region are governed again, so the color of TIPS-PEN films changes to purple, and it means that the films become thicker.

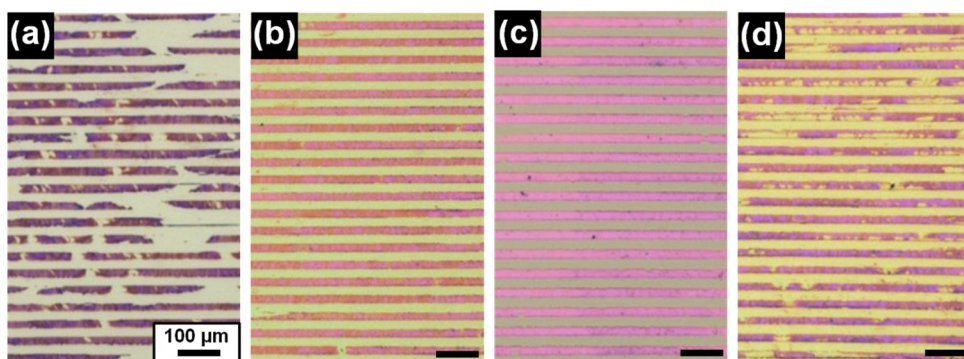


Figure 7.10. The optical microscopy images of the transferred TIPS-PEN patterns. When the TIPS-PEN/PDMS stamp was in conformal contact with the SiO_2 surface, the transferred TIPS-PEN micropattern was discontinuous (a). After spin coating of pure solvent (for the SiO_2 surface) (b) or PMMA solution (for the Si surface) (c), the micropatterned TIPS-PEN film became uniform and continuous. As the TIPS-PEN film was transferred on the PMMA surface after the removal of residual solvent, the line patterns were irregular and non-uniform (d).

The transferred TIPS-PEN crystalline films were shown in Figure 7.11. The thickness of the films was approximately 60 nm measured by atomic force microscopy (AFM) (Figure 7.11 (a)). Line patterned TIPS-PEN films with a variety of sizes ranging from 10 to 40 μm were made with regular thickness by direct pattern transfer using the TIPS-PEN/PDMS stamp (Figure 7.11 (b)-(g)). Additionally, the rectangular patterns with a dimension of 20 x 70 μm^2 (~length x width) were transferred onto Si/PMMA, Si/SiO₂, and ITO glass/PMMA substrates without any etching process, as shown in Figure 7.11 (h)-(j). Regardless of the type of the bottom electrode or gate insulator materials that were used in this study, organic semiconductors were well transferred on the surface at the designed locations. The crystallinity of TIPS-PEN was confirmed with x-ray diffraction (XRD) analysis. The high-order peaks in Figure 7.12 at 10.60° and 15.96° are attributed to the (002) and (003) reflection for the TIPS-PEN crystal structure, respectively, coincident with the previously reported results [15-17]. The intensity of the sharp peak of the TIPS-PEN on the transferred surfaces was relatively weak because the patterned film was thin. However, the transferred TIPS-PEN on SiO₂ and PMMA dielectric layer represented faithfully the crystalline structures. There was no distinct difference in the degree of crystallinity according to the type of dielectric materials. It was regarded that the degree of crystallinity of TIPS-PEN was determined before the transfer printing process.

In order to precisely confirm the molecular ordering and crystalline structures of transferred TIPS-PEN micropatterns, 2D-grazing incidence x-ray diffraction (GIXRD) was performed. A schematic illustration of the GIXRD experiments in this study is shown in Figure 7.13 (a). The self-aligned TIPS-PEN crystals on the SiO₂ dielectric layer cause many reflection spots in the direction of q_z (out-of-plane)

at a given q_{xy} (in-plane), which indicates that 3D crystal structure of the TIPS-PEN film is highly well-ordered in both the vertical and lateral directions (Figure 7.13 (b)). However, slightly scattered ring in Figure 7.13 (c) means that the TIPS-PEN film on the polymeric surfaces includes an unfavorable orientation of TIPS-PEN crystal. Compared with the SiO_2 case, we thought that poorer molecular ordering of TIPS-PEN crystal could be attributed to the possibility of recrystallization of TIPS-PEN on the PMMA surface. When the PDMS/TIPS-PEN stamp was in contact with the dielectric surface containing residual solvent, the possibility of recrystallization on the polymer dielectric surface could be higher than that on inorganic dielectric surface because it contained more residual solvent in polymer chain networks after spin-coating of the polymer solution.

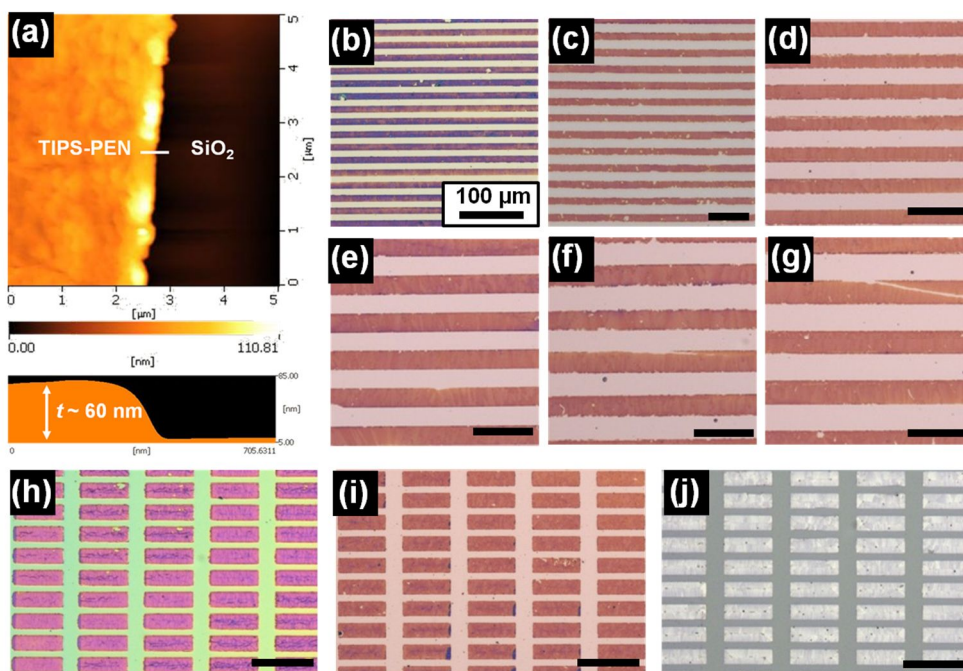


Figure 7.11. AFM images (a) and OM images (b~j) of the transferred TIPS-PEN micropatterns with various sizes and shapes on the dielectric surfaces. The sizes of line pattern are 10 (b), 20 (c), 25 (d), 30 (e), 35 (f), and 40 μm (g). The rectangular patterns are transferred on Si/PMMA (h), Si/SiO₂ (i), and ITO glass/PMMA (j) surfaces.

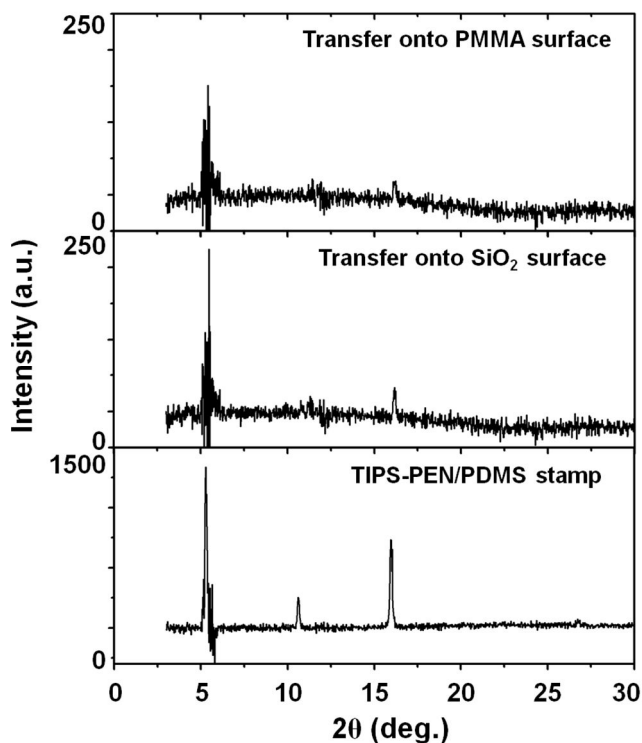


Figure 7.12. X-ray diffraction patterns ($\theta/2\theta$ mode) for the TIPS-PEN crystals on the TIPS-PEN/PDMS stamp and transferred surfaces. The peaks around 5° could be attributed to the combination results of a (001) reflection peak ($\sim 5.3^\circ$) for the TIPS-PEN crystal structure and instrumental noise peaks.

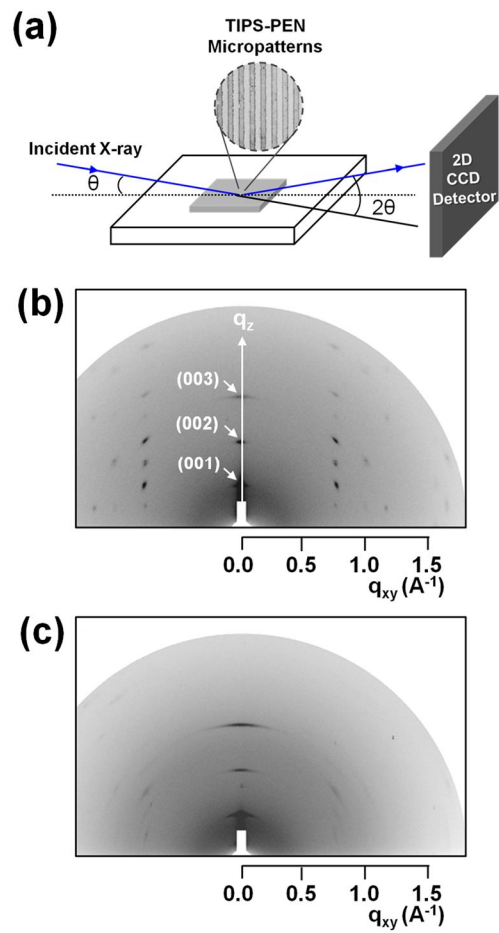


Figure 7.13. 2D GIXRD patterns of the transferred TIPS-PEN micropatterns on SiO_2 (b) and PMMA (c) dielectric layer. A schematic diagram of the experimental set-up for the GIXRD measurements is shown in (a).

Figure 7.14 represents the electrical properties of the bottom gate and top contact OTFTs with the micropatterned TIPS-PEN semiconductors manufactured by the direct pattern transfer printing. About 25 lines of TIPS-PEN micropatterns were bridged between each Au source and drain electrode (The inset of Figure 7.14 (c)). The output characteristics of the OTFTs with inorganic (SiO₂) and organic (PMMA) gate insulator showed a saturation behavior beyond a V_D of -40V (Figure 7.14 (a) and (b), respectively). The representative transfer curve from the OTFTs with the patterned semiconductor films on inorganic (SiO₂) and organic (PMMA) gate insulator in Figure 7.14 (c) and (d), respectively, showed a typical p-type current modulation. In the transfer curve of Figure 7.14 (c), an on/off ratio was $\sim 10^6$ and the highest field-effect mobility (μ) was calculated to be approximately $0.1 \text{ cm}^2\text{V}^{-1}\text{s}^{-1}$, according to the MOSFET standard model in the saturated regime, $I_D = (W/2L)C_i\mu(V_G - V_T)^2$, where W represents the width of the channel, L is the length of the channel between the source and the drain contacts, C_i is the areal capacitance of dielectric layer, and V_T is the threshold voltage. The OTFTs fabricated in this study presented the considerably enhanced device performance as compared to those of the devices prepared by typical deposition methods using single-component solvents [15, 16, 29]. The field-effect mobility on the PMMA dielectric layer in Figure 6d, on the other hand, was calculated to be lower than on silica substrate ($\sim 0.03 \text{ cm}^2\text{V}^{-1}\text{s}^{-1}$). From these results, we found that the electrical properties is dramatically affected by the crystal perfection and ordering of the TIPS-PEN crystals on the dielectric surface, as confirmed by 2D GIXRD analysis in Figure 7.13.

The device performance of the OTFTs was also significantly influenced by the morphological uniformity of the organic semiconductor because morphological

continuity plays an important role in determining charge carrier transport [15]. We analyzed the surface morphology of TIPS-PEN micropatterns using AFM (Figure 7.15). The TIPS-PEN micropattern on the inorganic (SiO_2) substrate had uniform surface topology (Figure 7.15 (a)), whereas the surface morphology of TIPS-PEN on the PMMA film was less uniform and complicated (Figure 7.15 (b)). On PMMA films, moreover, polymer bulge (height~ 36 nm) was observed at the edge of the TIPS-PEN patterns as depicted in the line-scan AFM images of Figure 7.15 (c) (the white arrow). It was considered that the PMMA surface could be slightly patterned by PDMS stamp during the contact and press, because the polymer chains could get mobile by the residual solvent after spin coating of the polymer solution. As a result, surface heterogeneities on the PMMA dielectric layer could deteriorate the electrical properties of OTFTs [30].

We summarized the electrical properties of the OTFTs in Table 1, including the dependence of the soaking solution for the PDMS stamp on the device performance. The output and transfer curves of each OTFT are shown in Figure 7.16. The difference in the device performance in the variation of the soaking solution could be explained by the different evaporation rates of various solvents. These effects resulted in the different crystalline microstructures and morphologies of the formed TIPS-PEN crystals on the patterned PDMS surfaces. We conjecture that the using of solvents with a moderate evaporation could improve the morphology uniformity and packing density of the semiconducting molecules on the patterned PDMS pad, and lead to the enhanced electrical characteristics of the OTFTs.

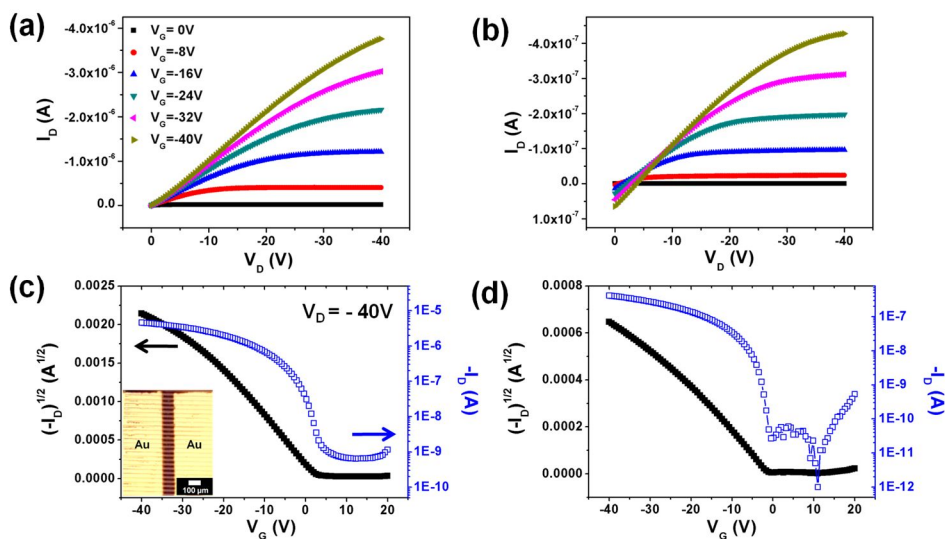


Figure 7.14. The output curve (top) and transfer curve (bottom) of the OTFTs with patterned TIPS-PEN semiconductors on SiO₂ surfaces ((a), (c)) and PMMA surfaces ((b), (d)), respectively. The inset of (c) shows the bottom gate and top contact OTFTs with ~25 lines of TIPS-PEN channels bridged between Au source and drain.

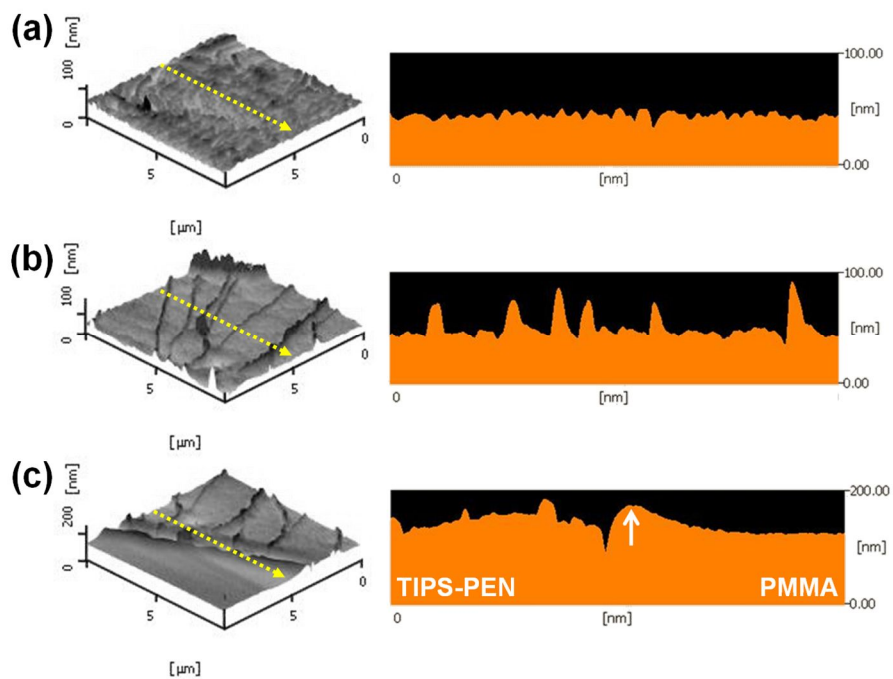


Figure 7.15. Three-dimensional and line-scan AFM images and of the transferred TIPS-PEN morphology on Si/SiO₂ (a) and Si/PMMA surfaces (the center region: (b)/ the edge region: (c)). The yellow-dot arrow indicates the direction of the line-scan and the white arrow in (c) points the patterned PMMA surface during stamping process.

Electrode	Dielectric layer	Soaking solution	μ ($\text{cm}^2\text{V}^{-1}\text{s}^{-1}$)	$I_{\text{On/Off}}$	V_{T} (V)
Si	SiO ₂ (chlorobenzene)	1 wt% TIPS-PEN in chlorobenzene	0.095	$\sim 10^4$	2.94
Si	SiO ₂ (toluene)	1 wt% TIPS-PEN in chlorobenzene	0.108	$\sim 10^6$	1.89
ITO glass	PMMA	1 wt% TIPS-PEN in chlorobenzene	0.027	$\sim 10^4$	0.61
Si	PMMA	1 wt% TIPS-PEN in chlorobenzene	0.026	$\sim 10^4$	0.69
Si	SiO ₂ (toluene)	1 wt% TIPS-PEN in toluene	0.025	$\sim 10^5$	3.96

Table 7.1. The electrical properties of the OTFTs. For SiO₂ dielectric layer, the solvent in the bracket indicates the residual solvent on the surface after spin coating.

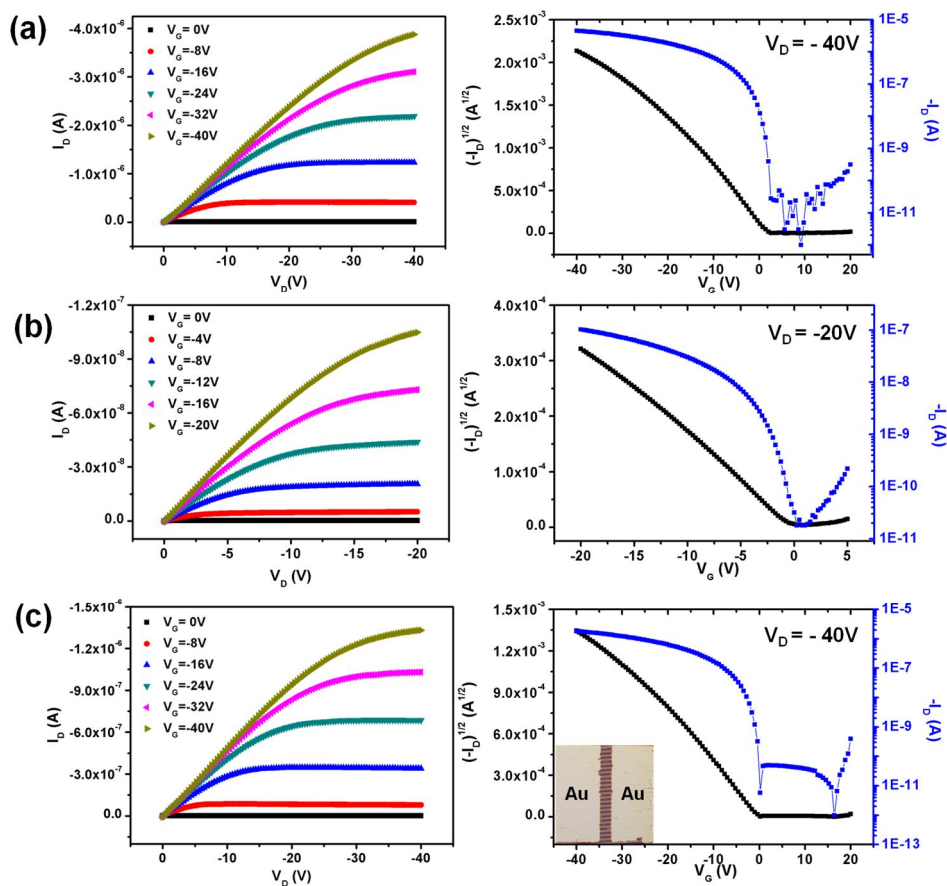


Figure 7.16. Output curve and transfer curve of the OTFTs with TIPS-PEN semiconductors prepared by different bottom electrode/ dielectric layer/soaking solution. Si wafer/SiO₂ (after spin coating of toluene)/ 1 wt% TIPS-PEN in chlorobenzene (a), ITO glass/PMMA/1 wt% TIPS-PEN in chlorobenzene (b), and Si wafer/ SiO₂ (after spin coating of toluene)/ 1 wt% TIPS-PEN in toluene (c). The bottom gate, top contact OTFTs shows in the inset of transfer curve in (c).

7.4. Conclusion

A simple method to fabricate the micropatterned crystalline TIPS-PEN semiconductors through direct pattern transfer printing using the TIPS-PEN/PDMS stamp was investigated. The micropatterned TIPS-PEN semiconductor films on PDMS stamp were directly transferred onto polymeric/inorganic dielectric surfaces at the desired location by the stamping process. The transferred TIPS-PEN on dielectric layer represented definitely the crystalline structures. Additionally, a variety of pattern sizes ranging from 10 to 40 μm were transferred, and the rectangular-shaped active pattern arrays were also simply prepared without any etching process. The OTFTs with the micropatterned TIPS-PEN semiconductors showed the good device performance with the field-effect mobility $\sim 0.1 \text{ cm}^2\text{V}^{-1}\text{s}^{-1}$ on the inorganic (SiO_2) gate insulator. We obtained better field-effect mobility with the SiO_2 dielectric layer than that with the polymeric dielectric layer. It was explained that the electrical characteristics would be varied by morphological uniformity and molecular ordering of TIPS-PEN micropattern on the dielectric surfaces. The patterned organic semiconducting device could be manufactured by the crystalline organic semiconductor/PDMS stamp acquired in general organic solvents. This direct pattern transfer printing of organic semiconductors can be efficient in manufacturing the micropatterns of solution-processed organic semiconductors for the integrated TFT devices. Thus, we expect that the direct transfer printing method itself should be a good tool for the micro-patterning of organic semiconductors.

7.5. References

- [1] J. E. Anthony, *Chem. Rev.* **2006**, *106*, 5028.
- [2] G. Horowitz, *Adv. Mater.* **1998**, *10*, 365.
- [3] J. E. Anthony, J. S. Brooks, D. L. Eaton, S. R. Parkin, *J. Am. Chem. Soc.* **2001**, *123*, 9482.
- [4] J. Kim, J. Jeong, H. D. Cho, C. Lee, S. O. Kim, S.-K. Kwon, Y. Hong, *J. Phys. D: Appl. Phys.* **2009**, *42*, 115107.
- [5] S. K. Park, T. N. Jackson, J. E. Anthony, D. A. Mourey, *Appl. Phys. Lett.* **2007**, *91*, 063514.
- [6] D. H. Kim, D. Y. Lee, H. S. Lee, W. H. Lee, Y. H. Kim, J. I. Han, K. Cho, *Adv. Mater.* **2007**, *19*, 678.
- [7] J.-H. Kwon, S.-I. Shin, K.-H. Kim, M. J. Cho, K. N. Kim, D. H. Choi, B.-K. Ju, *Appl. Phys. Lett.* **2009**, *94*, 013506.
- [8] W. H. Lee, D. H. Kim, Y. Jang, J. H. Cho, M. Hwang, Y. D. Park, Y. H. Kim, J. I. Han, K. Cho, *Appl. Phys. Lett.* **2007**, *90*, 132106.
- [9] C. S. Kim, S. Lee, E. D. Gomez, J. E. Anthony, Y.-L. Loo, *Appl. Phys. Lett.* **2008**, *93*, 103302.
- [10] J.-P. Hong, A.-Y. Park, S. Lee, J. Kang, N. Shin, D. Y. Yoon, *Appl. Phys. Lett.* **2008**, *92*, 143311.
- [11] B. K. C. Kjellander, W. T. T. Smaal, J. E. Anthony, G. H. Gelinck, *Adv. Mater.* **2010**, *22*, 4612.
- [12] J. A. Lim, W. H. Lee, H. S. Lee, J. H. Lee, Y. D. Park, K. Cho, *Adv. Funct. Mater.* **2008**, *18*, 229.

- [13] C. W. Sele, B. K. C. Kjellander, B. Niesen, M. J. Thornton, J. B. P. H. van der Putten, K. Myny, H. J. Wondergem, A. Moser, R. Resel, A. J. J. M. van Breemen, N. van Aerle, P. Heremans, J. E. Anthony, G. H. Gelinck, *Adv. Mater.* **2009**, *21*, 4926.
- [14] R. Z. Rogowski, A. Dzwilewski, M. Kemerink, A. A. Darhuber, *J. Phys. Chem. C* **2011**, *115*, 11758.
- [15] Y.-H. Kim, Y. U. Lee, J.-I. Han, S.-M. Han, M.-K. Han, *J. Electrochem. Soc.* **2007**, *154*, H995.
- [16] K. N. Choi, K. S. Kim, K. S. Chung, H. Lee, *IEEE Trans. Device Mater. Reliab.* **2009**, *9*, 489.
- [17] X. Li, B. K. C. Kjellander, J. E. Anthony, C. W. M. Bastiaansen, D. J. Broer, G. H. Gelinck, *Adv. Funct. Mater.* **2009**, *19*, 3610.
- [18] S. C. B. Mannsfeld, A. Sharei, S. Liu, M. E. Roberts, I. McCulloch, M. Heeney, Z. Bao, *Adv. Mater.* **2008**, *20*, 4044.
- [19] R. W. I. de Boer, M. E. Gershenson, A. F. Morpurgo, V. Podzorov, *Phys. Stat. Sol.(a)* **2004**, *201*, 1302.
- [20] S. C. B. Mannsfeld, A. L. Briseno, S. Liu, C. Reese, M. E. Roberts, Z. Bao, *Adv. Funct. Mater.* **2007**, *17*, 3545.
- [21] V. C. Sundar, J. Zaumseil, V. Podzorov, E. Menard, R. L. Willett, T. Someya, M. E. Gershenson, J. A. Rogers, *Science* **2004**, *303*, 1644.
- [22] K. C. Dickey, S. Subramanian, J. E. Anthony, L.-H. Han, S. Chen, Y.-L. Loo, *Appl. Phys. Lett.* **2007**, *90*, 244103.
- [23] A. L. Briseno, J. Aizenberg, Y. -J. Han, R. A. Penkala, H. Moon, A. J. Lovinger, C. Kloc, Z. Bao, *J. Am. Chem. Soc.* **2005**, *127*, 12164

- [24] S. Liu, W. M. Wang, A. L. Briseno, S. C. B. Mannsfeld, Z. Bao, *Adv. Mater.* **2009**, *21*, 1217.
- [25] S. Liu, W. M. Wang, S. C. B. Mannsfeld, J. Locklin, P. Erk, M. Gomez, F. Richter, Z. Bao, *Langmuir* **2007**, *23*, 7428.
- [26] I. Bae, S. J. Kang, Y. J. Shin, Y. J. Park, R. H. Kim, F. Mathevet, C. Park, *Adv. Mater.* **2011**, *23*, 3398.
- [27] S. H. Lee, M. H. Choi, S. H. Han, D. J. Choo, J. Jang, S. K. Kwon, *Org. Electron.* **2008**, *9*, 721.
- [28] R. D. Deegan, O. Bakajin, T. F. Dupont, G. Huber, S. R. Nagel, T. A. Witten, *Nature* **1997**, *389*, 827.
- [29] H. S. Lee, D. Kwak, W. H. Lee, J. H. Cho, K. Cho, *J. Phys. Chem. C* **2010**, *114*, 2329.
- [30] H. Jia, G. K. Pant, E. K. Gross, R. M. Wallace, B. E. Gnade, *Org. Electron.* **2006**, *7*, 16.

국 문 초 록

자기조립과정에 의해 정렬된 나노 구조를 형성하는 양극산화법(anodization)은 진공 장비를 이용하는 일반적인 리소그래피법에 비해 경제적이고, 대면적 제조가 가능하다라는 장점을 지닌다. 양극산화법을 통해 얻어진 나노 기공성 양극산화알루미늄(Anodized Aluminum Oxide, AAO)은 고밀도로 잘 정렬된 육각 배열 구조를 가지기 때문에, 그 자체로 활용될 수 있을 뿐만 아니라 나노틀(nanotemplate)로 사용되어 다양한 나노 구조를 제작 하는데 에도 활용될 수 있다. 그리하여 본 연구에서는 실린더 형태의 나노 기공성 양극산화알루미늄을 제조하는 기존의 양극산화법을 응용하여, 복잡한 계층 구조를 구현할 수 있는 비전통적인 양극산화법을 제안하였다. 또한 전통적인/비전통적인 양극산화법을 통해 제조된 기공성 나노틀을 이용하여 고분자 나노 구조를 구현하고, 이에 대한 표면 물성을 분석하였다. 또한 패터닝이 도입된 표면은 액정 디스플레이에서 배향막과 트랜지스터에 응용하였다.

제 1장에서는, 나노 구조를 제조하는 기술의 하나로 전통적인 양극산화법을 소개하고, 나노 기공성 양극산화알루미늄산화물의 구조 및 다양한 분야로의 응용성에 대해 간략히 다루었다.

제 2장에서는, 전통적인 양극산화법과 비교하여 보다 복잡하고 다양한 계층 구조를 제조할 수 있는 비전통적인 양극산화법에 대해 제안하였다. 계층구조를 가지는 나노기공성 양극산화알루미늄산화물은 산화물 두께를 조절한 후 전해질의 종류와 가해진 전압에 따라 그 형태가 달라짐을 관

찰하였다. 비전통적인 양극산화법을 통해 얻어진 계층적 나노기공 구조는 일반적인 리소그래피법으로는 구현하기 어려운 100 nm이하의 크기에 서도 쉽게 제조될 수 있음을 보였다.

제 3장에서는, 자연에서 발견되는 생물체들이 표면에 마이크로/나노미터 수준의 계층구조를 가지고 있어 우수한 물성을 가진다는 사실로부터 이러한 표면을 모사하고자 비전통적인 양극산화법을 이용하여 제조하였다. 자연모사기술의 두 대표적인 예인 연꽃잎 표면과 게코도마뱀의 발바닥 표면을 비전통적인 양극산화법을 이용하여 모사하였다. 먼저, 다양한 형태의 계층구조를 가지는 연꽃잎 표면은 1차 양극산화가 진행되고 얻어진 오목한(concave) 형태의 알루미늄표면을 다른 양극산화 조건에서 연속적으로 진행하여 나노틀을 제조한 후 여기에 고분자를 채워넣어 구현하였다. 그 결과, 연꽃잎 표면과 유사한 표면 젖음성(wettability)를 보였다. 두번째로, 게코도마뱀의 발바닥 표면은 비등방적인 계층구조를 가지고 있기 때문에, 실린더형태의 나노틀을 이용하여 일차원적인 고분자 나노구조를 제조하고, 한쪽 면에만 금속을 증착하여 휘어진 나노 구조를 구현하였다. 휘어진 나노구조는 평평한 표면에 비해 비교적 높은 접착력 보였고, 구조적인 특이성으로 비등방적인 접착 거동을 가짐을 관찰하였다.

제 4장에서는, 마이크로/나노 구조가 도입된 표면을 액정 디스플레이에 응용하고자, 액정 디스플레이의 구조에 대해 소개하였다. 패턴이 있는 표면은 액정 디스플레이에서 액정의 배향을 유도하는 배향막에 응용될 수 있기 때문에, 액정 배향 방법 및 메커니즘에 대해 간략히 설명하였다.

또한 액정 디스플레이를 구동하기 위한 스위칭 소자인 트랜지스터(transistor)에도 패터닝된 표면을 도입하고자, 기본적인 유기 박막 트랜지스터에 대해서 설명하였다.

제 5장에서는, 기공성 나노튜브를 이용하여 일차원적인 고분자 나노구조를 배향막으로 사용하여, 나노 구조의 지름 크기와 길이 크기에 따른 액정 분자의 배향 거동을 관찰하였다. 나노 구조는 액정 분자에 상응하는 크기를 가지고 있기 때문에 액정 분자들의 배향 거동에 매우 강한 영향을 준다. 나노구조의 지름 크기가 증가함에 따라, 액정 분자들이 존재할 수 있는 공간은 좁아지고, 이로 인해 강한 공간적인 가둠효과(confinement effect)를 받게 되어 수직 배향으로의 배향 전이가 일어남을 확인하였다. 또한 이러한 배향 전이는 나노 구조의 길이 크기 증가에 따라서도 관찰되었다.

제 6장에서는, 일차원적인 고분자 나노 구조 위에서 액정 분자들의 배향 거동이 공간적인 제약이외에도 표면의 화학적인 특성에도 결정되어짐을 확인하였다. 표면 에너지가 서로 다른 세 종류의 고분자를 이용하여 같은 크기의 나노 구조를 제조한 후 액정 배향 거동을 관찰한 결과, 특정 표면에너지를 가지는 고분자 물질에서만 나노 구조의 지름 크기에 따른 액정 분자의 배향 전이가 관찰되었다. 이로써, 액정 분자들의 배향 거동은 공간적 제약에 따른 액정-액정 상호작용과 표면의 화학적 특성에 따른 액정-배향막 표면 상호작용의 두 경쟁적인 상호작용에 의해 결정됨을 보였다.

제 7장에서는, 최근 각광 받고 있는 플렉서블(flexible) 소자에 응용하고

자 패턴이 있는 표면을 유기 박막 트랜지스터에 도입하였다. 마이크로패턴이 있는 PDMS 단성중합체를 유기 반도체 물질 용액에 담근 후, 용매를 증발시켜 패턴을 따라 유기 반도체 물질의 결정화를 유도하였다. 패턴을 따라 성장한 결정성 유기 반도체 층을 마치 도장 처럼 찍어내어 기판으로 전사하여 패턴된 유기 반도체 층을 형성하였다. 이렇게 얻어진 유기 반도체 층의 결정들은 스침각 X-선 분석 결과 잘 정렬되어 있음을 관찰하였고, 이로 인해 다른 용액 공정에 비해 비교적 높은 소자 성능을 보임을 확인하였다.

주요어: 양극산화알루미늄, 나노 구조, 계층 구조, 액정, 배향막, 유기 박막 트랜지스터

학 번: 2007-21204